Croissance de fissures en interaction : étude numérique du cas "En passant"

Marie-Émeline Schwaab

N° d'ordre NNT : 2018LYSE1276

THÈSE DE DOCTORAT DE L'UNIVERSITÉ DE LYON
opérée au sein de
l'Université Claude Bernard Lyon 1

École Doctorale ED52
Physique et Astrophysique de Lyon

Spécialité de doctorat :
Physique

Soutenue publiquement le 11/12/2018, par :
Marie-Émeline Schwaab

Growth of interacting cracks: Numerical approach to "En-passant" fracture

---

Devant le jury composé de :

Davy Dalmas, Chargé de Recherche CNRS, École Centrale de Lyon	Rapporteur
Grégory Legrain, Maître de Conférences, École Centrale de Nantes	Rapporteur
Mokhtar Adda-Bedia, Directeur de Recherche CNRS, ENS de Lyon	Examinateur
Thouraya Baranger, Professeure, Université Claude Bernard Lyon 1	Examinatrice
Véronique Lazarus, Maître de Conférences, ENSTA ParisTech	Examinatrice
Loïc Vanel, Professeur, Université Claude Bernard Lyon 1	Directeur de thèse
Anthony Gravouil, Professeur, INSA Lyon	Invité

Contents

List of Figures

List of Acronyms

DIC ..... Digital Image Correlation

EP-cracks ..... *En-Passant* crack pair

FE(M) ..... Finite Element (Method)

FPZ ..... Fracture Process Zone

G$_{max}$ ..... Maximum energy release rate bifurcation criterion

LEFM ..... Linear Elastic Fracture Mechanics

MTS ..... Maximum Tangential Stress

PC ..... Polycarbonate

PDMS ..... Polydimethylsiloxane

PET ..... Polyethylene terephthalate

PLS ..... Principle of Local Symmetry

SED ..... Strain Energy Density

SIF ..... Stress Intensity Factor, defined at the crack tip

SIF* ..... Stress Intensity Factor, defined at the tip of an infinitesimal crack extension

Introduction

Understanding and predicting material failure is of prime importance when designing mechanical structures, for both economical and safety reasons. In practice, macroscopic failure rarely intervene through the catastrophic propagation of a single crack. Other phenomena such as creep, fatigue failure or the growth and coalescence of pre-existing micro-defects are more commonly encountered. Understanding how two cracks interact is therefore necessary to evaluate the risk this last example presents. However, precise modelling of crack-crack interaction is not a problem as straightforward as studying a single defect or approaching statistically the material properties of a medium containing many cracks. The problem is indeed both coupled and non-local: because any crack tip acts as a singularity that alters the surrounding stress field close and far, multiple cracks affect each other by curving to form complex paths and fracture patterns.

The specific case of "En-passant" fracture has recently gained a renewed interest in relation with three experimental studies [1–3]. Initially used by geologists to describe transverse fracture along rift zones, the term *en-passant* now refers to any fracture pattern in which two initially parallel cracks interact, such as the one presented in Fig. 1. *En-passant* crack pairs (EP-cracks) were thereafter observed in a wide variety of materials, at magnitudes ranging from a few micrometers to several kilometres. We expect phenomena intervening at a metallic grain scale or a continent scale to be fundamentally different, without possible comparison between them. However, EP-cracks present a remarkable uniformity in their propagation shape: it is quasi-systematically hook shaped, formed by the succession of repulsive and attractive interaction phases between the cracks. This seemingly universal behaviour is still poorly understood: as of today, there are no simple predictions of magnitude and length of the repulsive component of the paths. More significantly still, contradicting and conflicting affirmations have been put forward concerning the origin of the repulsive phase. While Fender *et al.* [1] proposed a model that only predicts the attractive behaviour, Dalbe *et al.* [2] observations questioned the very validity of the principle of local symmetry, a commonly accepted bifurcation criteria. Koivisto *et al.* [3] tried to mitigate this conclusion by suggesting that the principle of local symmetry may be correct if one takes into account plastic effect around the crack tips, totally disregarding known occurrences of repulsive EP-cracks propagating in brittle media.

The main motivation of this thesis was therefore to clarify, hopefully once and for all, the real limitations of the linear elastic fracture mechanics framework, used in conjunction with the assumption of the principle of local symmetry, when studying interacting cracks. We found that this simple framework, while necessarily imperfect, provides still an excellent approximation of the characteristic hook-shape and reproduces well some common features of EP-crack paths, such as the position of the repulsion to attraction transition or the intersection angle between the cracks. Another surprising observation by Dalbe *et al.* [2] was that materials with comparable elastic behaviours could result in different repulsive interaction intensity. Using a diffuse damage model, we confirm that this phenomenon can probably be attributed to the size of the fracture process zone around the crack tips.

As a preliminary, chapter 1 presents the context and motivation of this study in deeper details: it

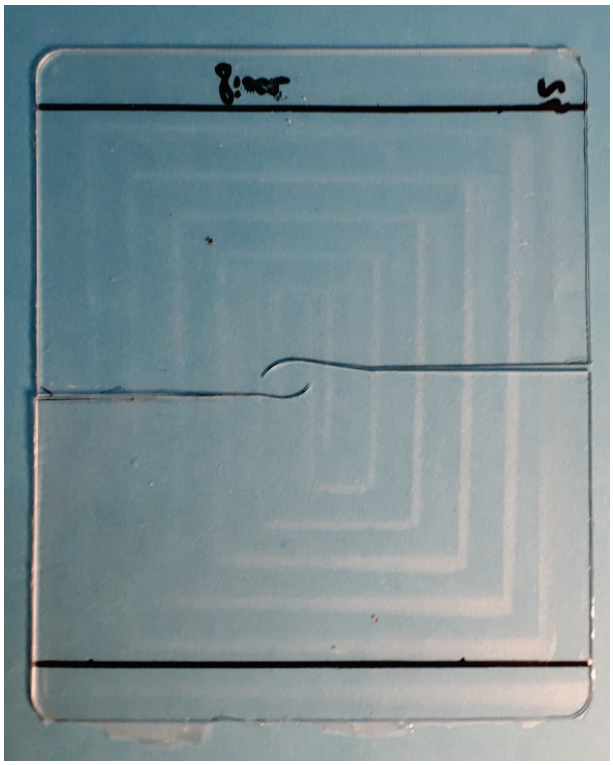

Figure 1 – **Example of EP-cracks in PDMS:** This film is 10 cm $*$ 12 cm $*$ 0.1 cm. The cracks were cut as two straight lines, separated by 2 cm in the longitudinal direction and by 0.5 cm transversally before being submitted to an opening tensile test

proposes an overview of both the theoretical frameworks used, linear elastic fracture mechanics and damage mechanics, and of the current knowledge concerning the *en-passant* fracture patterns.

The main findings of this dissertation are developed in chapter 2. A careful examination of the initial kink angle between EP-cracks, as predicted by the principle of local symmetry, revealed the precise geometric conditions for the existence of a repulsive phase according to linear elastic fracture mechanics. We also provide an explanation why the ubiquitous in nature repulsive phase can easily be missed in laboratory experiments or when computing the initial propagation direction of the cracks, effectively reconciling experiments with theory.

Finally, we show in chapter 3 how damage mechanics constitutes a better approach to model EP-cracks properly. We show that a diffuse representation of the cracks is a worthy approach to understand how the fracture process zone size influences the magnitude of the repulsion phase between the cracks.

Chapter 1

En-Passant fracture: theoretical background

Contents

Modern day fracture mechanics consists of an array of increasingly complex models destined to encompass the large variety of physical phenomena revolving around the crack growth process such as -but not limited to- brittle fracture, ductile fracture or the formation of a plastic zone. In most cases, the fundamental principles of these theories were laid down in the early 20^{th} century by a series of breakthrough papers [4–8] forming what we now refer to as the Linear Elastic Fracture Mechanics (LEFM) framework. This set of tools and hypotheses, while suffering from physically impossible conclusions, is still an excellent approach for brittle materials and the reference framework of fracture mechanics. Its validity in regard to the study of interacting cracks was questioned in contradictory papers (see 1.3.1). The first part of this dissertation was realized assuming the hypotheses of LEFM, with the aim of clarifying what are the predicted EP-cracks propagation paths in this framework.

While LEFM is based on a discrete representation of fracture, other models regard the cracks as diffuse. Recently, the development of phase-field resolution techniques applied to damage models allowed to introduce an additional parameter to otherwise purely linear elastic frameworks. The second part of our work consists in examining whether this extra input is sufficient to remedy the limitations LEFM modelling exhibits when confronted to experimental observation.

In this chapter, we will present both theoretical frameworks as well as a brief literature review concerning the core of our subject: en-passant fracture.

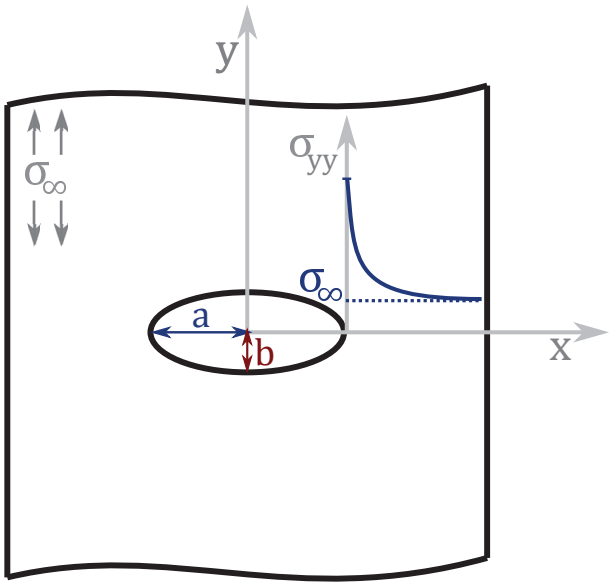

Figure 1.1 – **Stress concentration at an elliptical hole**

1.1 Linear Elastic Fracture Mechanics: an initial model of fracture

Beyond presenting a brief history of the early development of fracture mechanics, the intent of this section is to introduce the different concepts and quantities involved in a LEFM study, namely the stress intensity factors and the energy release rate of a propagating front. We will then review different bifurcation criteria useful to determine the propagation direction. We will finally see how to determine the stress intensity factors and the energy release rate for any given fracture problem, as they will be needed to determine in practice the crack path.

1.1.1 Stress concentration: an asymptotic approach of fracture

The stress in a solid body submitted to external forces or load is not homogeneous; its intensity is highly dependent on the solid geometry. The concept of stress concentration was introduced by Inglis [5] when he determined the stress distribution around an elliptical cavity (semi-axes $a > b$) traversing a plate subjected at infinity to an uniaxial traction σ_∞. Without going into the details of the derivation, it is shown that the maximum stress in the plate is located at the tip of the ellipse and is related to its shape factor by $\sigma_{max} = \sigma_\infty(1 + 2a/b)$. The stress concentration factor K_t is then defined by $K_t = 2a/b$ and, depending exclusively on geometry, can reach all values of $]2; \infty[$.

One way to define a crack is to consider it to be the limit case of a flattened elliptical hole or, in other words, an ellipse whose semi-minor axis is equal to zero, meaning that $a/b \to \infty$. Inglis' result is remarkable as it demonstrates a cornerstone concept of LEFM: the stresses at the tips of a sharp crack are predicted to approach infinity. The uses of Westergaard's stress functions [6] allowed to conduct significant stress analysis at the crack tip: in two independent landmark papers, Williams [7] and Irwin [8] showed this stress singularity to be of the order $r^{-1/2}$, with r

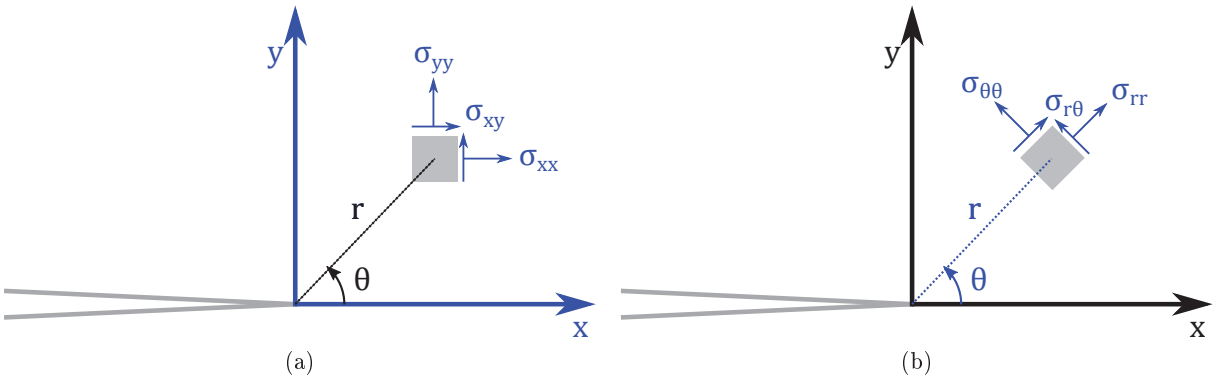

Figure 1.2 – **Coordinates systems & stress tensors at a 2D crack tip:** (a) cartesian (x, y) and (b) polar (r, θ).

being the radial distance to the tip (see Fig.1.2). Indeed, the asymptotic stress-field is entirely defined by universal weight functions, and a set of problem-dependent scalars, K_I, K_{II} and K_{III}. In polar coordinates the stress field expansion can be expressed as:

$$\sigma_{rr} = \frac{K_I}{4\sqrt{2\pi r}}\left(5\cos\frac{\theta}{2} - \cos\frac{3\theta}{2}\right) + \frac{K_{II}}{4\sqrt{2\pi r}}\left(-5\sin\frac{\theta}{2} + 3\sin\frac{3\theta}{2}\right) + O(1) \tag{1.1}$$

$$\sigma_{\theta\theta} = \frac{K_I}{4\sqrt{2\pi r}}\left(3\cos\frac{\theta}{2} + \cos\frac{3\theta}{2}\right) + \frac{K_{II}}{4\sqrt{2\pi r}}\left(-3\sin\frac{\theta}{2} - 3\sin\frac{3\theta}{2}\right) + O(1) \tag{1.2}$$

$$\sigma_{\theta r} = \frac{K_I}{4\sqrt{2\pi r}}\left(\sin\frac{\theta}{2} + \sin\frac{3\theta}{2}\right) + \frac{K_{II}}{4\sqrt{2\pi r}}\left(\cos\frac{\theta}{2} + 3\cos\frac{3\theta}{2}\right) + O(1) \tag{1.3}$$

The coefficients of the leading order of these expansions, K_I, K_{II} and K_{III}, are the *stress intensity factors* (SIF) of the three corresponding modes of fracture and $O(1)$ (constant term in the expansion) terms are sub-singular terms such as the T-stress or boundary effects acting far from the crack tip [9].

Considering that a crack can be defined as the locus of a discontinuity in the displacement field u of a solid body, it is useful to distinguish the three basic solicitation modes of the crack. The displacement jump $[u] = u^+ - u^-$ is then defined by the difference between the two fields across the fracture surface. While most cracks are solicited under complex mixed-mode loading, any stress or displacement field around the crack tip is a linear combination of the three following modes, as expressed in a Cartesian coordinate system (See Fig.1.3):

- mode I, or opening: the cracks lips move away from each other in a direction perpendicular to the plane of the crack.

$$[u_x] = 0, [u_y] \neq 0, [u_z] = 0 \tag{1.4}$$

- mode II, or sliding: the crack lips are sheared in direction orthogonal to the crack front.

$$[u_x] \neq 0, [u_y] = 0, [u_z] = 0 \tag{1.5}$$

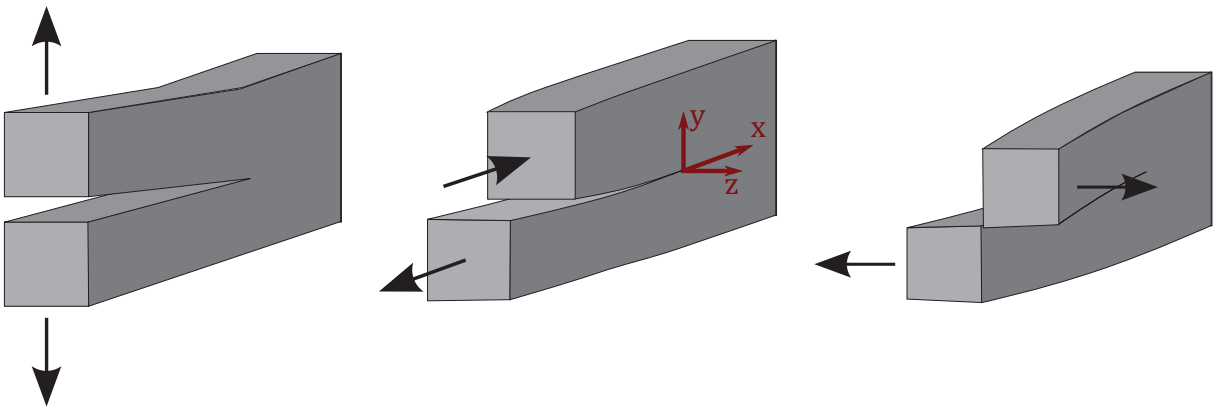

Figure 1.3 – **Basic modes of fracture:** (a) Mode I: opening, (b) Mode II: sliding, (c) Mode III: tearing, possible in 3D exclusively. Adapted from [10]

- mode III, or tearing: the crack lips are sheared in direction orthogonal to the crack front.

$$[u_x] = 0, [u_y] = 0, [u_z] \neq 0 \tag{1.6}$$

Given the relationship between stress and displacement in linear elasticity, it is possible to retrieve an explicit expression of the SIF useful in a 2D problem [11, 12]:

$$K_I = \lim_{r \to 0} \frac{\mu}{\kappa + 1} \sqrt{\frac{2\pi}{r}} [u_2] \tag{1.7}$$

$$K_{II} = \lim_{r \to 0} \frac{\mu}{\kappa + 1} \sqrt{\frac{2\pi}{r}} [u_1] \tag{1.8}$$

Note: μ is the shear modulus of the material and κ the Kolosov constant, whose value depends on the Poisson's ratio ν and the plane stress or strain assumption:

$$\kappa = \begin{cases} 3 - 4\nu \text{ for plane strain} \\ \dfrac{3 - \nu}{1 + \nu} \text{ for plane stress} \end{cases} \tag{1.9}$$

Thus, the values of the stress intensity factors not only quantify the magnitude of the stress singularity, but also provide an indication on the nature of the crack solicitation. This second piece of information will be useful to determine the crack propagation direction, whereas the first is indicative of when and if the crack propagates at all. Indeed, equations (1.1) through (1.3) show that the intuitive idea that materials break when their stress reaches a certain critical value becomes inapplicable at a crack tip as the stresses there go to infinity.

To circumvent this problem, Irwin postulated the existence of a material dependent quantity K_{Ic}, the fracture toughness, which constitutes the threshold under which the crack does not propagate. It may seem far-stretched to base a stability criterion on an unrealistic principle such as infinite stresses. However, experiments on a given material give measures of K_{Ic} consistent across geometries and loadings, and we will see in the following section that this asymptotic

approach is equivalent to a global reasoning based on energetic considerations.

1.1.2 Energy release rate: a thermodynamic approach to fracture

Extending the first law of thermodynamics to fracture

Also basing his work on Inglis' stress analysis [5], Griffith proposed in 1920 the founding theory of fracture mechanics [4] as an extension of the first principle of thermodynamics: the introduction of the surface energy γ_s allowed Griffith to consider propagation of a preexisting defect as an energy-balance problem. Here γ_s stands for the energy necessary to create new fracture surfaces per unit area and is intrinsically tied to the energy necessary for bond breakage. In the event of a quasi-static crack propagation, and neglecting all non-mechanical works, the energy balance between two instants t and $t + dt$ is expressed as:

$$\delta W_{ext} = dW_k + dW_{el} + 2e\gamma_s dl \tag{1.10}$$

This equation conveys that the work of external forces δW_{ext} is converted in either the variation of the kinetic energy W_k, of the strain energy W_{el} or the creation of new fracture surfaces when the crack total length increases of dl. The newly created surface area amount to $2dA = 2edl$, with e being the thickness of the medium. When dt goes to 0, eq. (1.10) can be rewritten in terms of powers:

$$\dot{W}_{ext} = \dot{W}_k + \dot{W}_{el} + 2e\gamma_s \dot{l} \tag{1.11}$$

The *energy release rate* G, that is to say the energy consumed during crack propagation per unit of newly created free surfaces area, can be defined as:

$$G = -\frac{d}{edl}(W_{el} - W_{ext}) \tag{1.12}$$

Crack propagation will be unstable if $dW_k/dt > 0$ [13] which translates as:

$$\frac{\partial W_k}{\partial A}.\frac{dA}{dt} > 0 \tag{1.13}$$

Given that the assumption that the crack cannot heal and only advance, i.e. $dA/dt > 0$, we retrieve:

$$\frac{\partial W_{ext}}{e\partial l} - \frac{\partial W_{el}}{e\partial l} - 2\gamma_s > 0 \tag{1.14}$$

or:

$$G > 2\gamma_s \text{ for unstable propagation} \tag{1.15}$$

On the other hand, we clearly get from eq. (1.11) and (1.12) that the following must remain true at all times of a quasi-static propagation :

$$G\dot{l} = 2\gamma_s \dot{l} \tag{1.16}$$

The Griffith propagation criterion results from the two solutions of this equality: as crack propa-

gation is an irreversible process, either $\dot{l} = 0$ and there is no condition on the energy release rate or $\dot{l} > 0$ and $G = 2\gamma_s$. While only G can be inferred from the knowledge of $\dot{l}$ in eq. (1.16), and not vice versa, the converse implication is usually admitted: the crack will propagate as soon as the rate of release of elastic strain energy reaches the rate at which surface energy is created. Thus, in a quasi-static propagation, G is capped by the *critical strain energy release rate* $G_c = 2\gamma_s$. This quantity is a purely material property, dependent only on the nature and configurations of the atomic bonds inside the body in the case of brittle fracture.

Equivalence with Irwin's theory

While the reasoning in Griffith's and Irwin's approaches are drastically different, their results as to when a crack will propagate are identical. Making the assumption that the crack propagates in its own plane, that is to say without turning or kinking, Irwin showed [8] that G and the SIF are mathematically equivalent:

$$G = \frac{\kappa + 1}{8\mu}\left(K_I^2 + K_{II}^2\right) + \frac{1}{2\mu}K_{III}^2 \tag{1.17}$$

This relationship between the stress intensity factors and the energy release rate has several very important consequences. First and foremost, it lends physical meaning to the $K_I = K_{I,c}$ propagation criteria which was originally based on the debatable existence of a stress singularity at the crack tip. It is now possible to express the critical SIF above which crack propagation occurs. For example, in pure mode I we get:

$$K_{I,c}^2 = \frac{8\mu}{\kappa + 1}G_c \tag{1.18}$$

Eq. (1.17) serves also proof that G, while being linked to a variation of energy between two states, only depends on the current asymptotic stress field and not on the knowledge of either the stress field far away from the crack or the stress state after propagation.

1.1.3 Bifurcation criteria: Determining where the cracks propagate

Sections 1.1.1 and 1.1.2 addressed the issue of how to determine *when* a crack propagate in brittle materials or, in other words, what loading is necessary to insure quasi-static crack propagation. By themselves, both Griffith and Irwin's theories can not predict *where* the crack will propagate. In mixed mode, the assumption of a bifurcation criterion is necessary to determine the shape and direction of the crack path. Many bifurcation criteria where proposed since the second half of the 20^{th} century; in this section, we will review the most commonly used.

Maximum tangential stress (MTS)

This criterion, proposed in 1963 by Erdogan an Sih [14], is both the first introduced historically and the most intuitive since it stems from the idea that the material will break in the direction

orthogonal to the greatest tension. Referring to the initial kink angle as θ_i, this criterion can be expressed as:

$$\frac{\partial \sigma_{\theta\theta}}{\partial \theta}(\theta = \theta_i) = 0 \tag{1.19}$$

It is possible to substitute $\sigma_{\theta\theta}$ by its asymptotic expression in 2D to get the relationship between θ_i and the stress intensity factors:

$$K_I \sin\theta_i + K_{II}(3\cos\theta_i - 1) = 0 \tag{1.20}$$

From there, it is possible to derive an explicit expression of θ_i when $K_{II} \neq 0$:

$$\theta_i = 2\arctan\left[\frac{1}{4}\left(\frac{K_I}{K_{II}} - \text{sign}(K_{II})\sqrt{\left(\frac{K_I}{K_{II}}\right)^2 + 8}\right)\right] \tag{1.21}$$

If $K_{II} = 0$ then $\theta_i = 0$ for this criterion as well as all others. The maximum tangential stress criterion (MTS) is widely used because of its good compliance with experiments [14–16] and its ease in the determination of θ_i.

Strain energy density (SED)

Sih [17, 18] also introduced a measure of the strength of the elastic energy field in the vicinity of a crack tip, the *strain energy density* (SED) function S. This quantity is expressed in function of the stored strain energy per unit volume $\mathrm{d}W/\mathrm{d}V$ and the radial distance:

$$S = r\frac{\mathrm{d}W_{el}}{\mathrm{d}V} \tag{1.22}$$

The crack is assumed to propagate in the direction minimizing S, classically expressed in its asymptotic form dependent on the SIF [16]:

$$S = a_{11}K_I^2 + a_{12}K_I K_{II} + a_{22}K_{II}^2 \tag{1.23}$$

Here, the a_{ij} coefficients are functions not only of θ, but also of the Kolosov constant. As a consequence, and contrarily to all other criteria reviewed here, results from the SED are dependent on the plane problem assumption and the value of the Poisson's ratio. The main interest of the SED relies in its ability to account for yield, allowing extension to problems outside of the LEFM framework, such as ductile fracture [19, 20]. In these situations, S is expressed directly in terms of the stress field [21]:

$$S = \frac{1}{2\mu}\left(\frac{\kappa+1}{8}(\sigma_{rr} + \sigma_{\theta\theta})^2 - \sigma_{rr}\sigma_{\theta\theta} + \sigma_{r\theta}^2\right) \tag{1.24}$$

The SED was also successfully extended to 3D situations, fatigue and non-homogeneous materials [19, 20]. However, some experimental studies found the SED to be less precise than other criteria such as the MTS [15]. Other difficulties, as the existence of multiple minima in the energy density function or the non-existence of a minimum, were also reported [22].

Maximum energy release rate

The criteria seeking to maximize the strain energy release rate (G_{max}) was also proposed by Ergodan and Sih [14]. It is thought with the same reasoning as the Griffith criteria for crack propagation: the crack grows to minimize the potential energy of the body, and the crack front advances as soon as G reaches a critical value G_c. The crack will therefore kink in the first direction for which this is possible. The kinking angle is then determined by:

$$\frac{\mathrm{d}G}{\mathrm{d}\theta}(\theta = \theta_i) = 0 \tag{1.25}$$

and:

$$\frac{\mathrm{d}^2G}{\mathrm{d}\theta^2}(\theta = \theta_i) \leqslant 0 \tag{1.26}$$

Note that G represents the variation of the energy in the body when the crack advances *of an infinitesimal length* in the direction θ_i. Taking l as the extension length, θ_i must maximize the function $G^*(\theta) = \lim_{l \to 0} G(l, \theta)$

Principle of local symmetry (PLS)

The principle of local symmetry (PLS) considers that any crack under mixed-mode loading will kink so that its extension is in purely opening mode; the stress field at the new tip will be then locally symmetrical about the crack plane. It was first introduced in 1973 by Goldstein and Salganik [23] and benefited greatly from the contributions of first Cotterell and Rice [24] as well as Amestoy and Leblond [25, 26] who, in both cases, provided asymptotic expansions for the crack paths and the SIF in the neighborhood of the kink.

To properly express the PLS mathematically, we need to differentiate between K_I and K_{II}, the SIF *before crack extension* at the original crack tip, from K_I^* and K_{II}^* the SIF *after propagation* (see Fig. 1.4). Again, the SIF* are dependent on both the kink angle and the propagation length, which leads to the mathematical expression of the PLS:

$$\lim_{l \to 0} K_{II}^*(l, \theta = \theta_i) = 0 \tag{1.27}$$

Choosing a bifurcation criterion

Bifurcation criteria are either *explicit*, in the sense that they rely on quantities determined at the crack tip in its original configuration, or *implicit*, meaning that they require the knowledge of future quantities defined at the crack tip after a theoretical propagation. Explicit criteria such as the MTS or the SED are usually favored in numeric studies to determine crack paths [27–32]. Indeed, their use is much less computer intensive than using implicit criteria for which we must determine the SIF and other quantities for a myriad of extended crack configurations.

On the other hand, the PLS, an implicit criterion, should be preferred for any homogeneous and isotropic material. Beyond its excellent accuracy, it was demonstrated by Leblond [11, 26]

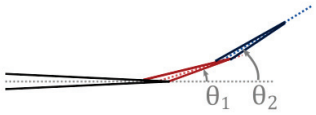

Figure 1.4 – **SIF before and after propagation:** K_I^* and K_{II}^* are defined at the new tip of the crack (in red), while K_I and K_{II} are defined the original tips (in black). The corresponding solicitation modes, opening and sliding should be understood in the local coordinate systems defined at the crack front (e_x, e_y) and (e_x^*, e_y^*) respectively.

that this criterion is the only physically admissible one in this configuration. The reasoning is as follows: in the case of a crack propagating into a homogeneous and isotropic material, under constant loading, we expect the crack path to be smooth, free of any discontinuities with the exception of the initial kink. If the crack were to propagate initially in a direction other than the one predicted by the PLS, we would necessarily retrieve $K_{II}^{*} \neq 0$. Consequently, the crack tip would still be solicited under mixed-mode, and the crack is bound to kink again, which is not admissible under our set of assumptions.

It should however be noted that the choice of a bifurcation criterion is usually of little impact on the final results; with the exception of almost pure mode II loadings, experimental scatter is often too large to differentiate between criteria [16]. For example, while the PLS and the G_{max} criteria are not strictly equivalent, to catch the difference between these two criteria one must expand the SIF as a function of the initial kink angle at least to the order 5 [26]. Given numerical imprecisions, they are virtually indistinguishable.

1.1.4 Practical determination of the SIF before propagation

Numerous techniques exist to determine the SIF and the energy release rate of any given fracture problem, either analytically or numerically. Analytic methods usually rely on the superposition principle to reduce the problem to a linear combination of known solutions, a good number of them being already catalogued into handbooks [17, 33]. These techniques are usually limited to simple geometries and loadings, and are only approximate as numerical methods for more complex cases.

Numerical methods most often rely on a global approach to fracture: the energy release rate is determined first and the SIF are then deduced from the relationships linking G, K_I and K_{II} for a straight crack in LEFM. Intuitively, the most straightforward way to determine G is to come back to its definition and to evaluate the elastic energy stored into a body twice : first for a crack of length l, and again for a crack of length $l + \delta l$. The infinitesimal nature of δl implies a very fine mesh around the crack tip, resulting in significant computation time.

However, the most well-known method to compute G is more direct and involves only one computation step: once the stress state of a body is known, the determination of the path independent J-integral introduced by Rice [34] is quite simple. Considering a crack tip enclosed in a contour Γ of normal $\boldsymbol{n}$, and taking the strain energy density as ψ, J is defined in 2D as [11] :

$$J = \int_{\Gamma} (\psi n_x - \sigma_{ij} u_{i,x} n_j) ds \tag{1.28}$$

Note that while i and j are dummy indexes used in Einstein summation convention, x is the fixed direction normal to the crack front defined in Fig. 1.4.

It was shown later by Bui [13] that J does not depend on the chosen contour, as long as the crack is straight inside Γ and the crack lips are traction-free, and is equal to G. The path-independence property is very useful in practical applications where the analytical solution for the stress field

is not known: it is often determined numerically using approximating techniques such as the finite element method (FEM). The presence of a stress singularity at the crack tip compounds the numerical errors in a zone a few element wide: choosing a larger path allow better precision by avoiding this area.

Another technique, the virtual extension method introduced by Hellen [35] and Parks [36, 37], is used in conjunction with finite element computation. While it determines G as the variation of strain energy between two steps of a straight propagation, it also only requires the knowledge of the stress state prior propagation. Indeed, the crack is propagated not by increasing the number of double nodes in the mesh but *virtually* by moving the node corresponding to the crack tip, which implies computer-intensive changes in the stiffness matrix.

Finally, the $\boldsymbol{G}(\boldsymbol{\Theta})$ (or sometimes **THETA**) method was initially developed by Destuynder [38]. Several improvements were introduced later to reach excellent accuracy and efficiency [39]. This procedure relies on a clear definition of G as a derivative of the potential energy, and presents the advantage to be generalizable to the 3D case and not limited to the linear elastic case [40]. The $\boldsymbol{G}(\boldsymbol{\Theta})$ procedure is based on the J-integral, but its accuracy is vastly improved by the use of a virtual vector field and of surface (rather than contour) integration. It is now implemented in well-known finite element solvers such as Code Aster [41] or Cast3m [42].

Here, we will only detail the techniques employed throughout the following section: the $\boldsymbol{G}(\boldsymbol{\Theta})$ procedure was used for the determination of both the energy release rate G and the stress intensity factors K_I and K_{II}. As we have seen in the previous section, it is also useful to know these quantities *after* propagation which can be cumbersome to compute using finite element methods. To circumvent this problem and determine K_I^* and K_{II}^*, we applied the work of Amestoy and Leblond [25, 26, 43], which is presented in detail in section 1.1.4.

G($\boldsymbol{\Theta}$) procedure

Here, $\boldsymbol{\Theta}$ refers to the virtual crack extension field. It is a vector field and should not be confused with the kink angle θ_i. The $\boldsymbol{\Theta}$ field is defined in the coordinate $(O, \boldsymbol{x}, \boldsymbol{y}, \boldsymbol{z},)$ system tangent to the crack surface and normal to the crack front (see Fig. 1.5), and acts as a mapping function matching the initial body containing the crack to a body with an infinitesimally longer crack.

Considering a reference body Ω containing a traction-free crack of which we know the stress state, an infinitesimal geometric perturbation transforms each point $\boldsymbol{M}$ of Ω into $\boldsymbol{M^\eta}$[44]:

$$\boldsymbol{M^\eta} = \boldsymbol{M} + \eta.\boldsymbol{\Theta}(\boldsymbol{M}) \tag{1.29}$$

Destuynder [38] gave the energy release rate associated with the chosen virtual crack extension field $\boldsymbol{\Theta}$. When neglecting thermal variations and taking ψ as the energy density it becomes :

$$\boldsymbol{G}(\boldsymbol{\Theta}) = \int_{\mathcal{D}} \left(\psi \nabla.\boldsymbol{\Theta} - \boldsymbol{\sigma} : (\nabla \boldsymbol{u} \nabla \boldsymbol{\Theta})\right) dV \tag{1.30}$$

Here $\boldsymbol{G}(\boldsymbol{\Theta})$ is the *global* energy release rate: it is a quantity dependent on the virtual crack

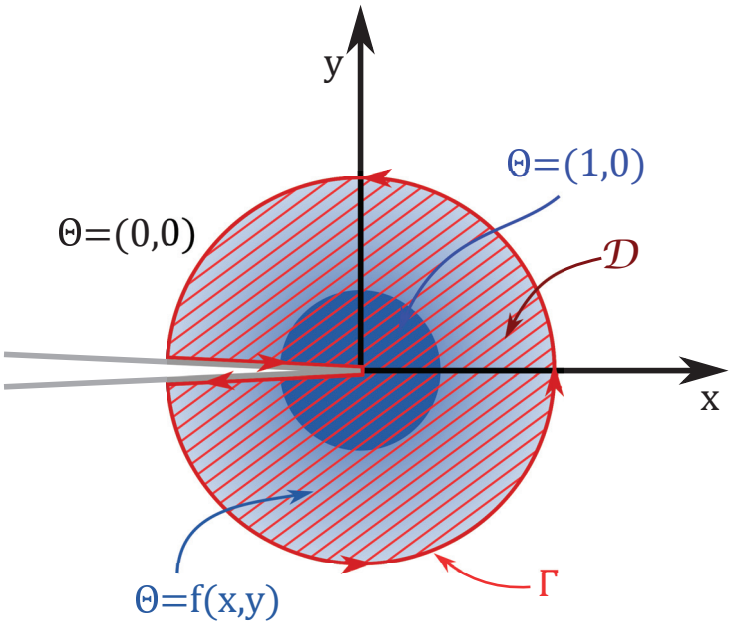

Figure 1.5 – **Typical mapping function Θ: Θ** is constant in the inner and outer sections. On the intermediate ring it varies continuously as a function of the coordinates (x, y) between the unit vector $(1, 0)$ (constant value near the crack tip) and $(0, 0)$ (constant value in the majority of the body). The closed contour Γ defines the domain $\mathcal{D}$: both of them are used as integration domain to compute the SIF.

extension field value. In 2D, the *local* energy release rate G is a single scalar obtained from the following equation:

$$G = \boldsymbol{G}(\boldsymbol{\Theta}(\boldsymbol{O})) \tag{1.31}$$

where O refers to the crack tip. One must respect several constraints when choosing $\boldsymbol{\Theta}$:

- $\boldsymbol{\Theta}$ must modify only the crack *tip* position or, in other words, it should be null on all other points of the domain border $\partial\Omega$,
- $\boldsymbol{\Theta}$ must be regular on Ω,
- $\boldsymbol{\Theta}$ must be locally tangent to the crack lips.

In practice, $\boldsymbol{\Theta}$ is chosen so that the integration in eq. (1.30) is as precise and as fast as possible: $\boldsymbol{\Theta}$ is taken constant everywhere, so that $\nabla\boldsymbol{\Theta}$=0 there, except on an anulus surrounding the crack tip [45]. Inside the inner ring, $\boldsymbol{\Theta} = (1, 0)$ and $\boldsymbol{\Theta} = (0, 0)$ outside the outer ring (see Fig. 1.5). This considerably decreases the size of the actual integration domain.

SIF at the original crack tip

Both the J-integral method or the $\boldsymbol{G}(\boldsymbol{\Theta})$ procedure are limited by their inherent incapability to determine the individual stress intensity factors separately. To separate the three rupture modes and identify the SIF, the use of other path-independent integrals is valuable. Stern *et al.* [46] used Betti's reciprocal work theorem and the link between the SIF and the first order stress field

(see eq. (1.1) through (1.3)) to introduce the first expression of a linear combination of K_I and K_{II} as a contour integral. In a similar fashion, Yau *et al.* [47] used the J-integral and suitable auxiliary fields to propose the well-known interaction-integral technique. Considering a fictive mechanical equilibrium $\left(u_j^{(tot)}, \epsilon_{jk}^{(tot)}, \sigma_{jk}^{(tot)}\right)$ as the sum of the current state $\left(u_j^{(c)}, \epsilon_{jk}^{(c)}, \sigma_{jk}^{(c)}\right)$ and an auxiliary field $\left(u_j^{(a)}, \epsilon_{jk}^{(a)}, \sigma_{jk}^{(a)}\right)$, eq. (1.28) is reformulated to express the total J-integral as:

$$J^{tot} = \int_\Gamma (\psi^{tot} n_x - (\sigma_{ij}^c + \sigma_{ij}^a)(u_{i,x}^c + u_{i,x}^a) n_j) ds \tag{1.32}$$

where the subscript $u_{i,x}$ is $u_{i,x} = \partial u_i / \partial x$. Naturally, ψ^{tot} is the strain energy of the superimposed state and should not be confused with the sum of ψ^c and ψ^a:

$$\psi^{tot} = \frac{1}{2}(\sigma_{ij}^c + \sigma_{ij}^a)(\epsilon_{ij}^c + \epsilon_{ij}^a) \tag{1.33}$$

It is possible to reorganize eq. (1.32) so that the J-integrals of the two superimposed states appear:

$$J^{tot} = J^c + J^a + M^{a,c} \tag{1.34}$$

Here, $M^{a,c}$ refers to the interaction integral between the current and the auxiliary state. Its expression is deduced from eq. (1.32) and (1.34):

$$M^{a,c} = \int_\Gamma \left(\frac{1}{2}(\sigma_{ij}^c \epsilon_{ij}^a + \sigma_{ij}^a \epsilon_{ij}^c) n_x - (\sigma_{ij}^c u_{i,x}^a + \sigma_{ij}^a u_{i,x}^c) n_j \right) ds \tag{1.35}$$

Using the equality $J = G$ and the equivalence between the Irwin and Griffith theories given in eq. (1.17), eq. (1.32) can also be rewritten in terms of stress intensity factors [47]:

$$J^{tot} = J^c + J^a + 2\alpha \left(K_I^c K_I^a + K_{II}^c K_{II}^a \right) \tag{1.36}$$

where α is dependent on the plane problem:

$$\alpha = \begin{cases} \dfrac{1-\nu^2}{E} \text{ for plane strain} \\ \dfrac{1}{E} \text{ for plane stress} \end{cases} \tag{1.37}$$

It comes directly from eq. (1.35) and (1.36) that

$$M^{a,c} = 2\alpha \left(K_I^c K_I^a + K_{II}^c K_{II}^a \right) \tag{1.38}$$

Eq. (1.35) allows for an easy determination of $M^{a,c}$ as long as the current stress state is known on a contour enclosing the crack tip. Consequently, it is possible to derive the SIF of the current problem using eq.(1.38) and a sensible choice of auxiliary state. The most direct solution is obtained when the auxiliary state is either pure mode I or II. Thus, when $K_I^a = 1$ and $K_{II}^a = 0$, we get $K_I^c = \dfrac{1}{\alpha} M^{a,c}$ or, when $K_I^a = 0$ and $K_{II}^a = 1$, we get $K_{II}^c = \dfrac{1}{\alpha} M^{a,c}$.

In practice, the contour integral $M^{a,c}$ is replaced by the integration integral $I^{a,c}$. This integral was introduced by Gosz and Moran [48] and is simply the combination of the $\boldsymbol{\Theta}$ field and $M^{a,c}$

transformed into a surface integral to improve the accuracy of the SIF determination:

$$I^{a,c} = \int_{\mathcal{D}} \left[\frac{1}{2}(\sigma_{ij}^c \epsilon_{ij}^a + \sigma_{ij}^a \epsilon_{ij}^c)\delta_{kl} - (\sigma_{ij}^c u_{i,k}^a + \sigma_{ij}^a u_{i,k}^c) \right] \Theta_{k,l} dV \tag{1.39}$$

where $\mathcal{D}$ is the domain inside Γ, where $\boldsymbol{\Theta}$ is non-zero (see Fig. 1.5).

SIF along the crack path

As we have seen in section 1.1.3, the principle of local symmetry requires the knowledge of K_{II} not at the tip of the crack in its original configuration, but after an infinitesimally small extension. This quantity K_{II}^* is of course dependent on the kink angle θ_i (see Fig. 1.4). Direct determination of the SIF* using FEM is time-consuming, as the computation should be repeated for each possible θ_i value. Fortunately, we know from the work of Amestoy and Leblond [11, 25, 26, 43] that K_I^* and K_{II}^* are dependent exclusively on the SIF before extension and the kink angle. The relationships between this parameters are universal, in the sense that their coefficients do not depend on geometry or loading, this information already being encapsulated in the original SIF:

$$\begin{bmatrix} K_I^*(\theta_i) \\ K_{II}^*(\theta_i) \end{bmatrix} = \begin{bmatrix} M_{11}(\theta_i) & M_{12}(\theta_i) \\ M_{21}(\theta_i) & M_{22}(\theta_i) \end{bmatrix} . \begin{bmatrix} K_I \\ K_{II} \end{bmatrix} \tag{1.40}$$

Accurate expressions of $M_{11}(\theta_i)$, $M_{12}(\theta_i)$, $M_{21}(\theta_i)$, $M_{22}(\theta_i)$ have been developed by Amestoy [26], up to the order 22:

$$\begin{aligned} M_{11}(\theta_i) = 1 &- \frac{3\pi^2}{8}m^2 + \left(\pi^2 - \frac{5\pi^4}{128}\right)m^4 + \left(\frac{\pi^9}{9} - \frac{11\pi^4}{72} + \frac{119\pi^6}{15360}\right)m^6 \\ &+ 5.07790m^8 - 2.88312m^{10} - 0.0925m^{12} + 2.996m^{14} - 4.059m^{16} \\ &+ 1.63m^{18} + 4.1m^{20} + O(m^{22}) \end{aligned} \tag{1.41}$$

$$\begin{aligned} M_{12}(\theta_i) = &- \frac{3\pi}{8}m + \left(\frac{10\pi}{3} + \frac{\pi^3}{16}\right)m^3 + \left(-2\pi - \frac{133\pi^3}{180} + \frac{59\pi^5}{1280}\right)m^5 \\ &+ 12.313906m^7 - 7.32433m^9 + 1.579m^{11} + 4.0216m^{13} - 6.915m^{15} \\ &+ 4.21m^{17} + 4.56m^{19} + O(m^{21}) \end{aligned} \tag{1.42}$$

$$\begin{aligned} M_{21}(\theta_i) = &\frac{\pi}{2}m - \left(\frac{4\pi}{3} + \frac{\pi^3}{48}\right)^3 + \left(-\frac{2\pi}{3} + \frac{13\pi^3}{30} - \frac{59pi^5}{3840}\right)m^5 \\ &- 6.73023m^7 + 4.44112m^9 - 1.5340m^{11} - 2.0700m^{13} + 4.684m^{15} \\ &- 3.95m^{17} - 1.32m^{19} + O(m^{21}) \end{aligned} \tag{1.43}$$

$$
\begin{aligned}
M_{22}(\theta_i) = 1 &- \left(4 + \frac{3\pi^2}{8}\right) m^2 + \left(\frac{8}{3} + \frac{29\pi^2}{18} - \frac{5\pi^4 4}{128}\right) m^4 \\
&+ \left(-\frac{32}{15} - \frac{4\pi^2}{9} - \frac{1159\pi^4}{7200} + \frac{119\pi^6}{15360}\right) m^6 + 10.58254 m^8 - 4.78511 m^{10} \\
&- 1.8804 m^{12} + 7.280 m^{14} - 7.591 m^{16} + 0.25 m^{18} + 12.5 m^{20} + O(m^{22})
\end{aligned}
\tag{1.44}
$$

with $\theta_i = \pi m (-1 < m < +1)$ denoting the kink angle formed between the original crack and its extension.

1.1.5 Limitations of the LEFM framework and existence of a fracture process zone

To summarize, LEFM is a macroscopic approach to fracture: criteria for crack propagation are based on energy balance and unconcerned with microscopic breaking processes. Representing the material as continuous, isotropic, and homogeneous for all scales results in square-root singular stress fields at the crack tip, which is physically unacceptable. However, all materials have a smallest representative volume under which their average mechanical properties are not statistically matching the continuum bulk description. Most materials will go through inelastic transformations before breaking, such as plastic deformation or the nucleation of micro-cracks. The zone where inelasticity prevails is known as the fracture process zone or sometimes as the plastic zone: because it undergoes dissipation mechanisms LEFM is invalid in this region. The small scale yielding assumption postulate that the fracture process zone is much smaller than all other characteristic lengths of the problem including the crack length. Under such conditions, the stress field provided by the LEFM theory are valid on an annulus enclosing the fracture process zone: the K-dominance zone. Outside the annulus, the stress fields are dominated by boundary conditions and LEFM, which is an asymptotic approach to fracture, also breaks down (Fig. 1.6).

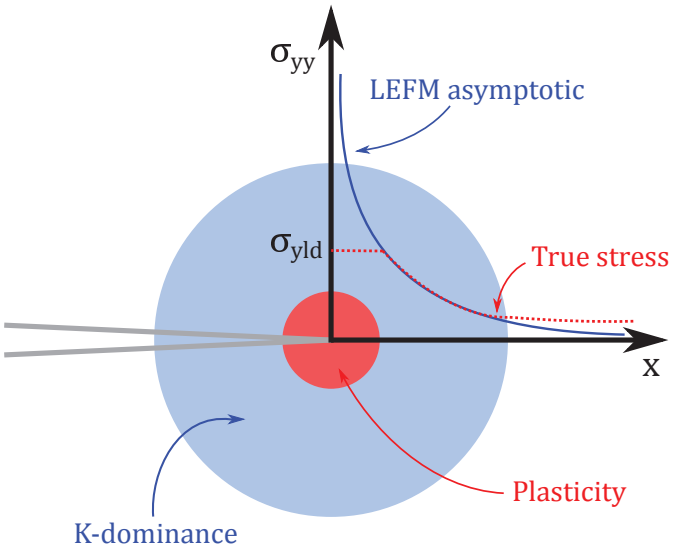

Figure 1.6 – **LEFM asymptotic solution compared to the "true" opening stress:** For a crack submitted to a far away tensile stress σ_∞ the LEFM solution is not valid extremely close to the crack tip where inelastic phenomena take place. The actual shape of the plastic zone is complex and controlled by many parameters. It depends most notably on the plane problem assumption. Outside the K-dominance annulus, the asymptotic solution becomes once again invalid as boundary conditions grow more important: the true opening stress tends to σ_∞, not 0.

1.2 Diffuse crack models: a variational approach to fracture

As we have seen in section 1.1, the classical approach of fracture mechanics based on Griffith's work is essentially an energy minimisation problem, in which the surface and strain energies compete. The variational approach of fracture consists in treating the problem thermo-mechanically as a whole, instead of dissociating the propagation and bifurcation criteria as is standard in LEFM. The crack length and shape become simply one parameter among others controlling the Gibbs free energy ψ. Representing cracks as material singularities hinders the proper differentiation of ψ: variational approaches to fracture require a regularized parameter. Phase-field solving techniques are based on this principle and use an additional scalar damage variable to represent a smooth transition between undamaged and broken materials.

In this section, we first aim to present how phase-field methodologies arose from the local state method. We will then present in more details the model of Miehe *et al.* [49], later implemented into Abaqus by Molnár *et al.* [50], on which the results from chapter 3 are based, and its numerical implementation.

1.2.1 The local state method

The variational approach of fracture is derived from the local thermodynamical state method developed by Lemaitre and Chaboche [51]. The aim of this technique is to establish a formalism compatible with the laws of thermodynamics and resolvable using numerical analysis techniques. It is well suited to study coupled problems, among which damage mechanics.

State variables

The local state method is based on the assumption that the thermo-mechanical state at a material point is entirely determined by a number of variables defined *at this point exclusively* [51]. Because the time derivatives of these variables are not taken into account, any approach stemming from this method will necessarily obey the quasi-static assumption: all processes are a succession of equilibrium states.

The state variables can be classified into two categories:

- *Observable variables*, such as the temperature T or the linearised deformation tensor $\boldsymbol{\epsilon}$, are necessary to define the thermo-mechanical state of a material as they appear in the first and second principle of thermodynamics.
- *Internal variables* represent dissipative phenomena and as such the solicitation history the material went through. While not directly measurable, they represent a real material state such as the crystalline micro-structure, the dislocation density or plastic deformation. In models using irreversible deformation, the total deformation $\boldsymbol{\epsilon}$ cannot be used as an observable variable. It is partitioned into its observable component, the elastic deformation $\boldsymbol{\epsilon^e}$, and the internal plastic deformation $\boldsymbol{\epsilon^e}$:

$$\boldsymbol{\epsilon} = \boldsymbol{\epsilon^e} + \boldsymbol{\epsilon^p} \tag{1.45}$$

  The number and nature of the internal variables $\boldsymbol{V_1}$,... ,$\boldsymbol{V_k}$ is an arbitrary choice driven by the modelled phenomenon complexity and the level of details one wishes to consider.

Laws of thermodynamics

The first law of thermodynamics is used under the small scale deformation assumption:

$$\rho \dot{e} = \boldsymbol{\sigma} : \dot{\boldsymbol{\epsilon}} + r - \mathrm{div}\boldsymbol{q} \tag{1.46}$$

where ρ is the density, e the internal specific energy (energy per unit mass), r the heat source density and $\boldsymbol{q}$ the heat flux.

We express second law of thermodynamics through the Clausius-Duhem inequality:

$$\boldsymbol{\sigma} : \dot{\boldsymbol{\epsilon^p}} - \rho(\dot{\psi} + s\dot{T}) - \boldsymbol{q}\frac{\nabla T}{T} \geqslant 0 \tag{1.47}$$

where $\psi = e - Ts$ is the specific free energy and s the specific entropy.

State laws

We assume the existence of a thermodynamic potential from which the state laws derive: as long as this scalar function is concave in regard to T, convex in regard to $\boldsymbol{\epsilon^e}$ and all $\boldsymbol{V_k}$, the

conformity with the second principle of thermodynamics through the Clausius-Duhem inequality is guaranteed.

For solids at a constant temperature, the chosen potential is generally the specific Helmholtz free energy $\psi = \psi(\boldsymbol{\epsilon^e}, T, \boldsymbol{V_k})$. Without detailing the derivation, it is possible to retrieve the state laws of elasticity from eq. (1.46) and (1.47):

$$\boldsymbol{\sigma} = \rho \frac{\partial \psi}{\partial \boldsymbol{\epsilon^e}} \tag{1.48}$$

$$s = -\frac{\partial \psi}{\partial T} \tag{1.49}$$

With $\boldsymbol{\sigma}$ the stress tensor i.e. the dual variable of $\boldsymbol{\epsilon}$.

By analogy it is possible to define the dual variables of all $\boldsymbol{V_k}$:

$$\boldsymbol{A_K} = \rho \frac{\partial \psi}{\partial \boldsymbol{V_k}} \tag{1.50}$$

Note that, while eq. (1.48) is a state law describing the evolution of an otherwise defined internal variable, eq. (1.50) is merely a definition of the dual internal variables $\boldsymbol{A_k}$. More equations are required to balance the number of unknowns.

Evolution laws

A dissipation potential $\phi = \phi(\dot{\boldsymbol{\epsilon^p}}, \dot{\boldsymbol{V_k}})$ is introduced to complete the model. As for the state laws, using a scalar potential is a convenient way to ensure consistency with the laws of thermodynamics. Considering the state laws, the Clausius-Duhem inequality becomes:

$$-\rho \frac{\partial \psi}{\partial \boldsymbol{\epsilon^p}} \dot{\boldsymbol{\epsilon^p}} - \rho \frac{\partial \psi}{\partial \boldsymbol{V_k}} \dot{\boldsymbol{V_k}} - \frac{\boldsymbol{q} \nabla T}{T} \geqslant 0 \tag{1.51}$$

$$\Leftrightarrow \boldsymbol{\sigma} : \dot{\boldsymbol{\epsilon^p}} - \boldsymbol{A_k} \dot{\boldsymbol{V_k}} - \frac{\boldsymbol{q} \nabla T}{T} \geqslant 0 \tag{1.52}$$

The first term refers to mechanical dissipation and the second to thermal dissipation: both must be positive independently from the other.

The dissipation potential is generally chosen as a positive, scalar function of $\dot{\boldsymbol{V_k}}$: this ensure automatic positivity of the mechanical dissipation. The ensuing relation is then:

$$\boldsymbol{A_K} = -\frac{\partial \phi}{\partial \dot{\boldsymbol{V_k}}} \tag{1.53}$$

Plus the complementary law for stress:

$$\boldsymbol{\sigma} = \frac{\partial \phi}{\partial \dot{\boldsymbol{\epsilon^p}}} \tag{1.54}$$

In practice the dual dissipation potential ϕ^*, obtained through the Legendre-Fenchel transform, is often preferred:

$$\phi^*(\boldsymbol{\sigma}, \boldsymbol{A_k}) = \sup_{(\dot{\boldsymbol{\epsilon}^p}, \dot{\boldsymbol{V_k}})} [\boldsymbol{\sigma} : \dot{\boldsymbol{\epsilon}^p} - A_k \dot{V_k} - \phi(\dot{\boldsymbol{\epsilon}^p}, \dot{V_k})] \tag{1.55}$$

We have then:

$$\dot{\boldsymbol{\epsilon}^p} = \frac{\partial \phi^*}{\partial \boldsymbol{\sigma}} \tag{1.56}$$

$$-\dot{\boldsymbol{V_k}} = \frac{\partial \phi^*}{\partial \boldsymbol{A_k}} \tag{1.57}$$

1.2.2 Extending to phase field models

The diffuse damage approach of fracture is usually concerned in representing the effect of damage on the macroscopic properties of the material, such as stiffness degradation or decreasing yield stress. It is an application of the local state method to fracture, and uses one or more internal variables to represent *damage*, a concept covering various irreversible material changes such as void nucleation or variations in the dislocation density.

Strain softening, that is to say the phenomenon of decreasing material stiffness when strain passes a certain critical deformation, poses an extra difficulty. Indeed, strain softening fundamentally changes the local differential equations making the problem ill-posed, with multiple numerical solutions [52]. In particular, in the presence of material softening the material is predicted to break along an infinitesimally thin surface: in numeric approximations, this translates as strain localisation in a single element regardless of mesh size. Ultimately, the size and localisation of the simulated crack will be mesh dependent.

The first solutions proposed to solve this problem consisted in using regularization techniques that contradict the main hypothesis of the local state method. Indeed, regularization techniques are based on the assumption that some variable are *non local* either by referring to a volume rather than to a point [53], or by operating through their spatial derivatives [54].

As noted by Borino and de Borst [52], this approach presents several drawbacks:

- While it can be rationalized using micro-mechanical arguments, the choice of the regularized variable is somewhat arbitrary and of great influence on the final result.
- The use of spatial derivative adds additional constraints when using finite element solvers: the shape functions differentiability class must be increased.
- First and foremost, the loss of the local state assumption means that automatic compliance with the second principle of thermodynamics is not guaranteed and must be ensured a posteriori.

The solution came under the form of phase-field models. Initially used to model nonequilibrium crystal growth [55], these models differ from the previous regularized approaches in the sense that the damage variable is integrated directly in the formulation of the potential energy. The

evolution law is then derived from the same energy than the other variables, and not from a different potential

1.2.3 Numerical implementation

All phase-field results presented in subsequent chapters were obtained using the Abaqus implementation proposed by Molnár *et al.* [50]. In this section we present this particular model in more details.

Damage field & crack topology

In this model, we consider a single internal variable: the damage d, dependent on both time and space. It is the crack phase-field function and varies between 0 (intact material) and 1 (completely broken). To represent micro-cracking and void nucleation, d varies smoothly between these values. Take for example an infinite bar of cross section Γ extending in the x direction. A sharp crack at $x = 0$ may be approximated by:

$$d(x) = e^{-|x|/l_c} \tag{1.58}$$

This exponential form is consistent with the sharp crack topology: $d(0) = 1$, $d(\pm\infty) = 0$ and if $l_c \to 0$ the damage will be null everywhere but at $x = 0$. In eq. (1.58) the length scale parameter l_c characterizes the diffuse crack topology: in a way, it measure the crack thickness.

An energy minimisation approach requires to determine the fracture energy, which is dependent on the size of new fracture surfaces in LEFM. In diffuse damage approaches, the *crack surface density* is constructed by analogy with the infinite bar case. Note that the exponential function in eq. (1.58) is solution of the differential equation:

$$d(x) - l_c^2 d''(x) = 0 \tag{1.59}$$

Any solution of eq. (1.59) will necessarily satisfy the condition:

$$d = \text{Arg}\left\{\inf_d I(d)\right\} \tag{1.60}$$

where we define the functional $I(d)$ as:

$$I(d) = \frac{1}{2}\int_{-\infty}^{+\infty} \left[d^2 + l_c^2 d'^2\right] dx \tag{1.61}$$

In the case of an infinite bar, $I(d = e^{-|x|/l_c}) = l_c\Gamma$. Recognising Γ as the crack surface in the sharp crack representation of a fully broken bar, we have by analogy in 1D diffuse damage representation: $\Gamma = I(d = e^{-|x|/l_c})/l_c$. We may generalize in higher dimension Γ as a function of the damage d present in any multi-dimensional body Ω:

$$\Gamma(d) = \int_\Omega \gamma(d, \nabla d) dV \tag{1.62}$$

where $\gamma(d, \nabla d)$ is the *crack surface density function*. It is simply the integrand of eq. (1.61) extended to 3D situations, divided by l_c:

$$\gamma(d, \nabla d) = \frac{1}{2l_c} d^2 + \frac{l_c}{2} |\nabla d|^2 \tag{1.63}$$

Potential energies

We introduce the Helmholtz free energy:

$$E(\boldsymbol{\epsilon}, d) = \int_\Omega \psi(\boldsymbol{\epsilon}, d) dV \tag{1.64}$$

The chosen free energy density is then expressed as:

$$\psi(\boldsymbol{\epsilon}, d) = g(d).\psi_0(\boldsymbol{\epsilon}) \tag{1.65}$$

where $\psi_0(\boldsymbol{\epsilon})$ is the usual strain energy and $g(d)$ a parabolic degradation function:

$$\psi_0(\boldsymbol{\epsilon}) = \frac{1}{2} \boldsymbol{\epsilon}^T \boldsymbol{C_0} \boldsymbol{\epsilon} \tag{1.66}$$

$$g(d) = (1 - d)^2 + k \tag{1.67}$$

where $\boldsymbol{C_0}$ is the undamaged material stiffness matrix and k a very small numerical stability parameter.

From eq. (1.48) and (1.66), it is possible to derive the state law defining the the stress tensor:

$$\boldsymbol{\sigma} = \rho \frac{\partial \psi}{\partial \boldsymbol{\epsilon}} \Rightarrow \boldsymbol{\sigma} = g(d) \boldsymbol{\sigma_0} = g(d) \boldsymbol{C_0} \boldsymbol{\epsilon} \tag{1.68}$$

where $\boldsymbol{\sigma_0}$ refers to the stress tensor of the undamaged material. Eq. (1.68) illustrates how the damage field impacts the stresses and degrades the material stiffness.

Because of the diffuse crack representation, we have to redefine the fracture energy. Making once more an analogy with standard LEFM, the fracture energy is expressed as the product between the critical energy release rate g_c and the crack surface defined in eq. (1.62)

$$W(d) = \int_\Omega g_c \gamma(d, \nabla d) dV \tag{1.69}$$

Finally, considering $k \approx 0$ the total potential energy of the system can be written as:

$$E_p(\boldsymbol{u}, d) = W(d) + E(\boldsymbol{\epsilon}, d) - \Pi^{ext}(\boldsymbol{u}) \tag{1.70}$$

$$= \int_\Omega [g_c \gamma(d, \nabla d) + (1 - d)^2 \psi_0(\boldsymbol{\epsilon})] dV - \int_{\partial\Omega} \boldsymbol{t}.\boldsymbol{u} dA \tag{1.71}$$

where $E(\boldsymbol{\epsilon}, d)$ refers to the free energy and Π^{ext} to the work of external forces $\boldsymbol{t}$ acting on the body boundary $\partial\Omega$.

Evolution law

One more equation is lacking to complete the model: we need to define the evolution law that will drive the expansion of the fracture phase-field d. It must ensure damage irreversibility: $\dot{d} \geqslant 0$.

Without detailling the derivation, which is available in [49], the minimisation of eq. (1.71) coupled with inequality constraints stemming from the second principle yields the Karush–Kuhn–Tucker (KKT) system:

$$\begin{cases} \dot{d} & \geqslant 0 \\ f - g_c \delta_d \gamma & \leqslant 0 \\ \dot{d}(f - g_c \delta_d \gamma) & = 0 \end{cases} \tag{1.72}$$

in which we introduced the variable f, dual of d: $f = \partial\psi/\partial d = 2(1-d)\psi_0(\boldsymbol{\epsilon})$ and the infinitesimal variation $\delta_d\gamma$:

$$\delta_d \gamma = \frac{\partial \gamma}{\partial d} - Div(\frac{\partial \gamma}{\partial \nabla d}) \tag{1.73}$$

$$= \frac{1}{l_d}(d - l_c^2 \Delta d) \tag{1.74}$$

If we consider the case when damage is increasing ($\dot{d} > 0$) the fourth equation of system (1.72) imposes that $f = g_c \delta_d \gamma$ which translates as the damage evolution law:

$$\frac{g_c}{l_c}\left(d - l_c^2 \nabla d\right) = 2(1-d)\psi_0(\boldsymbol{\epsilon}) \tag{1.75}$$

Resolution

For stability purposes, the problem is decoupled: the displacement field and the phase field are determined by two quasi-independent minimisations.

For each time step of the simulation, the phase field is updated first. From eq. (1.75), it is clear that damage is driven by the maximum stored elastic energy ever underwent by the material. We therefore introduce a history variable:

$$H_{n+1} = \begin{cases} \psi_0(\boldsymbol{\epsilon}) & \text{if } \psi_0(\boldsymbol{\epsilon}) > H_n, \\ H_n & \text{otherwise.} \end{cases} \tag{1.76}$$

Then, using a slightly altered potential energy, we get the evolution law of the damage field:

$$d_{n+1} = \text{Arg}\left\{ \inf_d \int_\Omega [g_c \gamma(d, \nabla d) + (1-d)^2 H] dV \right\} \tag{1.77}$$

In eq. (1.77), we consider only the terms dependent on d. This excludes Π^{ext}, as we assume that damage cannot reach the domain border $\partial\Omega$.

The displacement field is then determined as the minimizer of the difference between the potential

energy and external works:

$$u_{n+1} = \mathrm{Arg}\left\{\inf_{u} \int_{\Omega} \psi(\boldsymbol{u}, d_n) dV - \int_{\partial\Omega} \boldsymbol{t}.dA\right\} \tag{1.78}$$

The main assumption in this step is that d and $\boldsymbol{u}$ can not vary at the same time. This condition ensures numerical stability.

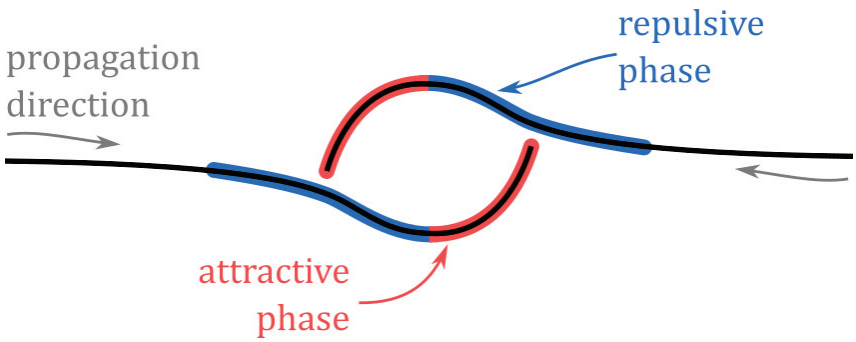

Figure 1.7 – **Typical hook-shaped configuration:** Two initially straight EP-cracks will, after getting close enough, enter a repulsive phase. They eventually turn into an attractive path until coalescence

1.3 Interacting cracks

Failure rarely occurs through the catastrophic propagation of a single crack. In practice, numerous microscopic defects are initially present in any structure; under solicitation many will grow and coalesce into macroscopic cracks. The problem of crack interaction, either at the microscopic or the macroscopic scale, is therefore of prime importance and has underwent large investigation. Multi-fracture problems are usually approached in one of two ways [56]: how individual cracks are affected by their neighbors, or how the presence of multiple fractures statistically alters the elastic properties of the material.

In the case of an array containing many cracks, two opposite behaviors are possible, depending on the relative positions of the cracks [57, 58]. Of course, because macroscopic cracks are the product of the coalescence of smaller fractures, the presence of many micro cracks can speed up propagation by increasing the SIF [56, 57]. On the other hand, macroscopic toughening by micro-cracking is a less intuitive, but also well known phenomenon. The presence of micro-cracks can increase the apparent fracture toughness by reducing the material stiffness around the crack tip, or by locally releasing residual stresses [59, 60].

The dominant mechanism (stress shielding or stress amplification) is highly dependent on the relative position of the interacting cracks. It is therefore critical to understand the mechanism behind two-cracks interactions. This situation poses challenges as a coupled and non-local problem: each increment of crack propagation is entirely determined by the stress field surrounding the crack tip, which is in turn influenced by the presence and propagation of other cracks. Just as in many-cracks array, crack-crack interaction can either shield (or even arrest) their development or, on the contrary, cause a sudden jump of propagation [61].

1.3.1 Some observations on EP-crack pairs

Careful examination of crack coalescence also requires to examine how interaction can induce path deflection. The family of fracture problems known as *en-passant* (EP-cracks) is an excellent example of how a seemingly simple situation can yield widely different final propagation paths.

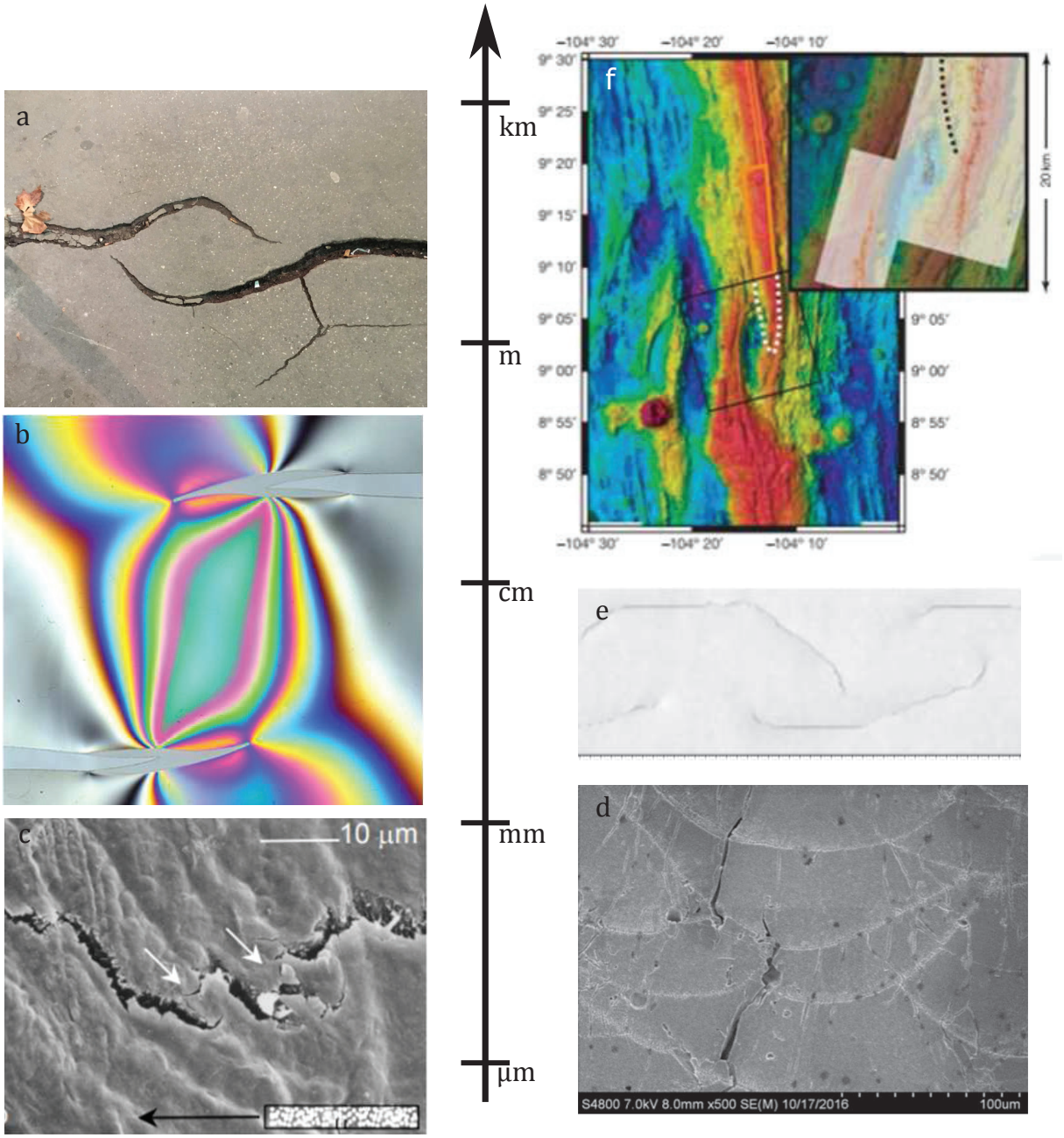

Figure 1.8 – **EP-cracks examples:** the hook shaped propagation paths can be observed at scales ranging from a few micrometers to several kilometers.
(a) in an asphalted road;
(b) in a plastic sheet, adapted from [2];
(c) in human cortical bone adapted from [62];
(d) in 3D printed aluminum alloy, adapted from [63]
(e) in a paper sheet, adapted from [64];
(f) in oceanic floor, adapted from [65].

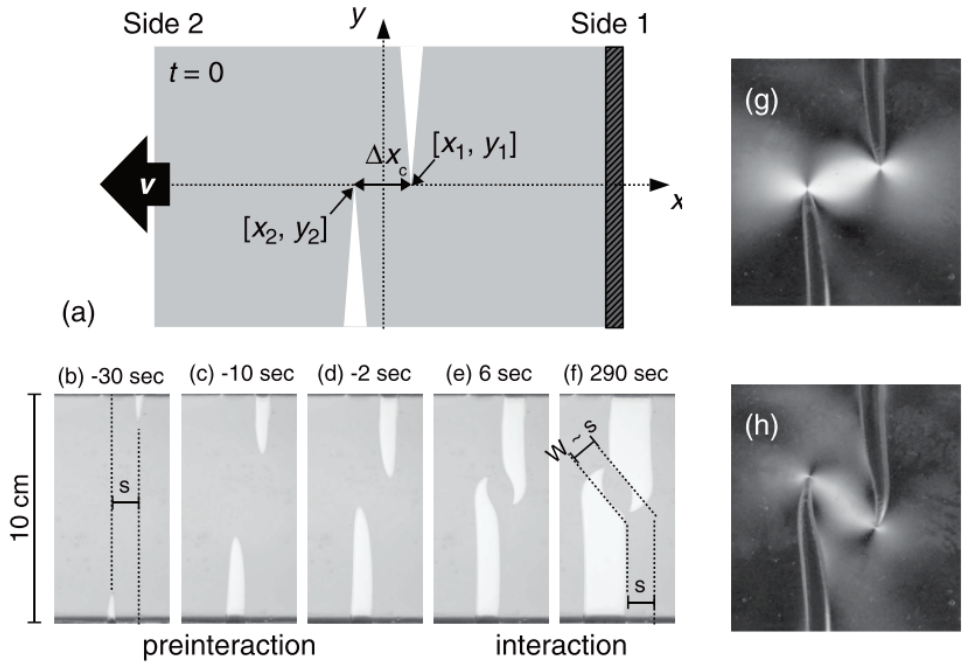

Figure 1.9 – **Fender *et al.* experiment:** (a) Set-up schematics, (b)-(f) Propagation dynamics, (g)- (h) Example of a fractured gelatin sheet: the repulsion is negligible. Taken from [1].

EP-cracks refers to the configuration in which two initially collinear and offset cracks propagate inward, i.e toward each other. They generally exhibit a surprising repulsive behavior: counter-intuitively, EP-crack pairs do not join tip to tip. Indeed, when the cracks are not yet superimposed, the lateral separation between the tips usually *increases* as the cracks approach each other. The cracks will later turn, usually at superimposition or slightly before, and grow toward each other until they join (see Fig. 1.7). As shown in Fig.1.8, the resulting hook-shaped propagation path is characteristic of EP-cracks and have been observed in a wide variety of materials and at a broad range of scales.

The name "en-passant" was first coined by Kranz [66] when he observed this type of interaction as a basic type of micro-crack linking mechanism in rocks. In this case, the cracks were only a few micrometers long. Since then, the term was re-used to designate any fracture problem containing two parallel cracks approaching each other. In particular, kilometers long EP-cracks are frequently observed at the geological scale in pack ice [67] or along rift zones in planetary crusts [68, 69], under the name of "overlapping spreading centers". At the micro-scale, examples of en-passant like cracks a few hundreds micrometers long are visible in biological tissues such as dental enamel [70], bones [62, 71–73], or antlers [74], where they are known to act as toughening mechanisms. Recent industrial applications gave way to even smaller en-passant like fracture configurations: the thin metallic films used in stretchable electronics often contain many parallel cracks separated by only a few micrometers [75–77]. Other examples of en-passant cracks of similar length are also present in 3D printed alloys [63] or mechanical sensors [78].

Considering how ubiquitous en-passant cracks are, there is a remarkable dearth of controlled experimental studies of this configuration.

Laboratory observation of EP-cracks can be accidental, as they often are the sub-product of mode

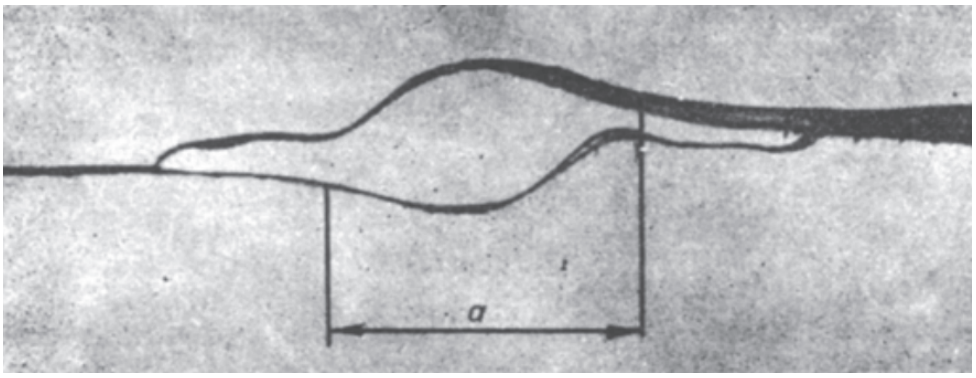

Figure 1.10 – **EP-cracks in Plexiglas:** the strong repulsion before overlap was observed by Eremenko *et al.* [79].

I+III propagation: small, hook-shaped, en-passant cracks can form in the direction transverse to the main cracks [80]. Cortet *et al.*[64] did not study EP-cracks directly, but a similar configuration: two lines of collinear cracks form a repeated en-passant pattern. Even with these modified initial conditions, clear hook-shaped paths with repulsive and attractive phases are observed (see Fig. 1.8e). Theocaris [81] limited his study to collinear EP-cracks propagating into Plexiglas: he found that, in this configuration, interaction effects were negligible if the tip to tip separation distance was greater than twice the crack length.

Fender *et al.* [1] presented the first examination of the shape of EP-cracks propagating in various relatively soft materials (gelatin, cork, polystyrene foam and aluminum foil) and proposed that the paths have a universal square root shape, governed exclusively by the initial offset between the cracks. While the results from this experiment are remarkably self-similar, the repulsive component in the resulting crack paths was systematically neglected. As shown in Fig. 1.9), it was in their case small but still visible and remains an important feature of the hook-shaped path of EP paths. Indeed, we usually expect EP-cracks to repel one another at the onset of propagation and to attract one another only after the inner tips are superimposed. As shown in Fig. 1.10, this was observed by Eremenko *et al.* [79] during experiments conducted in Plexiglas, as well as in many geological settings [66, 82, 83]. It should be noted however that repulsion between EP-cracks can be almost imperceptible: Swain and Hagan [82] needed to magnify the overlap region to reveal the slight repulsion present in their experiments conducted in soda-lime glass.

To the best of our knowledge the only comprehensive examination of the repulsive component of EP-cracks paths, its magnitude and its controlling parameters, was conducted by Dalbe *et al.*[2]. When studying EP-cracks propagating into three different kinds of polymer films, they found results startlingly different from Fender's: not only distinct repulsion between the cracks was almost systematically present, but the previous shape universality is lost. Some features are similar: the final shape is not dependent on the horizontal separation between the cracks and they attract one another eventually. However, the turning point between repulsion and attraction happened before overlapping and the final crack path is strongly influenced not only by the initial offset between the cracks but also by the material properties (See Fig. 1.11). As shown in Fig. 1.12, the maximum angle of repulsion was systematically stronger for cracks propagating in

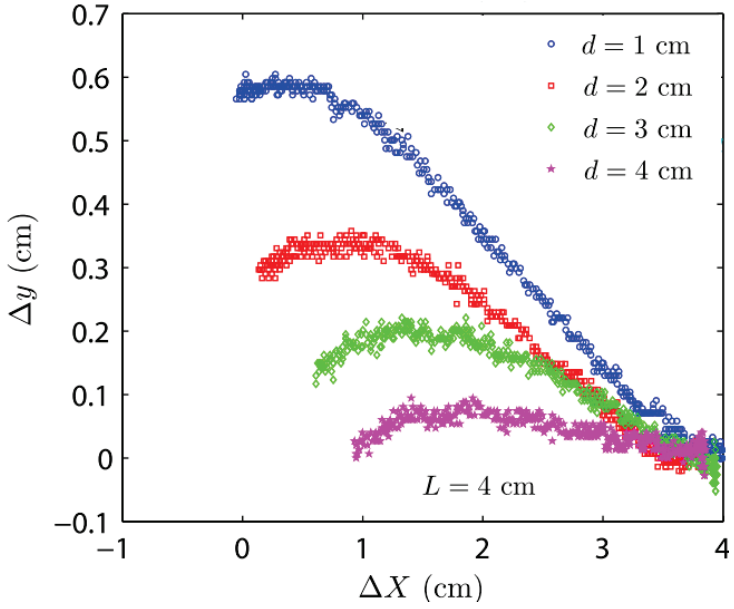

Figure 1.11 – **Dalbe *et al.* trajectories:** The lateral separation Δy is represented as a function of Δx, the separation in the crack axis direction for different d, the original offset between the cracks. In this case, the repulsion to attraction transition occurs before overlaping ($\Delta X = 0$). Adapted from [2].

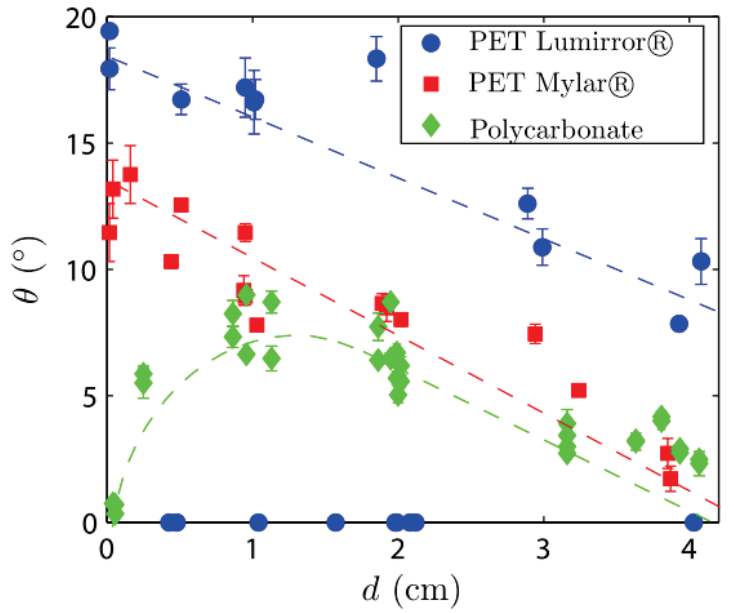

Figure 1.12 – **Maximum repulsion angle vs. lateral separation:** The two different PET sheets, Lumirror®and Mylar®had the same Young's modulus and Poisson ratio. The systematically smaller repulsion in the PET Mylar®was attributed to phenomena occurring at a scale small enough for LEFM to become inapplicable. Adapted from [2].

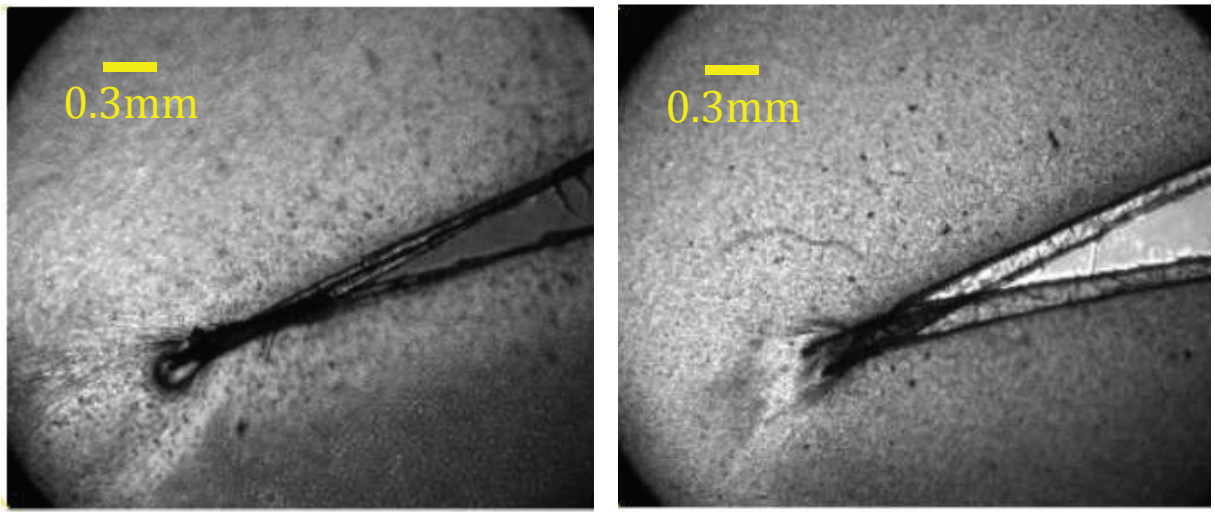

Figure 1.13 – **Close-up of the crack tips and surrounding plastic zones:** We assume that the fracture process zone appears in black, as it contains voids and micro-cracks that will obstruct the light.
(a) The PET Lumirror®endures the most repulsion and seems to be associated with a narrower process zone;
(b) PET Mylar®. The "double tip" visible in this sample is probably an artifact caused by out-of-plane deformation. Adapted from [2], Supplemental Material.

polyethylene films rather than in polycarbonate films. Even more surprisingly, it appeared that taking into account the Young modulus and the Poisson's ratio, i.e. the material properties used in a LEFM model, would not be sufficient to fully explain the different final path shapes. When identical tests were run for two separate kinds of polyethylene sheets that had identical macroscopic properties, the magnitude of repulsion was also systematically larger in one case. This clearly shows a failing of a LEFM approach to study interacting cracks in such material samples as the only noticeable difference between the two tests was the shape of the plastic zone around the crack tips, shown in Fig. 1.13. The discrepancy was tentatively attributed to the different micro-structures of the materials, and how it may impact the fracture process zone ahead of the crack tips: strong repulsion appears at first glance to be associated with a "sharper" point of the fracture process zone. Finally, Dalbe *et al.* noted an even more surprising disparity: while the PLS, as well as as other bifurcation criteria, predicts that perfectly aligned cracks propagate straight ahead, maximum repulsion is observed for this configuration specifically.

This effect was further examined by Koivisto *et al.* [3] who reproduced the previous experiments in polycarbonate sheets and used digital image correlation to track the tips of the fracture process zone and measure the strain fields. The authors found that, when treating the process zone tip as an effective crack tip, the cracks follow LEFM theory with a maximum tangential stress assumption. Crack repulsion is then considered as an exceptional, rather than usual, phenomenon: according to the authors, it could only result from a stress field perturbed by a large fracture process zone.

The presence of an attractive phase following a repulsive stage is not the only distinctive characteristic of EP-crack paths. The results of Dalbe *et al.* are also surprising because the attractive

phase begins before overlapping when a starting point at coincidence is the general consensus [66, 69, 79, 82, 83]. EP-cracks are also known to coalesce at a near perpendicular angle [66, 84]. Finally, the shape factor of the released central part between the cracks is generally reported to be 3:1 [69, 85, 86]. However in a minority of cases, the central part is more elongated: observing normal faults Acocella *et al.* reported a small number of large aspect ratios, up to about 10:1 [69]. To our knowledge a more circular central part, with a ratio of 2:1 was observed in only one instance [1].

1.3.2 Modelling interacting cracks

General techniques for studying interacting cracks

Most studies specifically on two-cracks interactions are focused on the determination of the SIF, and do not extend the reasoning to the identification of the complete crack paths. Techniques to compute the SIF often rely on the stress superposition principle [87]. The first method of this family was introduced by Kachanov [88]: the problem containing N cracks is represented as the superposition of N subsidiary problems consisting of one isolated crack, loaded from both the original tractions, and a sum of *unknown interaction tractions* induced by the other cracks. Simplifying hypotheses, such as the one proposed by Kachanov (any interaction traction is taken as the response of a crack to the *uniform average* traction on the other) makes for an easy solving of the problem. This technique, which was later re-branded as the "pseudo-traction method" by Horii and Nemat-Nasser [89], has benefited from many enrichments in the form of tractions hypotheses: instead of using constant tractions along the considered crack, Horii and Nemat-Nasser used polynomials of the Chebyshev's and Taylor's kinds. Benveniste *et al.* [90], also used a polynomial approximation to represent the tractions: in this case polynomials are used on all the cracks, not just the one in the current sub-problem.

Pseudo-traction methods are simple and adaptable to many fracture problems; they are, however, limited to straight cracks and thus unable to determine complex curved final paths. They also become imprecise for small crack spacing, making it all the more irrelevant to the study of crack coalescence or close crack interaction [87].

Another often used technique to study interacting cracks consists in representing them by a distribution of infinitesimal dislocations in an otherwise perfect body [91]. This "distributed dislocations technique" was first introduced by Bilby and Eshelby [92] and further refined later by Hills *et al.*[91]. The final solution is the superposition of two problems: a trivial one consisting of the given geometry and loading from which we removed all cracks, and an auxiliary problem containing the cracks but no far-field loading conditions. The cracks are represented by an assembly of glide and climb dislocations to account for any displacement jump. The stresses are then retrieved using the well-known Burger's theory [93].

Recently, but dislocations-based methods were extended to determine the SIF not only at cracks tips, also at other stress singularities such as crack kinks [94, 95]. This allows the study of crack branching in the context of LEFM. The main advantage of dislocation based methods is

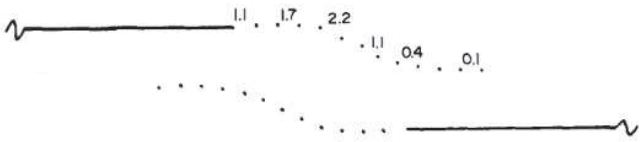

(a)

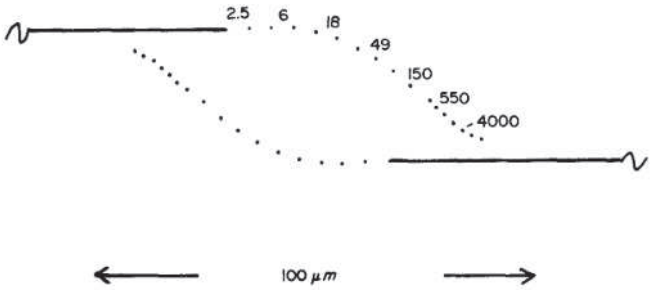

(b)

Figure 1.14 – **Predicted EP-cracks paths by Mills and Walker:** Adapted from [98] The cracks are subjected to a far removed tensile stress and the numbers above each increment stand for the energy release rate.
(a) Paths for a *pair* of cracks: the authors did not retrieve the expected hook shape, but an unanticipated "s" shape.
(b) Paths for an *infinite array* of EP-cracks. Note that in both case the repulsion between the cracks is negligible.

that they are usually less numerically costly than FEM analysis, and extend well to the case of multiple curved cracks. However, these methods are generally considered to be more suited to study relatively short cracks [91] and may prove inadequate for a problem with known multi-scales properties such as EP-cracks. Furthermore, dislocations methods are only valid for purely elastic materials and do not allow to study the effect of plasticity [96].

Some models of *en-passant* crack pairs

Many studies concerned with the propagation direction of interacting crack are usually focused on very specific geometries and offer only a partial analysis of the problem.

Melin [97] restricted her work to the case of a periodic array of perfectly collinear cracks. Using a dislocation method, she showed that slight curvature at the tips of the otherwise straight cracks induces crack repulsion and impedes tip to tip coalescence. The inquiry was focused on the initial behavior of the cracks, and the final path was not comprehensively described.

Mills and Walker [98] also studied an infinite and periodic array of cracks using a dislocation

method. In this case the cracks are entirely curved and approximated by a succession of straight displacement discontinuities. Mills and Walker were able to retrieve the classic hook shape in a periodic array: a repulsive phase is followed by an attractive phase when the cracks overlap. However, the cracks intersect at an angle of about 38° (see Fig. 1.14a), which is markedly smaller than the 90° angle usually observed. When applied to a pair of cracks, their method revealed that propagation at the inner tips should eventually stop for the benefit of propagation at the outer tips. Also, the complete path shown in Fig. 1.14b was not hook-shaped; the attractive phase does not last until coalescence as the cracks eventually deviate a third time and end up parallel to each other. Mills and Walker attributed these phenomena to artifacts of the dislocation method but, depending on the tested geometry, it could be in accordance with later results [57, 99].

Yokobori *et al.* [100] used a dislocation method to study narrowly spaced EP-cracks, under the assumption of the MTS. The results are somewhat contradictory to the general consensus: Yokobori *et al.* found that EP-cracks do not deviate from their original axes before overlapping, and that repulsion could begin *after* superimposition of the inner tips. This is, to the best of our knowledge, the only occurrence where such a phenomenon is reported; we attribute this discrepancy to the known failings and inaccuracies of dislocation methods. Chan [101] tried to re-simulate Yokobori's trajectories using another dislocation method on the exact same geometry and boundary conditions: he found that the cracks repel one another before overlapping, further invalidating Yokobori's model.

Baud and Reuschlé [102] studied EP-cracks submitted to either tensile or compressive far-away stresses. Surprisingly, this dramatic change in boundary conditions does not significantly affect the qualitative form of the final shape: again, the trajectories are hook-shaped. This model presents two failings: any predicted repulsion is very weak, and the cracks interact only if they stand really close to each other. Indeed, the maximum tip to tip interaction distance is the half-length of the crack, which is smaller than other models predict.

For example, Gdoutos [99] found the interaction between EP-cracks to be significant if the tip to tip separation distance is smaller than twice the crack length. Gdoutos used previous work to identify the SIF [100, 103] and determine the initial kink angle of the cracks as defined by the strain energy theory: depending on the geometry both repulsion and attraction are possible. Gdoutos also compared the energy release rate at the outer and inner tips, which enabled him to determine from which extremities the cracks would propagate.

Wang *et al.* [57] were interested in EP-cracks as a mechanism of crack coalescence: using known solutions for the SIF neighboring cracks, and assuming the MTS hypothesis, he determined complete EP-cracks trajectories. It should be noted however that the known solutions he used are only available for straight cracks in an infinite medium; the influences of both the boundary conditions and the history of the crack propagation were necessarily neglected. While the resulting paths can not be considered quantitatively accurate, Wang *et al.* were able to qualitatively retrieve the hook-shaped paths of EP-cracks and concluded that the presence of a repulsive phase is exclusively dependent on the lateral, i.e. in the direction transverse to the original cracks axes, distance separating the original tips.

Forsyth [104] adopted a similar approach to determine EP-cracks paths, along which he determined theoretical plastic zones whose size was proportional to K_I^2. He argued that the turning point of the paths or, in other words, the moment the cracks behaviour changes from repulsive to attractive, corresponds to the moment the plastic zones encroach one another. This assumption was poorly justified and no explanation of the magnitude of repulsion was presented.

Sempere and Macdonald [85] successfully modelled overlapping spreading centers, that is to say immense EP-cracks found along rift zones, as two initially parallel cracks in a tensile far away loading using a dislocation method: repulsion is observed in certain configurations and the ratio of the released piece between the cracks was always about 3:1, comparable with sea-floor observations.

More recently, Ghelichi and Kamrin [105] presented a set of analytical tools based on the superposition principle to study EP-cracks but did not explicitly study the complete trajectories. This technique allows a very precise determination of the SIF at the tips of a curved crack propagation increment, but it relies on the knowledge of the T-stress, i.e. the second order term in the stress expansion around the crack tip, which is arduous to calculate in interacting crack situations [106]. Although the trajectories were not studied in terms of attraction or repulsion, the changing sign of K_{II}^* suggests that both behaviours can be retrieved with this technique.

1.3.3 Remaining questions & research objectives

As we have seen, conflicting affirmations have been put forward to explain the behavior of EP-crack pairs. In particular, the conditions necessary to induce repulsion and the parameters controlling its magnitude remain unexplained. While most observations and many theoretical work confirmed its ubiquity, the only two deep analysis of experimental EP-cracks paths yield confusing results: Fender *et al.* [1] did not observe repulsion and concluded to the existence of a universal shape that clearly conflicts with the majority of observations and Dalbe *et al.* [2] discovered surprising phenomena that call into question the validity of the LEFM framework to study EP-crack pairs.

Few hypothesis have been put forward to suggest the origin of repulsion between EP-cracks. Melin's work [97] suggests that heterogeneity-induced perturbations could be the source of this instability, but Cortet *et al.* [64] later found that any inhomogeneities in the material would have to be unrealistically large to explain the whole magnitude of the repulsion he observed. Other authors [3, 104] attributed the repulsion to the presence of a significant plastic zone around the crack tips. However, the most recent conclusion in that regard [3], that repulsion is induced exclusively by the presence of a process zone and that larger process zone would lead to stronger repulsion, is debatable considering previous work where repulsion was predicted by purely linear elastic approaches [99, 102, 105]. Dalbe's explanation [2], i.e. the repulsion intensity depends on the *shape* of the plastic zone rather than its *size*, seems more credible.

These apparently contradictory works raise three main questions:

- Under which conditions does the LEFM framework, under the assumption of the PLS

predict EP-cracks repulsion ?

- Is the observation that the maximum repulsion between EP-cracks is realised when the cracks are aligned really a failure of LEFM, or is it possible to explain the contradiction ?
- How can we explain that macroscopically similar materials yield different crack paths ?

Our first objective is to delineate once and for all the real limitations of a LEFM framework applied to EP-crack pairs by conducting a precise and systematic analysis of the initial kink angle θ_i, as predicted by the PLS. In that respect, we developed a fast and versatile tool presented in section 2.1 that allowed us to repeat the computation of θ_i for many EP-cracks configurations. The corresponding results shown in section 2.2 confirmed that a LEFM+PLS approach is not inherently unfit to model the repulsive component of EP-crack pairs. A deeper study of the complete trajectories was therefore desirable; we detail the method used to determine them in section 2.3 and the results in section 2.4. We later on investigated how a diffuse damage modelling affects the results as it let us test Dalbe's hypothesis by controlling the crack bluntness. This set of prospective results is presented in chapter 3.

Chapter 2

LEFM study of EP-crack pairs

Contents

In this chapter, we wish to conduct a thorough study of EP-crack pairs in the LEFM framework, first to clarify if repulsion can be *qualitatively* anticipated using this model. To that aim we determined the initial kink angle of EP-cracks loaded in a tensile stress field. Repeating the computation for many crack lengths and tip to tip separation distances allowed us to identify the precise geometric conditions leading to crack repulsion within this theoretical context.

In a second phase, we wish to complete our study by comparing simulated trajectories to the ones obtained experimentally by Dalbe *et al.* [2] in plastic films. In particular we seek to verify whether LEFM predictions of the magnitude of repulsion between EP-crack pairs can be *quantitatively* accurate.

Given the arguments in favor of the PLS outlined in section 1.1.3, all kink angles and trajectories in this chapter will be identified under this assumption, unless otherwise specified.

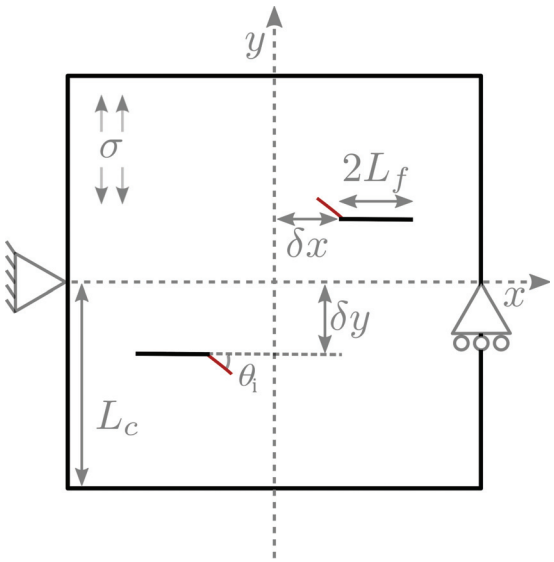

Figure 2.1 – **Parameters definition:** Geometric definition and boundary conditions used in the finite element analysis of the initial kink angle θ_i of EP-cracks. θ_i is measured between the original crack direction and its *virtual* extension. In our convention, the behaviour is considered repulsive when $\theta_i < 0$ and attractive when $\theta_i > 0$ in the counter-clockwise direction. Here, the example is drawn in the repulsive case.

2.1 Determining the initial kink angle

2.1.1 Problem definition & computation

Procedure

For this first step, our aim is to focus on how two-cracks interaction affects the initial kink angle while minimizing the impact of boundary conditions on the cracks propagation direction. To do so, we examine the case of a square plate notched with symmetric cracks significantly smaller than the length of the plate sides. As shown in Fig.2.1, this configuration is defined by four parameters: the half side length L_c, the half crack length L_f and the tip to tip separation distances $2\delta x$ and $2\delta y$. We are interested in determining $\theta_i(L_f, \delta x, \delta y)$, the initial kink angle formed between a crack and its extension. In the initial configuration the cracks are rectilinear and oriented perpendicularly to the applied stress: if only one was present, it would be solicited in pure mode I and propagate straight ahead ($\theta_i = 0$) according to the PLS and other bifurcation criteria. We therefore distinguish between two types of interaction: the cracks repel one another if they are deviated from their straight, when alone, path in the direction going away from the second crack ($\theta_i < 0$). Alternatively, we consider the interaction to be attractive when $\theta_i > 0$.

In accordance with the LEFM hypothesis, we only consider an ideally linear elastic, isotropic and homogeneous material for all scales considered.

As we have seen in section 1.1.3, to determine the θ_i that satisfy the PLS, we need to solve $K^*_{II}(\theta) = 0$, with K^*_{II} being an universal polynomial function dependent on the SIF *before kinking* K_I and K_{II}.

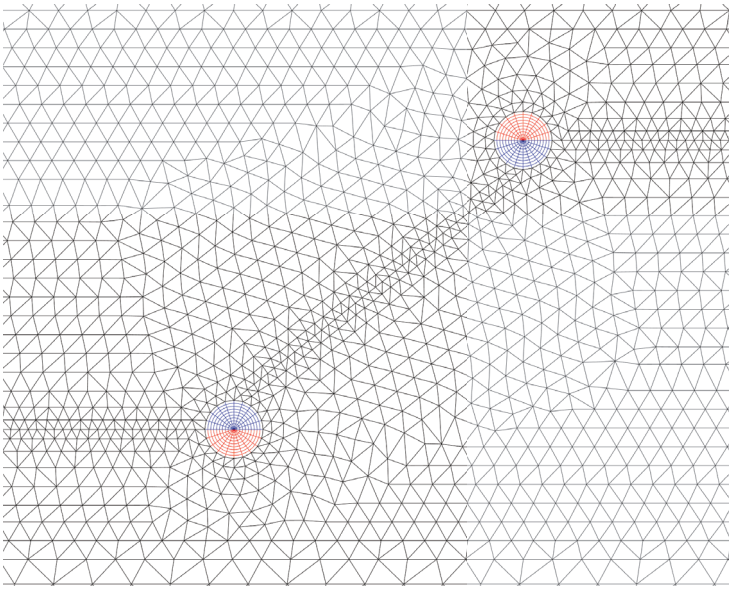

Figure 2.2 – **Regular layered mesh:** Close-up on the mesh around the inner crack tips. In this instance the regular mesh contains 10 layers. The $G(\Theta)$ procedure is applied on the outermost colored line.

Therefore, our scheme to determine θ_i amounts to two steps: a simple finite element analysis to compute K_I and K_{II} and a classic minimization algorithm to solve $K^*_{II}(\theta) = 0$. We used the freely available Cast3m finite element software [42] to determine the stress state of our problem, and a pre-implemented procedure [107] to compute the SIF based on the $G(\Theta)$ method presented in section 1.1.4.

Mesh definition

Given the simple geometry defined in Fig. 2.1, we have only three meshing parameters to choose:

- The radius L_r of the circular contour inside which the SIF will be calculated,
- the size h of the regular mesh enclosed in these contours (see Fig. 2.2),
- the mesh size on the outer borders of the plate.

In the subsequent section, we will present the various situations tested to determine the optimal meshing characteristics to study EP-crack pairs.

2.1.2 Validation: precise SIF determination

We first conducted a convergence study to determine which meshing characteristics and other numeric conditions should be respected to obtain satisfactory precisions when computing the SIF. In that order, we compared simulation results to analytical solutions known for specific interacting crack configurations (see [56] for reference).

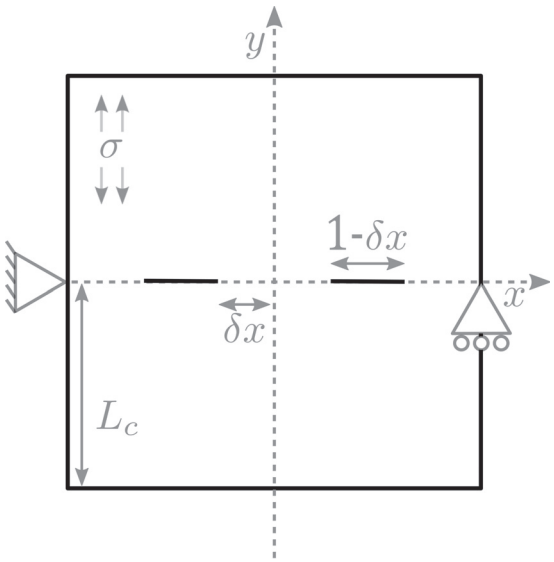

Figure 2.3 – **Test case configuration:** Geometric definition and boundary conditions used to test the validity of the far-field assumption. The same arrangement was reused to identify the meshing conditions necessary to reach statisfying precision.

Far-field loading approximation

Ideally, the study of two-cracks interaction should be undertaken in an infinite medium to remove the influence of boundary conditions. This is possible analytically only for specific crack arrangement and not at all using finite element analysis. The far-field tensile loading was then represented in our FEM simulation by taking the plate several order of magnitude bigger than the cracks.

To test this hypothesis, we compared the results obtained analytically in [56] for two cracks standing on the same line, in an infinite medium under far-field opening stress, to a similar configuration in a plate of varying finite size L_c, as shown in Fig.2.4. Figure 2.4 (a) and (b) show the computed outer and inner tips SIF rescaled by K_I^0, the SIF for a single crack in a similar medium. The computed values reproduce well the influence of crack interactions when the distance δx decreases. Figure 2.4 (c) and (d) show that the relative error, compared to the analytical prediction in an infinite plate, is very small for a plate size to crack length ratio $L_c/L_f = 20$ and can reach about 3.5% in the worst case where $L_c/L_f = 5$, i.e. when the boundaries of the plate can not be considered at infinity and finite size effects are important. As the error decreases quickly with the plate size, we are confident that a ratio of $L_c/L_f = 20$ is sufficient to reach a satisfactory approximation of an infinite plate.

Influence of the meshing parameters

The main numerical challenge here is to ensure an accurate description of the stresses in the areas of interest, despite the crack tips acting as close standing mathematical singularities. The $G(\boldsymbol{\Theta})$ procedure should be applied inside a contour enclosing the crack tip, the size of which should be chosen carefully. Indeed, the contour cannot be too large and intersect the second crack but

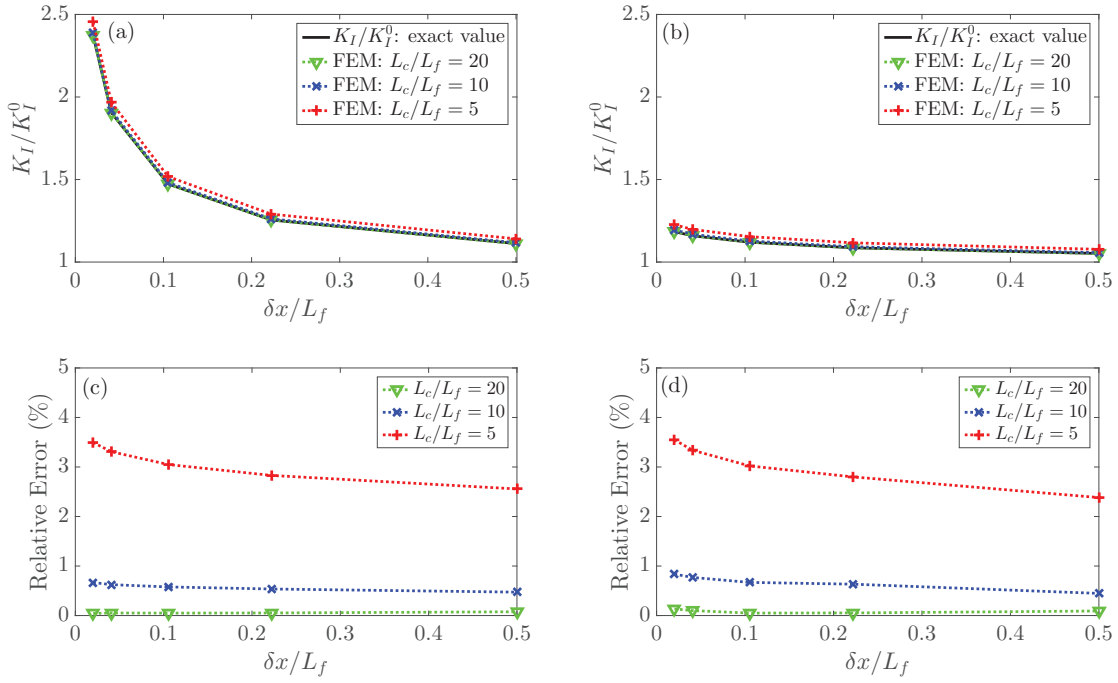

Figure 2.4 – **Far-field loading assumption:** Evolution of the first SIF and relative error compared to analytical predictions (for an infinite plate) at the inner (a,c) and outer (b,d) crack tip as a function of δ_x/L_f Different plate sizes were used to identity the minimum L_c/L_f ratio for which crack interaction effects dominates over the influence of boundary conditions.

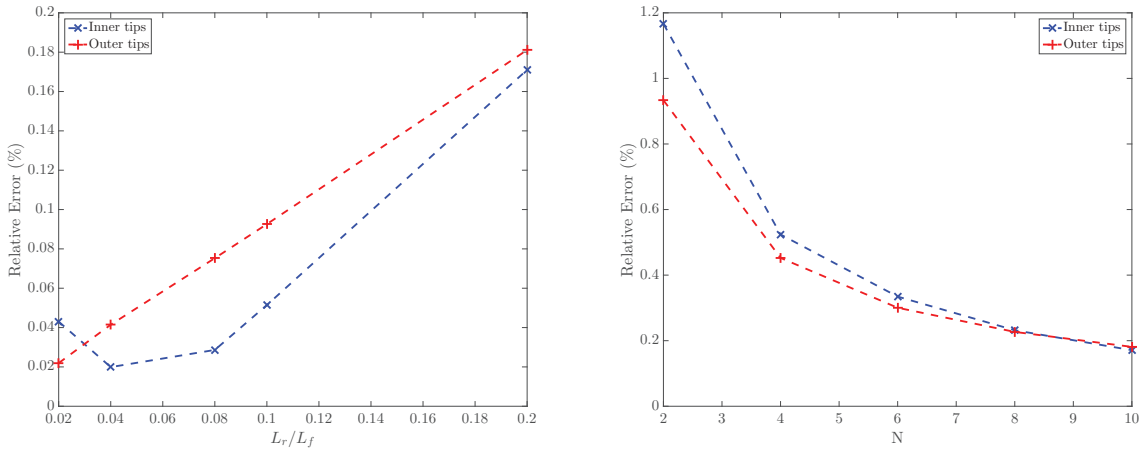

(a) (b)

Figure 2.5 – **Influence of the meshing parameters on the SIF determination precision:** The horizontal spacing between the cracks is fixed to a value of $\delta x = 0.2$. (a): The precision is inversely proportional to the size of the integration contour and (b) proportional to the number of regular mesh layer separating the tip and the contour. In both case this could be at least partially attributed to the changing mesh size around the crack tips.

it should not be too small either, as the stresses will be less precisely calculated too close (in terms of number of meshes separation) to the stress singularity. The remaining question is then how large should the contour radius L_r be comparatively to L_f, and how many meshes should it enclose.

Comparing again simulations to the analytical solution for two collinear cracks in an infinite medium, Fig.2.5a represents the evolution of the relative error as a function of the ratio L_r/L_f. In each case the contour contained a 10-layers regular mesh around the crack tip (see Fig. 2.2): it appears clearly that the decreasing mesh size completely cancels out any disadvantage of small L_r/L_f ratios. In any case, the maximum relative error of 0.2% could be attributed to the model approximation and excellent precision is easy to reach even for close interacting cracks, as long as a sufficient number of nodes separates the tip from the contour. The influence of this number N on the relative error is displayed in Fig.2.5b where we represent the relative error as a function of the number of regular mesh layer in a contour of fixed size L_r. Again the effect is coupled with the decreasing mesh size and excellent precision is reached for $N = 10$ which correspond here to a mesh size around the tips of $h = 0.02L_f$.

2.1.3 Final meshes characteristics

The work presented in section 2.1.2 allowed us to establish the fitting computational parameters for our study. All results presented in section 2.2 were obtained using meshes of the following characteristics:

We used quadratic triangular finite elements everywhere, with the exception of the regions around the cracks tips. They were refined in order to reach a $h \in [0.0002L_f; 0.005L_f]$ mesh size depending on the geometry, and we enforced a regular mesh of quadrangular quadratic elements in a 10 nodes radius so that the SIF determination using $G(\mathbf{\Theta})$ procedure is as precise as possible. To save computation time, the mesh size was gradually increased toward the edges of the plate, so that the outermost mesh size was about 1200h. The plate half sides length L_c was taken constant across all computations, while L_f varied so that the ratio L_f/L_c fell between 20 and 1000, which is sufficient to ensure minimal influence from the boundary conditions. Rigid body modes are restrained by clamping the midpoint on the plate left side and only allowing displacement along Ox for the opposing point. The horizontal sides are pulled apart by imposing a stress uniformly on the top and bottom sides in the σ_{yy} direction.

The efficiency and robustness of our calculation allowed us to repeat the computation for many points: finally, K_I and K_{II} were determined for over 7500 $(\delta x; \delta y; L_f)$ combinations. One limit of this representation is that we deliberately chose to not consider potential contact between the crack lips, as it saves computation time. This is of no incidence as long as the first mode of fracture dominates over the second, which is the case in a far-field tensile loading.

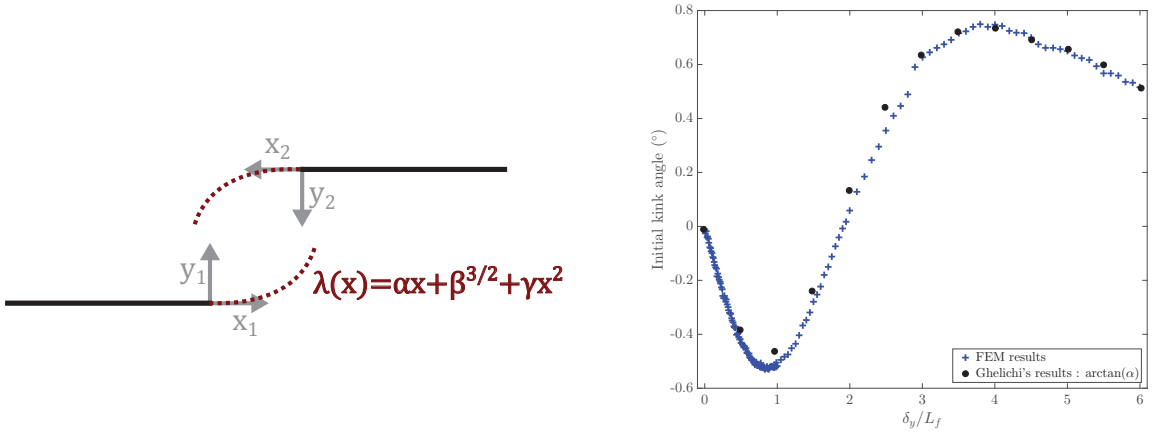

Figure 2.6 – **Evolution of the initial kink angle versus the lateral separation:**
(a) Coordinate system used to describe a curved propagation increment.
(b) Here δ_x/L_f is fixed to a value of 2.5, and we compare our simulation results to data extracted from Ghelichi's work [105].

Verification for interacting cracks

In a second step, we verified the validity of our model specifically for EP-cracks by comparing our results with the ones obtained by Ghelichi [105] who also studied EP-cracks in a LEFM context but using different techniques from finite element analysis. Amestoy's formulas allow to determine only the direction of the next (straight) propagation increment. However, Ghelichi went further by determining analytically the SIF after propagation of interacting cracks using a curved increment depending on three parameters:

$$\lambda(x) = \alpha x + \beta x^{3/2} + \gamma x^2 \tag{2.1}$$

where λ and x are the coordinates along the propagation increment, in a Cartesian coordinate system centered on the original EP-crack tip. We derived from there an equivalent initial kink angle $\theta_i = \arctan(\alpha)$. Comparison of our results with Ghelichi's is presented in Fig. 2.6: the excellent agreement between our simulations and the θ_i derived from Ghelichi's work validates both the precision of the FE computation step and the use of a minimization algorithm based upon Amestoy's formulas (see Eq. (1.40)) to determine the initial kink angle of close standing EP-crack pairs.

While Ghelichi's work gives a more accurate description of the next propagation step, only the linear approximation of the curved increment is necessary to determine the cracks propagation direction and our method has the benefit of relying exclusively on simulation methods well known by engineers and simple analytic equations.

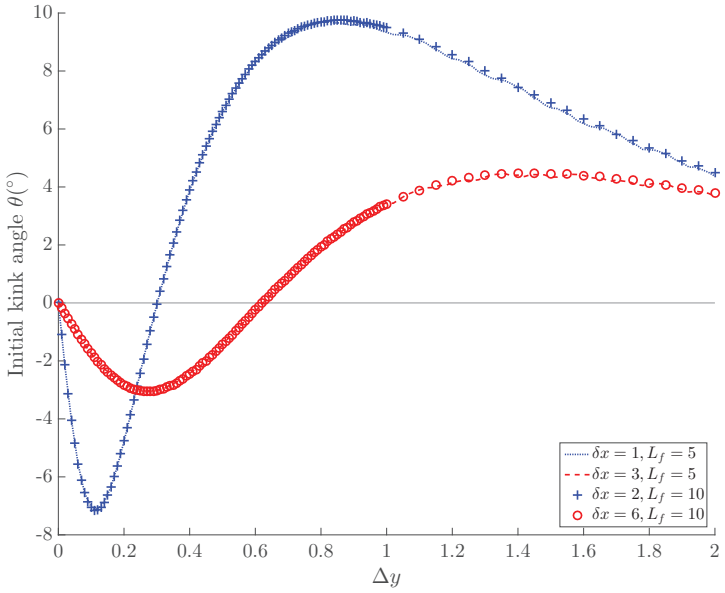

Figure 2.7 – **Rescaling properties:** Evolution of θ_i with scaled tip to tip spacing $\Delta y = \delta y / L_f$ for four sets of $\delta x, L_f$ values: curves with identical $\Delta x = \delta x / L_f$ match.

2.2 Scaling properties of the initial kink angle

The problem of two EP-cracks in a quasi-infinite medium is defined by 3 length scales: assuming L_c is large enough to render boundary effects negligible, the geometry of the cracks is then controlled by L_f, δx and δy. We found however the situation reduces to a set of only two dimensionless parameters: the scaled tip to tip relative separation distances $\Delta x = \delta x / L_f$ and $\Delta y = \delta y / L_f$. We represent in Fig. 2.7 the evolution of $\theta_i(\Delta y)$ for various δx and L_f: the different evolutions collapse on a set of master curves depending on the Δx value.

This property allowed us to compute θ_i for extremely small values of Δx and Δy by choosing large crack lengths. By charting scaled separation distances of the order of 10^{-2} and smaller, we unveiled the non-monotonic dependency of the initial bifurcation angle with the geometric conditions, thus providing a broad insight as to which EP-crack pairs will initially attract or repel one another. We will comment more on this behaviour in the following section.

2.2.1 An attractive to repulsive transition

We found that the typical variation of θ_i with Δy belongs to one of three kinds, depending on the fixed Δx value; non-overlapping cracks ($\Delta x > 0$), coincident cracks ($\Delta x = 0$) and partially overlapping cracks ($1 < \Delta x < 0$).

In the case of approaching cracks, we retrieve the non-monotonic behaviour shown in Fig.2.8. As expected, large lateral separations Δy result in weak interaction; θ_i starts small, with positive values lesser than 0.5° if the tip to tip separation distance $\sqrt{\Delta x^2 + \Delta y^2}$ is greater than $6L_f$, and increases to convey strengthening attraction as Δy diminishes. Surprisingly, attractive interaction

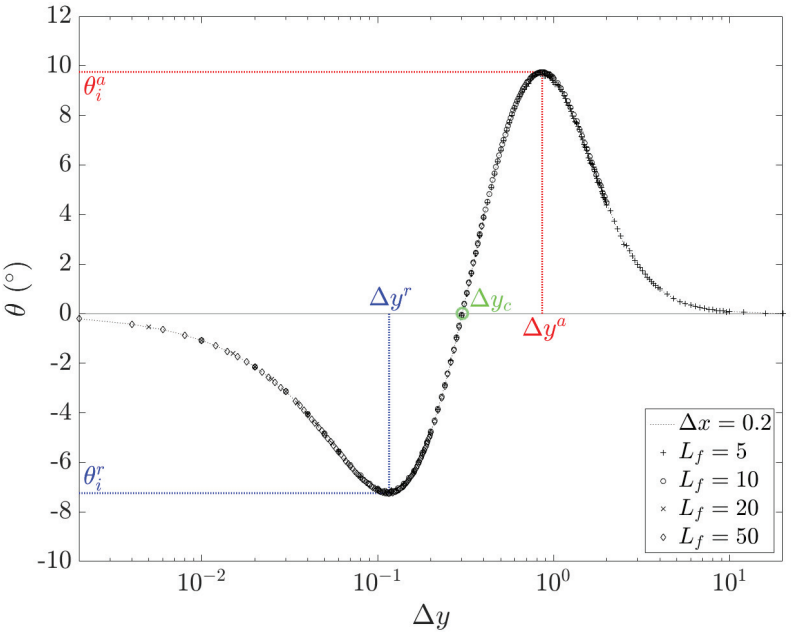

Figure 2.8 – **Typical $\theta_i(\Delta y)$ evolution for approaching cracks:** ($\Delta x > 0$) The point corresponding to $\Delta y = 0$ is not represented here because of the logarithmic scale. In this situation $\theta_i = 0$, no matter the value of Δx.

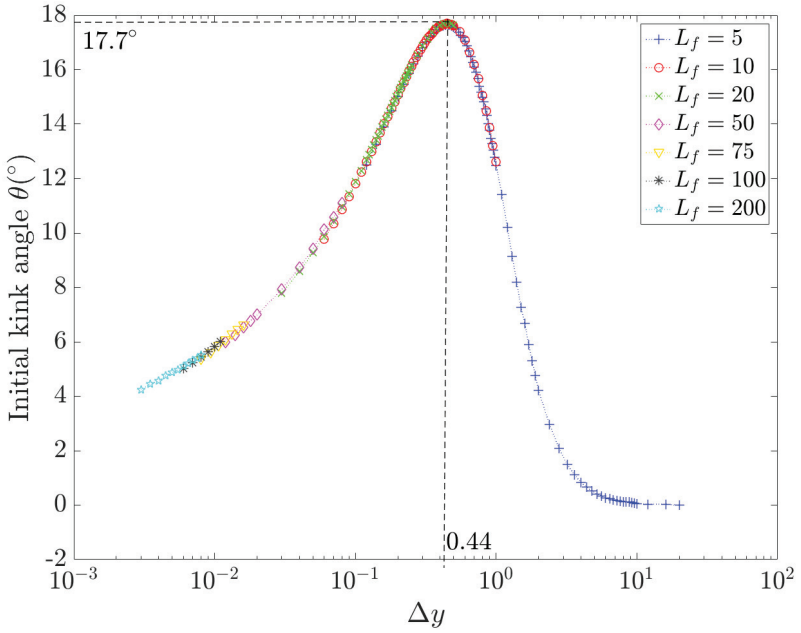

Figure 2.9 – **Typical $\theta_i(\Delta y)$ evolutions for coincident cracks:** ($\Delta x = 0$). Several crack length L_f were used to reach a 5 orders of magnitude span in Δy.

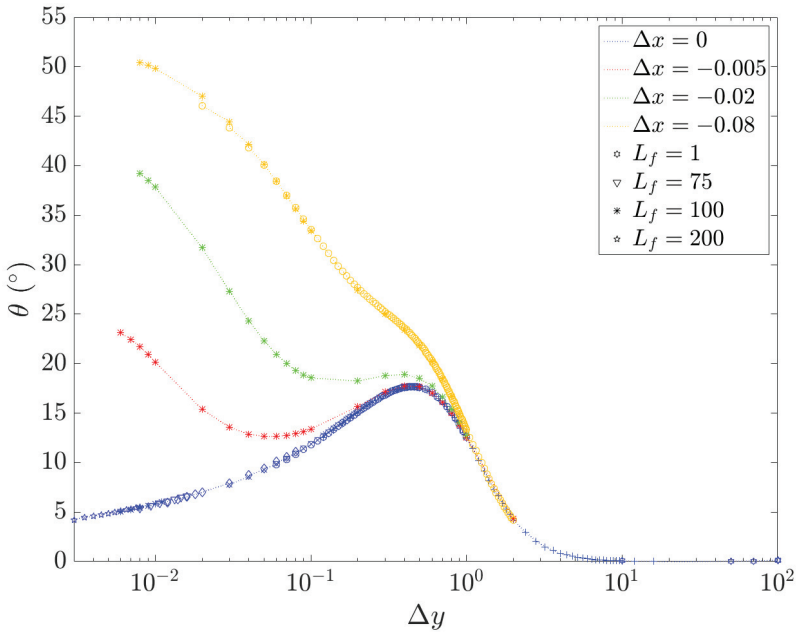

Figure 2.10 – **Typical $\theta_i(\Delta y)$ evolutions for partially overlapping cracks:** ($\Delta x < 0$). Contrary to the case of approaching cracks, the variations of the initial kink angle with the vertical separation is strongly dependent on the magnitude of horizontal spacing. While cracks only slightly overlapping retain an optimum of attraction, this local maximum slowly disappears as the superposition increases.

does not intensify indefinitely as the cracks get closer: θ_i reaches its maximum value $\theta_i^a(\Delta x)$ at $\Delta y^a(\Delta x)$. After this point, θ_i decreases acutely to the extent of crossing the abscissa axis at $\Delta y^c(\Delta x)$: the behaviour becomes then exclusively repulsive. The existence of an optimum of repulsion θ_i^r realized at Δy^r comes of as a second surprise: amazingly, the magnitude of the interaction only decreases after this point until it reaches zero for perfectly aligned cracks. As expected for these perfectly symmetric configurations, the PLS predicts that the cracks propagate straight ahead. However, and contrary to what was previously thought, this is not incompatible with LEFM predicting significant initial repulsion as a maximum repulsion angle is realized at a small lateral separation distance $\Delta y^r(\Delta x)$ amounting to only a small fraction of the initial crack length.

In the case of coincident cracks ($\Delta x = 0$) and partially overlapping cracks ($1 < \Delta x < 0$), the inner kink angle is positive for all values of Δy: the cracks always exhibit an attractive behaviour. In Fig.2.9, we plotted the evolution of θ_i when Δy tends toward zero or, alternatively, when L_f approaches infinity. While the repulsive zone disappears abruptly for $\Delta x = 0$, an optimum of attraction evolves continuously across $\Delta x = 0$: θ_i^a continues to exist for superimposed cracks not as a global maximum of attraction but as a local one. As shown in Fig. 2.10, when the level of superimposition increases, θ_i^a progressively vanishes until $\theta_i(\Delta y)$ becomes a purely decreasing function. It is possible to reach much larger kink angles in this situation: we recorded values up to about 55° for largely superimposed cracks.

2.2.2 Actual realization of the inner kink angle

It should be noted that we computed θ_i at the inner tips whether or not propagation actually occurs at these tips: the cracks can rather propagate the outer tips, depending on the $(\Delta x, \Delta y)$ configuration. We identified the advancing front independently from the determination of the SIF and θ_i by comparing the energy release rates, as computed directly by the FE simulation, at each tip. Assuming that only the inner *or* the outer tips can propagate, and not all four fronts at once, we found for each horizontal spacing Δx the value of vertical separation $\Delta y^{i/o}$ above which the the energy release rate becomes larger at the outer tip, indicating a propagation from this extremity. Here, the energy release rate was computed using the $G(\Theta)$ method, that is to say before crack propagation and assuming a straight path.

Gdoutos [99] led a similar investigation on a reduced Δx range, using the strain energy density criterion and tabulated values to determine K_I and K_{II} [103]. His results for the transition between propagation at the inner or outer tips are in excellent agreement with ours, as shown in Fig. 2.11d.

In the case of approaching cracks, propagation occurs at the inner tips for any $(\Delta x, \Delta y)$ combination that is under the $\Delta y^{i/o}(\Delta x)$ curve. Thus, we find that both attractive and repulsive behaviour can be effectively observed at the inner tips, and that only part of the attractive behaviour may be eclipsed by propagation occurring at the outer tips.

In the case of partially overlapping cracks, the inner kink angle θ_i is almost purely virtual: for close to all $(\Delta x, \Delta y)$ we tested propagation starts from the outer tips. As shown in Fig.2.11a, for any fixed negative value of $\Delta x \lesssim 0.2$, the energy release rate is considerably larger for the outer tips for small values of Δy. As the lateral separation increases, the energy release rates at each tips tend to the same asymptote, without swapping their relative position As shown in Fig.2.11b, only very small overlap, combined with a modest Δy allows a propagation from the inner tips.

In any case, EP-crack repulsion is not eclipsed by propagation from the outer tips; it is indeed possible to anticipate this behaviour using a LEFM model only.

2.2.3 Phase diagrams of crack interaction

The various configurations of EP-crack pairs are summarized in Fig.2.13 showing the value of θ in the $(\Delta x, \Delta y)$ space. The landscape formed by the θ values presents multi-scale characteristics. First, we find that the positions of the local extrema of attraction and repulsion, as well as the neutral line $\theta = 0$, are reasonably fitted as power laws of Δx (see also Table 2.1):

$$\Delta y_i = \Delta y_i^0 + A_i |\Delta x|^{\alpha_i} \tag{2.2}$$

The local optimum angles of interaction θ_a and θ_r form the crests and valleys of the landscape presented in Fig.2.13. As shown in Fig. 2.12, their values can be fitted as shifted power laws of

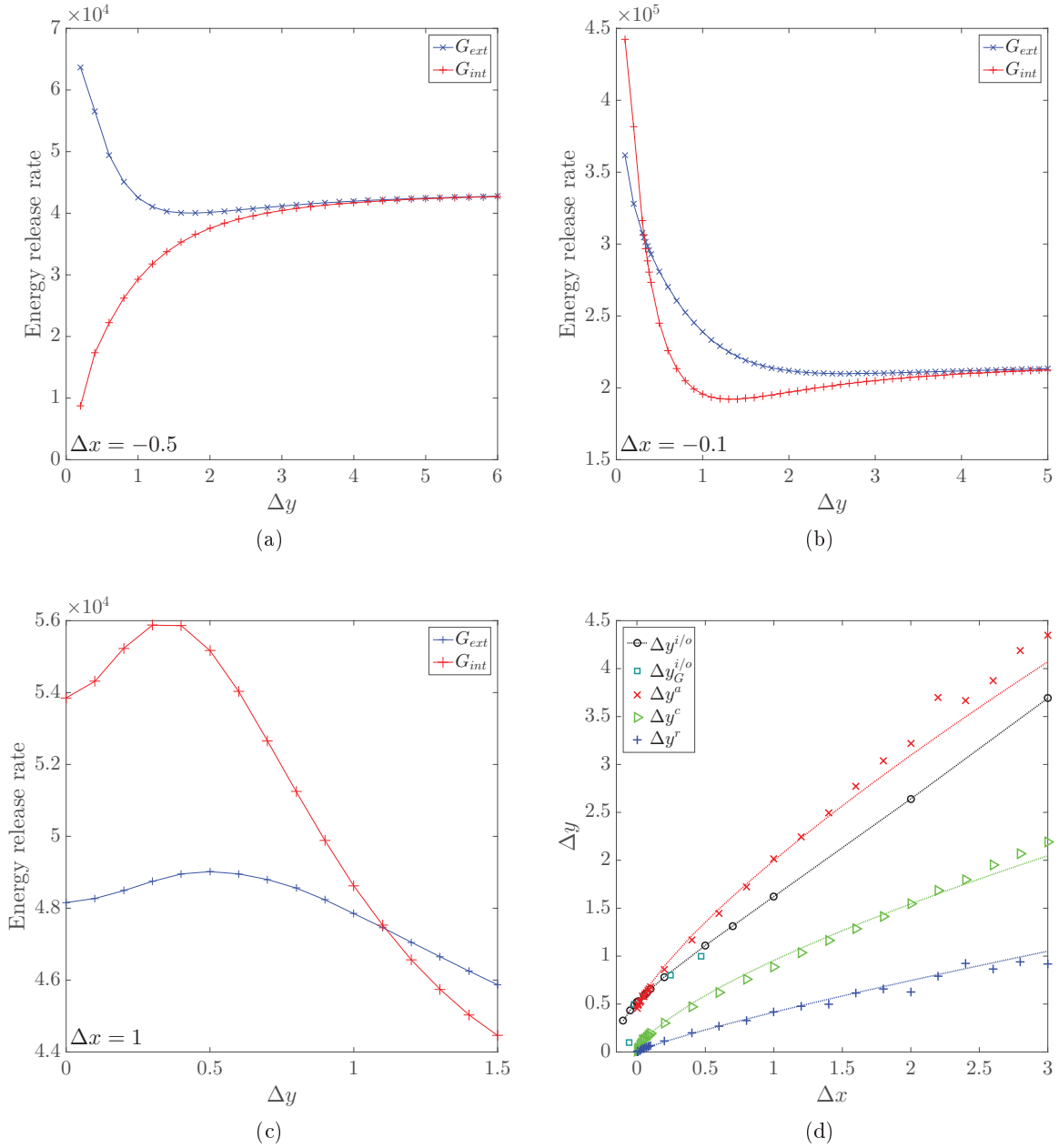

Figure 2.11 – **Identifying the advancing front:** Evolution of G_{int} the energy release rate at the inner tips and the corresponding G_{ext} at the outer tips, for fixed values of Δx.
(a) $\Delta x = -0.5$,
(b) $\Delta x = -0.1$,
(c) $\Delta x = 1$,
(d) Loci of remarkable points in the $(\Delta x, \Delta y)$ space as defined in Fig. 2.8. $\Delta y^{i/o}$ marks the limit above which EP-cracks will propagate from their outer tips rather than approaching each other. Even if we used the PLS instead of the SED criterion, our results are comparable to Gdoutos', $\Delta y_G^{i/o}$.

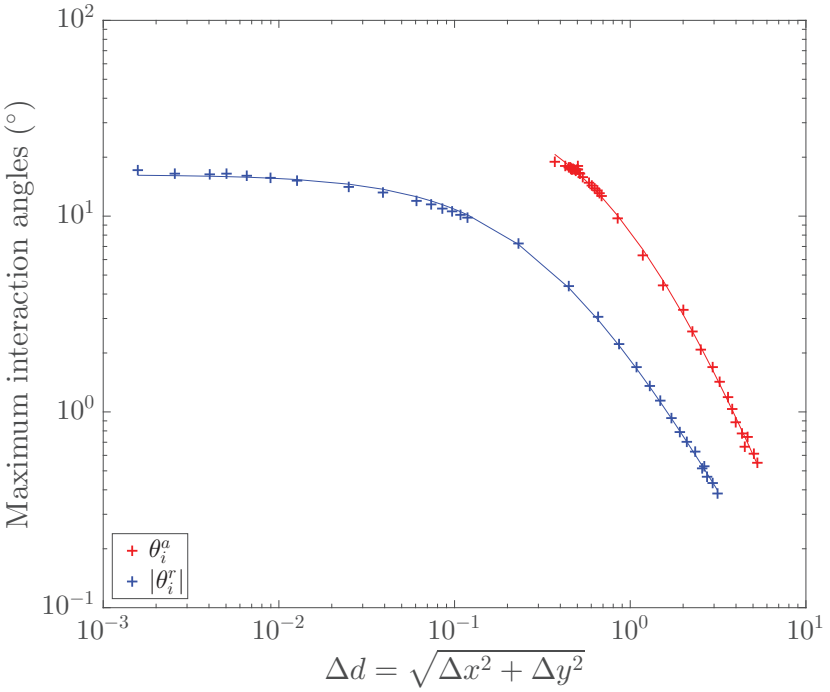

Figure 2.12 – **Maximum initial interaction angles of EP-crack pairs:** θ_i^a and θ_i^r follow a shifted power law (continuous line) of the distance $\Delta d = \sqrt{\Delta x^2 + \Delta y^2}$. Note that repulsion is recorded for much smaller tip to tip separation than attraction.

the tip to tip distance $\Delta d = \sqrt{\Delta x^2 + \Delta y^2}$):

$$\theta_{a/r} = \theta_{0a/r} \left(1 + \frac{\Delta d}{\lambda_{a/r}}\right)^{-\alpha_{a/r}} \tag{2.3}$$

Eq(2.2) and Eq(2.3) quantify how sensible interacting cracks are to the initial configuration and, in a larger sense, how difficult it may be to determine the path of interacting cracks. For $\Delta x > 0$, both attraction and repulsion tend to become stronger when the crack tips are closer. The length scale λ_r characterizing the increase in repulsion is however nearly three times smaller than the corresponding scale λ_a for the attractive zone (see table 2.1). Another remarkable scaling property is that attraction remains a dominant behaviour when the vertical offset between the cracks Δy is of the order of the crack length (as shown by $\Delta y_a^0 \neq 0$), while repulsion becomes prevailing for crack tip distances corresponding to very small fractions of the crack length, typically of the

Table 2.1 – Coefficients used in Eq(2.2) and (2.3) for the lines of maximum attraction or repulsion and the attraction/repulsion transition line. The non-zero Δy_a indicates that an optimum of attractive behaviour subsists well after superimposition of the inner tips and will always occur at distances comparable to the crack size.

	Δy_i^0	A_i	α_i
Δy_a	0.45	1.5	0.77
Δy_c	0	0.95	0.66
Δy_r	0	0.41	0.86

	θ_0	λ	α
θ_a	44.8	0.96	2.35
θ_r	−16.3	0.35	1.61

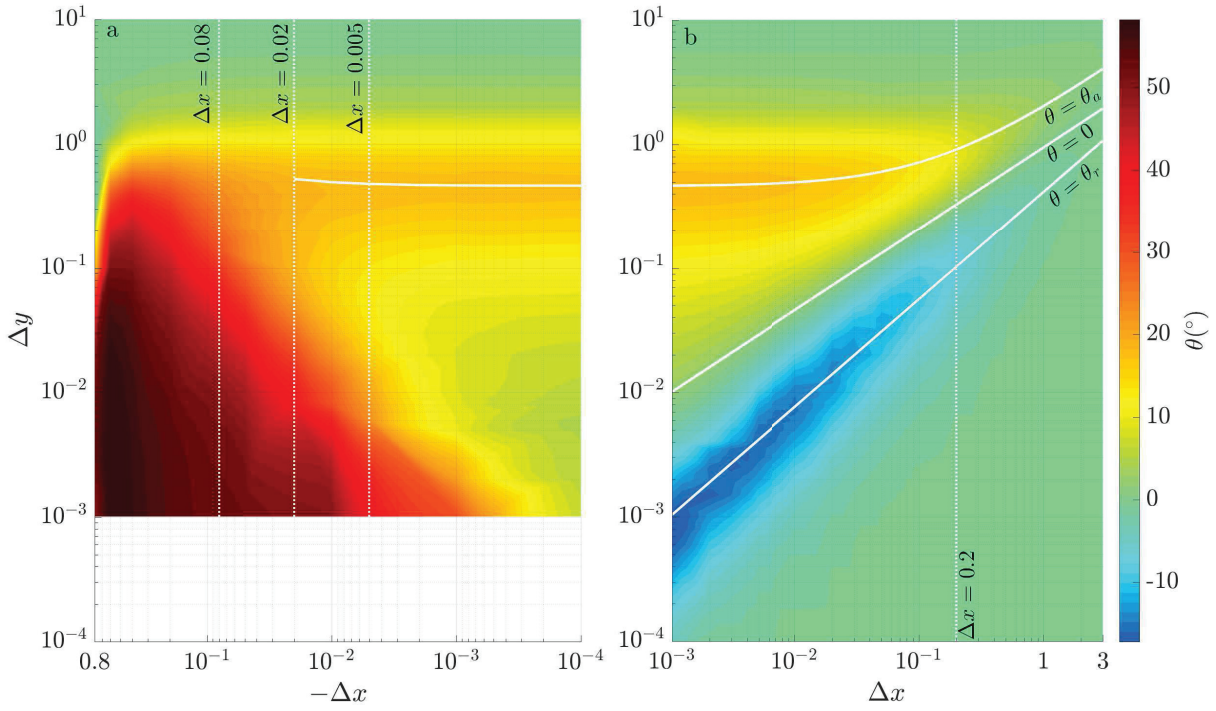

Figure 2.13 – **Initial kink angle for overlapping cracks (a) and approaching cracks (b) in the $(\Delta x, \Delta y)$ space.** The superimposed white lines signal the local maxima of attraction and repulsion, as well as the transition from attractive to repulsive (defined by $\theta_i = 0$). The dotted vertical lines show where the cuts for Fig. 2.8 & 2.10 were taken.

order of the percent (Fig.2.12).

An alternative representation of the θ_i values, as shown in Fig.2.13, can be proposed without making the distinction between approaching and overlapping cracks. In this case, θ_i is not dependent on its $(\Delta x, \Delta y)$ coordinates, but on the corresponding $(\Delta d, \alpha)$ values defined in Fig.2.14. Δd is simply the radial separation distance defined earlier and $\alpha = \text{atan}\left(\frac{\Delta y}{\Delta x}\right)$ the angle formed between the cracks axis and the line connecting their inner tips. With this representation, it becomes apparent on Fig. 2.15 that EP-cracks repulsion is a phenomenon confined to both α angles lower than 90° and small fractions of Δd.

2.2.4 Shearing EP-cracks

In practical situations, EP-cracks are seldom loaded under pure mode I; most notably, EP-cracks along rift zone are sheared into a combination of modes I and II. We display here the results for the initial kink angle for the configuration presented in Fig. 2.16. Contrary to the mode I configuration presented in section 2.1.1, we did not impose a stress but a displacement on the upper border of the medium. Because the lower side of the sample is clamped, this ensure a symmetric deformation along the medial axis and prevent rigid-body motion. The cracks are not exclusively sheared: we added a small opening component whose magnitude amount to one tenth of the shearing displacement, so that the cracks lips do not inter-penetrate, as our model do not factor contact.

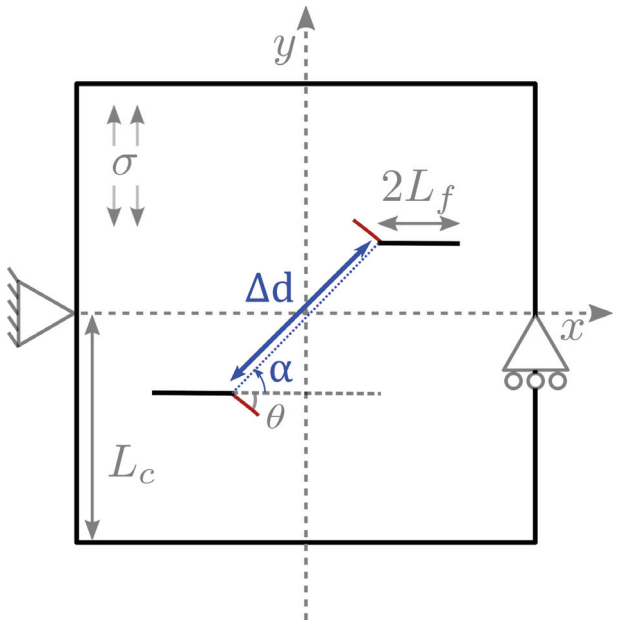

Figure 2.14 – **Initial kink angle of EP-crack pairs in the** $(\Delta d, \alpha)$ **space:** Definition of the polar system.

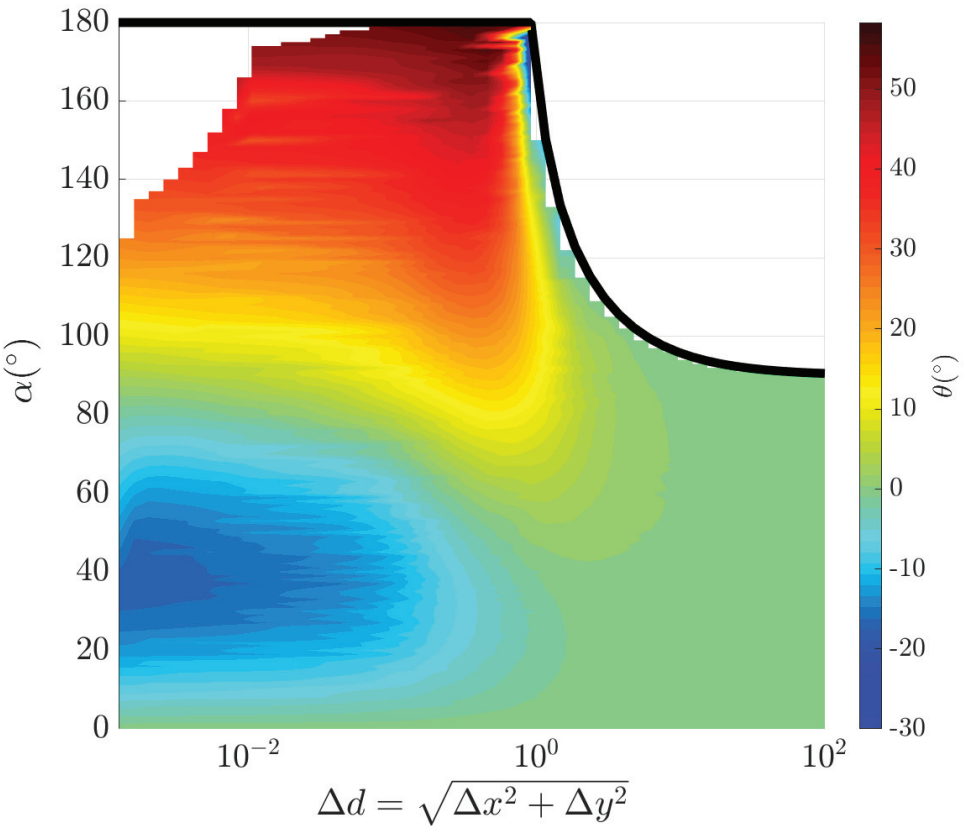

Figure 2.15 – **Initial kink angle of EP-crack pairs in the** $(\Delta d, \alpha)$ **space:** the black line marks the limit above which the upper crack pass the lower one on its left side. The rather extreme negative values taken by θ_i near this line in $\Delta d = 1$ region may correspond to repulsion induced by the *outer* tips, as the cracks are nearly completely stacked in this area.

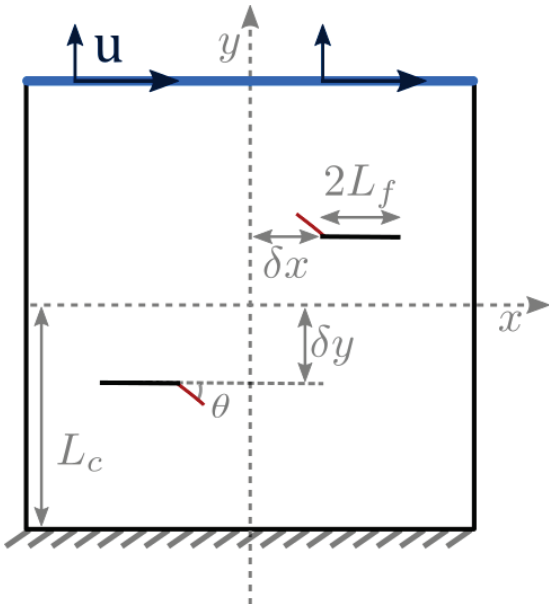

Figure 2.16 – **Shearing EP-cracks:** The boundary conditions of the EF model presented in Fig.2.1 were modified so that the far-field loading of the cracks was a mode II dominant mixed mode. The two possible directions of shearing were tested.

In these conditions, a single crack should kink into a direction of $\theta_i^0 \approx -64.1°$ according to the PLS. As shown in Fig. 2.17, we find a large zone where the interaction between the cracks can be classified as attractive: while the cracks are still going *away* from each other, θ_i is significantly less negative than $-64.1°$, in the sense that $\theta_i - \theta_i^0 > 0$. This attractive behaviour is largely dominant in the $(\Delta x, \Delta y)$ space we explored. A comparatively much smaller area containing weak repulsion angles, of a few degrees only, is centered around the $\Delta y = 1$ region.

Contrary to the precedent situation, it appears this time that repulsion, and not attraction evolves continuously across the $\Delta x = 0$ limit between the approaching and overlapping cases. On the other hand, the attractive behaviour seems to undergo a sharp transition at superposition that becomes more dramatic as lateral separation decreases. For example, θ_i is of the same order of magnitude across both sides of the $\Delta x = 0$ axis if $\Delta y \gtrsim 5.10^{-2}$ while it is almost twice greater on the overlapping side if $\Delta y \approx 10^{-3}$.

It should be noted that the $(\Delta x, \Delta y)$ space was charted with a much smaller number of data points than the purely tensile situation presented in section 2.1.1: all interpolations are less precise and it is possible that very narrow zones of intense attraction or repulsion escaped us. Precise fits such as those given in eq. (2.2) or (2.3) would necessitate to compute much more data points than we were able to.

2.2.5 Partial conclusion

The idea that repulsion between EP-crack pairs is the result of the formation of a plastic zone around the crack tips has been put forward recently [3]. At first glance it seems supported by experimental data: Fender *et al.*[1] did not observe repulsion in her set up, and Dalbe *et*

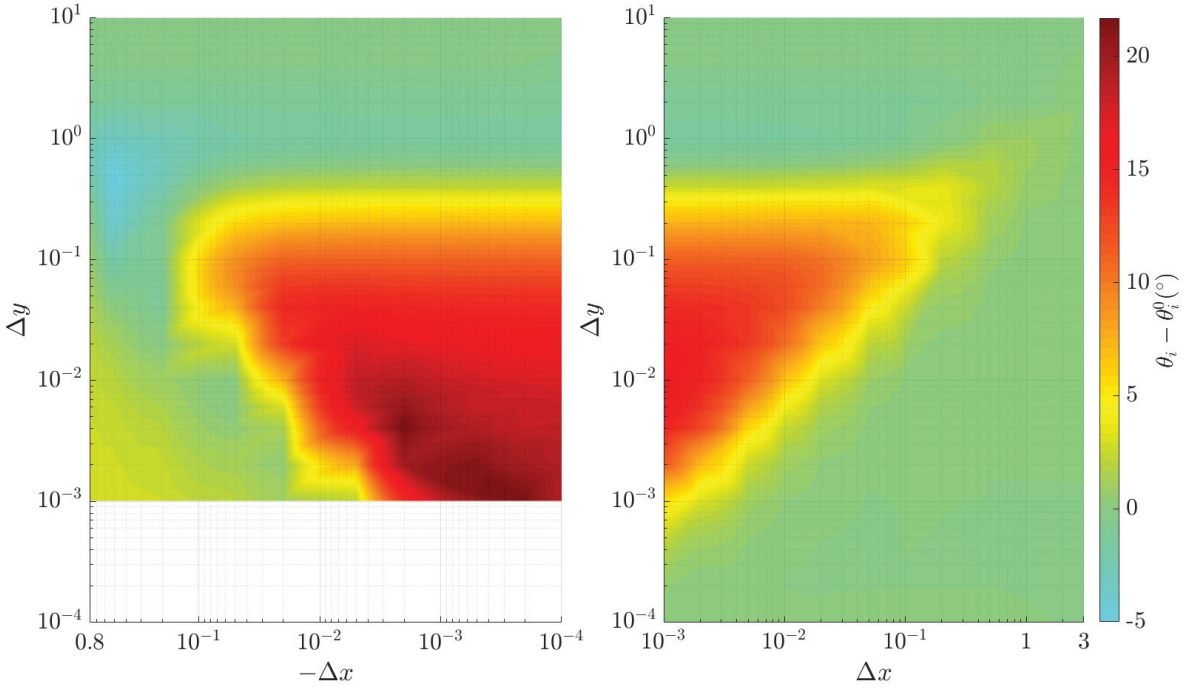

Figure 2.17 – **Initial kink angle for sheared EP-cracks:** for (a) overlapping cracks and (b) approaching cracks . In both case, the initial kink angle of a similarly loaded single crack, $\theta_i^0 = -64.1^\circ$ was deducted to represent the *interaction component* $\theta_i - \theta_i^0$ of the kink angle only. The irregularities in the attraction to repulsion transition are caused by the reduced number of data points we have in this configuration: less than 500, while over 7500 in the purely tensile configuration.

al. reported an apparent conflict between her results and the PLS predictions for the initial bifurcation angle of aligned EP-cracks.

However, as we have seen in section 1.3.3, this hypothesis is inconsistent with other observations, in particular those of large EP-cracks at the geological scale. The work presented in this chapter is a first step to reconcile theory and observation: the difficulty to predict crack repulsion in the context of LEFM does not come from a failure of the model or of the bifurcation criterion, but from the very narrow $(\Delta x, \Delta y)$ domain in which different behaviours, from repulsive to attractive, can initiate.

Our results show that significant deviation ($|\theta_i| > 10^\circ$), either attractive or repulsive, can arise for strictly positive horizontal spacing smaller than one fifth of the cracks length. The comparatively smaller size of the repulsive zone, compared to the dominant attractive domain, may explain why the repulsive component of EP-cracks path is most often visible in larger settings rather than laboratory experiments. Finally, the existence of an optimum of repulsion realised for small values of Δy may indicate that the inconsistence pointed out by Dalbe *et al.* [2] is only apparent: the strong sensitivity of the kink direction to small misalignments between the cracks could be enough to induce significant repulsion. While we did find that perfectly aligned ($\Delta y = 0$) do not interact at all and propagate straight ahead, θ_i grows steeply with a slight increase in

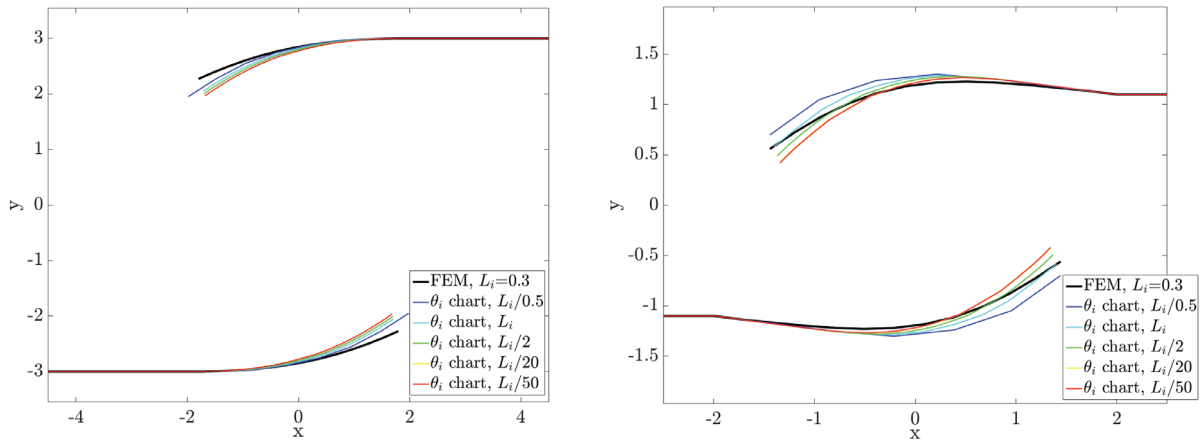

Figure 2.18 – **FEM-less trajectories:** Close-up of the inner tips.
(a) $L_f = 10$, $\Delta x = 0.2$, $\Delta y = 0.3$. (b) $L_f = 10$, $\Delta x = 0.2$, $\Delta y = 0.11$.

lateral spacing, favouring unstable crack paths. This is consistent with the theory presented by Melin [97], who concluded that the smallest perturbation in collinear EP-cracks will force them to deviate from their straight paths. Furthermore, this instability may also explain why experimental observation very rarely shows crack merging tip to tip.

2.3 Determining complete trajectories

2.3.1 Necessity of an actualised FEM-computation: influence of the path history

Because of the stress singularity at the crack tips, one can wonder if the stress field around EP-cracks is not mostly determined by the relative position of the tips. If this is the case the knowledge of $\theta_i(\Delta x, Deltay)$ should be sufficient to determine complete crack paths.

We compared the crack paths obtained using the FEM method described later in section 2.3.2 to trajectories based only on the $\theta_i(\Delta x, \Delta y)$ chart presented in Fig. 2.13. To compute them we simply determined the separations between the crack tip (normalized by the total length of the cracks, not the initial length), read θ_k on the chart and added a rectilinear segment of arbitrary length. This method presents the advantage of being extremely fast as long as an accurate θ_i chart of the correct loading is already available, and is equivalent to neglecting the propagation history. In other words, this methods make the gross assumption that the effect of the crack tips positions eclipses completely the effect of the previous path shape: for each step the local inclination angle is taken as $\theta_k \approx \theta_i$, as if the whole crack were straight.

This method gives results somewhat comparable to the full finite element simulation. However, small errors accumulate as the crack advances and we do not get the same propagation paths even when choosing the same increment length. As shown in Fig. 2.18, this method converges toward a stable path when L_i diminishes: we can therefore assume that most of the difference from the FEM-simulated trajectories is caused by the previous path assumption and not by

interpolation errors when calculating θ_k.

This method is not accurate enough to properly render EP-crack paths in details; in the following section we will present the more precise, and more compute-intensive, process we used to determine EP-crack paths.

2.3.2 Method: an iterating process

The procedure presented in section 2.1.1 allows to determine the next propagation direction of any advancing crack whose SIF are known. We propose to expand this method to determine approximate crack trajectories: after the FE computation step to calculate the SIF and the determination of the initial kink angle according to the PLS, it is possible to define a new finite element problem by adding a small segment of arbitrary length L_i at the tip of the initial cracks. We can then solve again for the SIF at the new crack tips and determine the next kink angle. Repeating the process as necessary allows to determine complete crack trajectories approximated by a succession of short rectilinear segments.

Because we only studied the symmetric fracture problem presented in section 2.3.4, the SIF at the tips of each EP-cracks are always identical and, in accordance with the LEFM principles, the propagation paths of each crack must remain symmetric. In practice, numerical imprecisions cause very slight differences between the SIF at the two crack tips, of the order of a 10^{-3} relative difference in the worst cases. They do not lead to much variation in the next kink angle θ_k but cumulatively such meager deviations could lead to incorrect crack paths. To prevent this phenomenon θ_k was not computed independently at each crack tip, but globally with SIF averaged over the two tips as input for eq. (1.40).

This symmetry also dispensed us to consider which crack tip would propagate first, as both crack fronts must advance at the same speed. Likewise, we were able to use the same boundary conditions across all pseudo-time steps thanks to the symmetric propagation: the imposed border displacement was constant no matter the length of the cracks. In more complex situations taking the energy release rate at each crack tip into account, and how it compares to the critical energy release rate of the material, would be needed to identify each crack front speed.

Although this process is largely similar to the computation scheme described in [108], we chose to approximate the crack extension by a short segment instead of a portion of a curve. As a result, we do not need to compute the T-stress necessary when using a curved increment, which can be arduous in the case of interacting cracks [106]. As shown in the following section, convergence regarding L_i is easily reached despite this approximation.

2.3.3 Validation against known experimental results

To test the validity of our method, we compared the simulated path of a single edge crack propagating in a PMMA beam pierced with three holes and subjected to a three points bending test (see Fig. 2.19) to the experimental and FEM results presented in [30]. This configuration

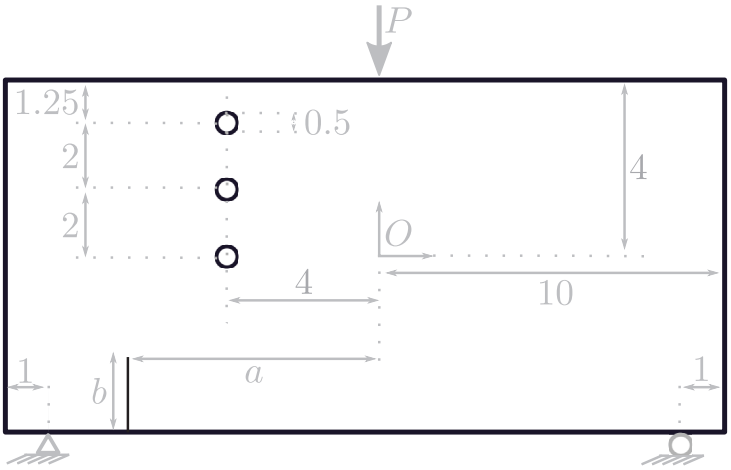

Figure 2.19 – **Simulated trajectories test case:** Initial geometry of the 3 points bending test case. As in [30], all dimensions are in inches. Two independent situations were tested in a first ($a = 5in, b = 1.5in$) and second ($a = 6in, b = 1.0in$) examples.

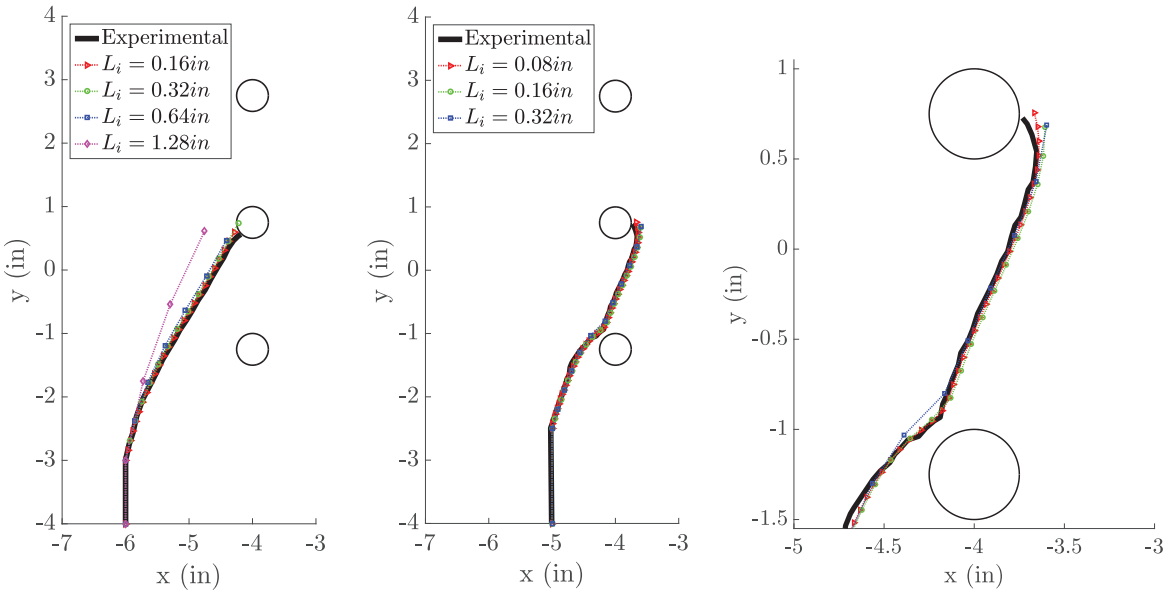

Figure 2.20 – **Comparison between experimental and simulated trajectories:** All experimental data was taken from [30]. (a) Example 1: the initial notch is defined by $a = 6in, b = 1.0in$. (b) Example 2: $a = 5in, b = 1.5in$. (c) Close-up from example 2.

exhibits a great sensitivity to the initial notch: any variations in its position and length will lead to completely different propagation paths. This series of experiment was used to validate simulated crack trajectories in brittle materials repeatedly [49, 50, 109]: it is well suited to confirm our simulations are in agreement with the LEFM theory.

We examined two different initial notch configurations (see Fig. 2.20) to test the robustness of our computational scheme regarding the increment length L_i. We chose to represent the problem as a $2D$ plane stress model; as seen before the value of the imposed force P or the elastic constants E and ν is of no effect on the final trajectory because of the quasi-static propagation assumption. The smallest mesh size around the crack tips is always $h = L_i/20$.

In both cases, we retrieved excellent agreement between simulated and observed trajectories given a sufficiently small L_i.

In the first example shown in Fig.2.20a, the smallest increment length $L_i = 0.16in$ will cause the crack to reach the second hole in 25 iterations. There is no need to refine the crack path further, as doubling or even quadrupling L_i yields nearly identical trajectories. It takes an increment length as large as $L_i = 1.28in$ for the simulation to deviate clearly from the observation: in this situation, the crack path is approximated by only 3 segments. The only exception to this very quick convergence regarding L_i is for the final increments very close to the second hole. In this region, the stress gradient is higher because of the proximity of a free edge: the curve of the crack is more pronounced and only the smallest increment length is able to capture it.

This effect is even more visible in the second example shown in Fig.2.20b & 2.20c, whose final propagation path is less regular. While taking $L_i = 0.16in$ gives again satisfying results, half this increment length depicts the sharp turn in the vicinity of the lowest hole better. Once more, the very end of the trajectory near the middle hole is not well captured by the simulations, regardless of the chosen increment length.

In conclusion, convergence regarding the increment length is quite easy to reach in most situations. However some small portions of the simulated crack paths may remain unusable where the cracks approach free edges. The same can be expected when cracks approach intersection. A complete convergence study focused specifically on the case of EP-crack pairs is presented in section 2.3.4.

2.3.4 Path discretization and other modelling characteristics of EP-crack pairs

We applied our method to the experimental configuration presented in [2], and we conserve their notations: a square plate of half side length L_C is notched with two collinear cracks separated horizontally by a distance L and vertically by a distance d (See Fig. 2.21). In the experiment, the sides of the plate are slowly pulled apart so that the cracks propagate quasi-statically. The clamping jaw is clad with rubber, and allows some transverse displacement. We represented this boundary condition by clamping the mid-point of the bottom side, and allowing only horizontal displacement for every other points of this side. On the upper side of the plate, we impose a

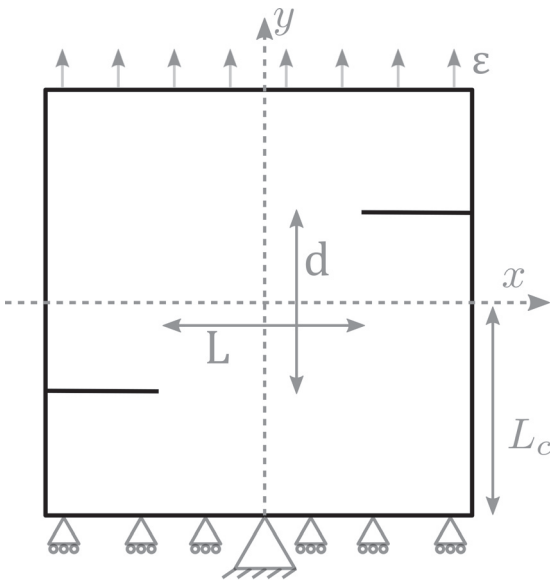

Figure 2.21 – **EP-cracks definition:** Schematic representation of the FEM model used to simulate Dalbe's experiments [2]. We keep using the same notations: the two initial crack tips are separated by L and d, the horizontal and vertical distances respectively.

displacement Δu only on the pulling direction: transverse displacement is let free. Likewise, the horizontal displacement of the bottom side is free.

We used the PET Young's modulus and Poisson ratio ($E = 1.8GPa$ and $\nu = 0.38$) as inputs of the FEM simulations, but tests with other values confirmed these parameters do no influence the shape of the final trajectory in a LEFM model. Likewise, the magnitude of the imposed displacement is of little impact on the crack path. We used the same value $\Delta u = 2L_c/100$ across all simulations and incrementation steps.

In all simulation results presented in section 2.4, we used the same smallest mesh size around the crack tips $h = L_i/20$ that was employed to validate our methodology in section 2.3.3. Because of the relatively small size of the plate compared to the crack length, we chose to re-mesh the whole specimen for each added crack increment. In situations where the cracks are several order of magnitude smaller than the medium they are propagating into, local re-meshing around the crack tips exclusively could save significant computation time.

Contrary to other parameters such as material properties or the magnitude of the imposed deformation, we have seen in section 2.3.3 that the choice of the increment length L_i can be critical when a crack tip approaches a zone with a high stress gradient. In the case of EP-crack pairs approaching one another, the precision of the simulation may deteriorate when a crack nears a free edge, whether it is a plate edge or the other crack. After tests to find the optimum L_i for the geometry presented in Fig. 2.21, our results are in agreement with this observation. In most cases, the size of the propagation increment has very little impact on the final crack path: with the exception of d close to 1.84 cm the paths superimpose perfectly whether $L_i = 0.02$ cm, 0.04 cm or 0.08 cm. The case of $d = 1.84$ cm is singular: as we will see in section 2.4.1, the simulated trajectories belong to one of two kinds and the cracks behaviour transition from hook shaped to s-shaped for a vertical separation of $d = 1.84$ cm. Indeed, for smaller values of d the

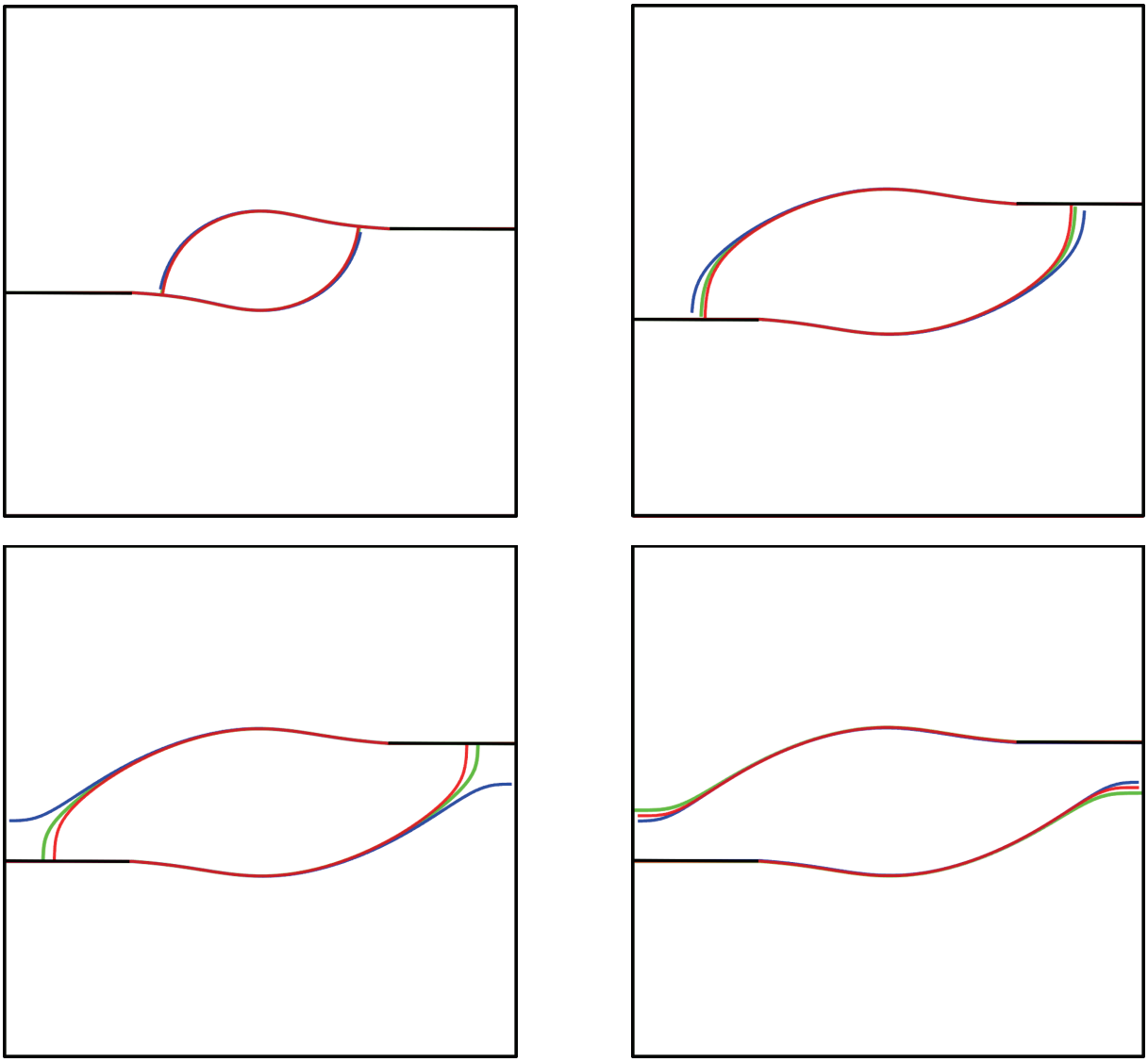

Figure 2.22 – **Simulated trajectories with varying increment length:** red: $L_i = 0.02$ cm, green: $L_i = 0.04$ cm, blue: $L_i = 0.08$ cm
(a) The cracks are originally separated by $L = 4$ cm and $d = 1.0$ cm. The medium increment trajectory is barely discernible under the finer one: this example is representative of most (L, d) combinations for which an increment length of $L_i = 0.04$ cm is sufficient to get completely converged paths.
(b) $L = 4$ cm and $d = 1.8$ cm.
(c) $L = 4$ cm and $d = 1.84$ cm
(d) $L = 4$ cm and $d = 1.86$ cm
As the initial vertical separation increases, the cracks reach regions more strongly influenced by the boundaries of the medium and the second cracks: convergence is harder to reach in these areas. While the impact of L_i can be considerable in the later stages of propagation, this effect is apparent only for a minority of initials (L, d) combinations, and never until well after the cracks overlap.

cracks are hook shaped: the closer d is to its critical value, the closer the cracks will join one another near the plate edge. In this situation a slightly longer increment can be enough to bring the crack tip nearer from the side of the specimen and completely transform the cracks behaviour. For values of d close but not exactly equal to 1.84 cm, the influence of L_i is not as dramatic but some notable differences are still observable in the later stages of the propagation (see Fig. 2.22).

Whatever the increment length chosen, we did not observe significant variation in the repulsive component of the crack trajectories, or in any portion of the path preceding the crack tips superimposition. We are therefore confident that our choice of $L_i = 0.04$ cm in all computations is adequate to study the repulsive phase in this configuration. In section 2.4, all results shall be assumed to have been computed with this increment length, unless otherwise specified.

2.4 Reproducing experimental trajectories

In this section, we are comparing trajectories of EP-crack pairs predicted by the LEFM+PLS framework to the experimental results obtained by Dalbe *et al.* [2]. As we have seen in section 1.3.1, we expect the cracks to exhibit a repulsive behaviour that increases in magnitude when the transverse separation d diminishes, and the repulsion to attraction transition to occur before overlapping.

2.4.1 Typical trajectories

Given a fixed value of $L = 4$ cm we retrieve again a repulsion to attraction transition with increasing values of d. When the vertical separation is smaller that $d \approx 3.5$ cm, the initial behaviour of the cracks is repulsive and remain so until the tips overlap. For greater values of d, only weak attractive behaviour is retrieved all along the propagation.

In the experiments we tried to reproduced numerically, the propagation was stopped shortly after the crack overlapped to prevent the appearance of too much out of plane deformation. Without this constraint, we were able to simulate much longer trajectories and to unveil two different behaviours. Indeed, the simulated cracks do not necessarily intersect with each other; if the initial separation d between the cracks is sufficient ($d \gtrsim 1.84$ cm), the crack will deviate *again* at the end of the attractive phase to recover parallel trajectories and finally reach the specimen border. These s-shaped path were also retrieved by Gdoutos [99] or Mills and Walker [98] ; the latter dismissed them as numerical artefacts because they did not have real examples of s-shaped EP-cracks. In our opinion, these paths are concordant with LEFM theory: their scarcity in observations can be explained by physical arguments. In particular, we have seen in section 2.2.2 that EP-cracks completely included in the material (ie. not surface breaking) can propagate preferentially from their outer tips. It is possible that inner tips propagation is arrested before the emergence of a complete s-shape.

In the singular case of perfectly collinear cracks ($d = 0$), the cracks propagate straight ahead without deflecting on either side. As noted in section 2.2.1, this result is not incompatible with

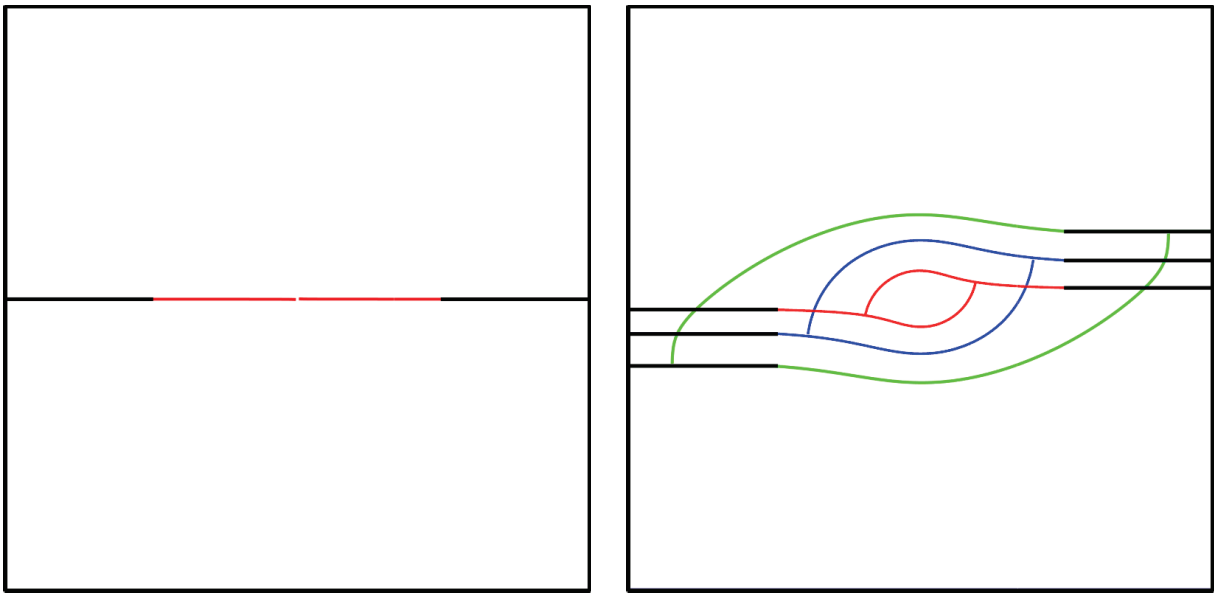

(a)

(b)

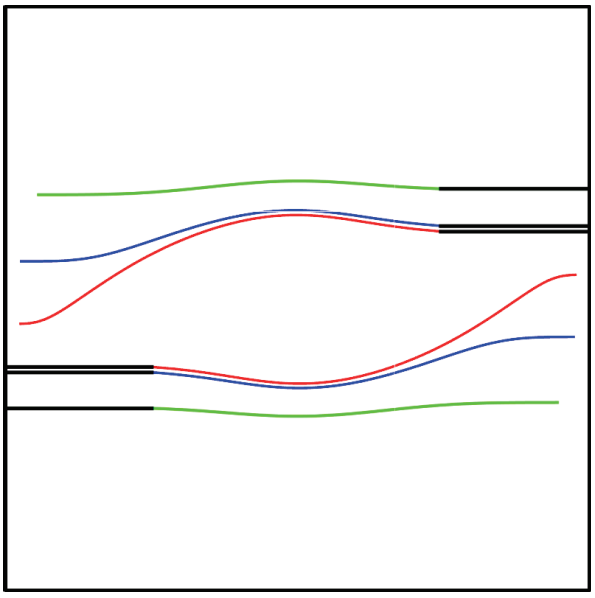

(c)

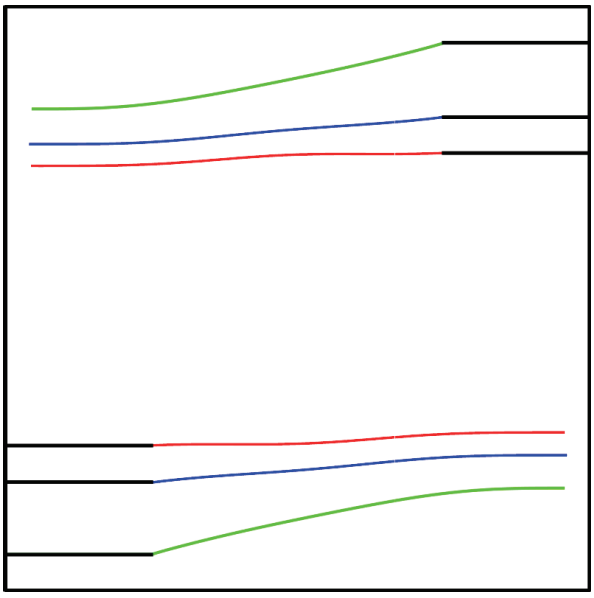

(d)

Figure 2.23 – **Typical EP-cracks shapes:** $L = 4$ cm in all examples presented here.
(a) Perfectly aligned cracks with $d = 0$ do not interact and propagate into a straight line.
(b) In this configuration, the well-documented hook-shaped path is retrieved for $d \leqslant 1.84$ cm. Red: $d = 0.3$ cm, blue: $d = 1$ cm, green $d = 1.84$ cm.
(c) Intermediate values of lateral separation yield an s-shaped path. Red: $d = 1.85$ cm, blue: $d = 2$ cm, green $d = 3$ cm
(d) For even larger d, the only interaction between the cracks is moderately attractive. Red: $d = 4$ cm, blue: $d = 5$ cm, green $d = 7$ cm.

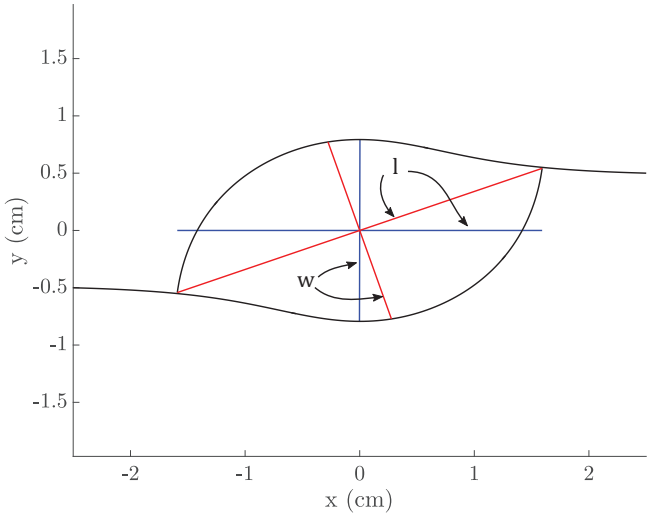

Figure 2.24 – **Aspect ratio definition:** $A = l/w$. Here $L = 5$ cm and $d = 1$ cm.

the empirical observation that initially aligned cracks do not merge tip to tip [64, 97]. Indeed, the slightest material defect would lead to the misalignment of the cracks' tips, and the apparition of a hook shaped path.

The so-called "universal" shape of EP-crack pairs, a hook-shaped path which does not exhibit a repulsive phase described in [1], was retrieved in our computation only when $L \leqslant 0$ cm, forcing the propagation to start when the potentially repulsive area is already passed. Indeed, in all (L, d) configurations we tested, repulsion was never observed after the tips passed each other.

2.4.2 Typical features of hook-shaped EP-crack pairs

Aspect ratio

In the literature, two different techniques were used to measure the aspect ratio A of the released central piece enclosed between two hook-shaped cracks. As shown in Fig.2.24, the length and width of the ovoid shape can be measured either in parallel to the cracks original axes, or in the direction of the line passing through both intersection points. While most authors do not acknowledge the difference, we found that it is of little importance, as the discrepancy between the two values is usually minimal.

Some authors postulated that the knowledge of the aspect ratio could be used to infer the loading conditions of EP-cracks retrospectively, and that it should always equate $A = 2$ in purely tensile situations [1, 68]. We find that the impact of boundary conditions is of more importance than anticipated, and results in largely dispersed values of A. As shown in Fig.2.25a for a fixed value of L, while A is indeed relatively constant over a large span of d, it grows steeply after $d \gtrsim 1.5$ cm. For these larger lateral separations, the overlap before intersection is longer: the cracks reach regions closer to the sample borders and are therefore much more affected by boundary conditions. Moreover the impact of L is significant: for example, if d is fixed to $d = 1.8$ cm, we find $A \approx 2.36$

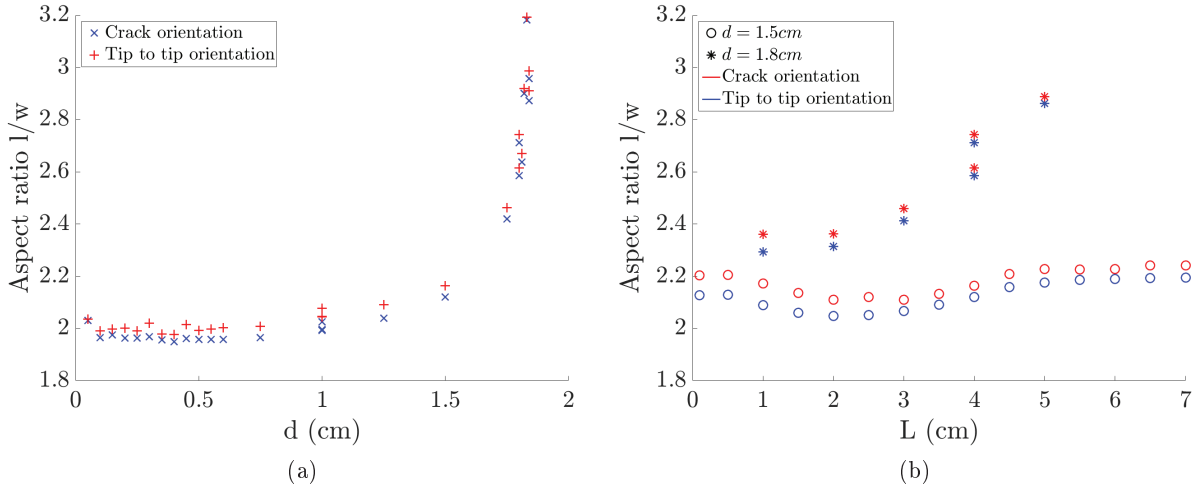

Figure 2.25 – **Evolution of A with the initial EP geometry:** (a) vs. d. (b) vs L. In both cases, the values are not too dispersed around $A \approx 2$, unless the central piece dimensions becomes significant compared to the total medium size.

if $L = 2$ cm and $A \approx 2.89$ when $L = 5$ cm, a $22,5\%$ relative difference. Situations where loadings are inaccessible but the initial conditions are known precisely seem unlikely, and it is therefore far-stretched to use a sole measure of A to evaluate unknown stresses, as it was proposed in [68].

We should note however in Fig. 2.25a the existence of a plateau for $d \lesssim 1.5$ cm: for these specific configurations we retrieve an aspect ratio of $A \approx 2$, close to the "universal value" observed by Fender *et al.* [1]. We infer that in these calculations as well as in Fender's experiments, the relative initial closeness of the cracks tips have a dominant effect on the propagation paths, over loadings and other boundary conditions.

Intersection angle

For hook-shaped paths, it is also possible to determine the intersection angle ϕ between the two cracks. The paths are expected to meet orthogonally: intersection angles retrieved experimentally usually lay between 80° and 90° [66, 84]. We determined ϕ by simply adding the tilt angle of the ending increment of one crack with the tilt angle of the intersected increment on the opposite crack. As shown in Fig.2.26, our results are in excellent agreement with observation, as we find that ϕ is an increasing function of d, starting at 80° and tending to 90°.

Just as for the aspect ratio, varying the value of the horizontal separation L will add dispersion to the results, but both the $[80°, 90°]$ interval and the trend to get closer to orthogonality as the lateral separation increases are always respected.

The few outlandish values visible in Fig.2.26 are explained by the use of a larger increment length. This may also suggest that relatively lower intersection angles for small offsets between the cracks ($d \lesssim 1$ cm) are artificial and caused a too large L_i comparatively to d, as closer-standing cracks have a smaller curvature radius.

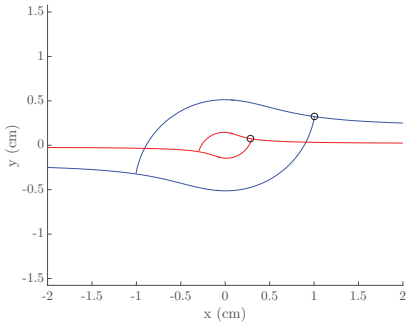

(a)

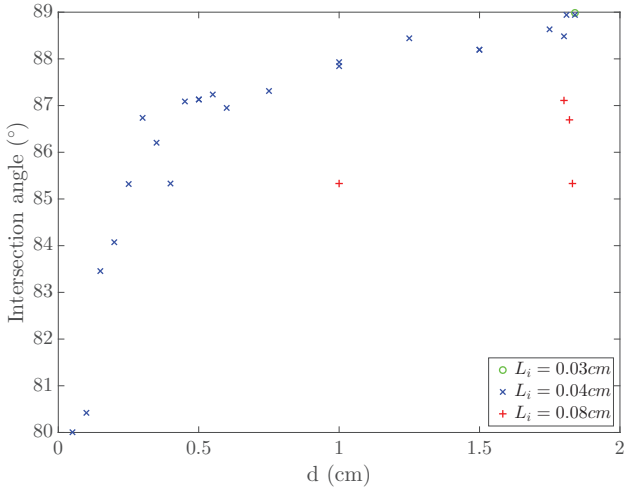

(b)

Figure 2.26 – **Intersection angle ϕ vs. d:** Here L is fixed to $L = 4$ cm.
(a) ϕ is identified as the sum of the tilt angle of the two closest increments. Red: $d = 0.05$ cm, blue: $d = 0.5$ cm.
(b) In agreement with observation, the cracks always join almost orthogonally. The influence of d on ϕ may well be a computational artefact.

Repulsive to attractive transition & maximum repulsion

For crack paths presenting a repulsive component, that is to say $d \lesssim 2.5$ cm whether the cracks intersect or are s-shaped, θ_k takes its last negative value (indicating repulsion) when the cracks' tips are overlapping by an horizontal distance comprised between 0.06 cmand 0.16 cm.

These quantities must be interpreted in light of the increment's length: our computations indicate that the turning point is usually removed from the plate center by a distance smaller than one (56% of all cases tested) or two L_i (29% of all cases tested). The remaining cases correspond to situations with a very small L, that is to say the propagation started nearly at coincidence, the repulsive to attractive transition occurs then for an overlap smaller than 0.24 cm. These results are consistent with the common experimental observation that EP-cracks become attractive upon overlap [1, 79, 82]. They are however conflicting with the specific experiment we are trying to reproduce numerically: Dalbe *et al.* [2] were one of the few studies that reported the repulsion to attraction transition taking place before overlapping. This, in our opinion, confirm that there a non-LEFM material effect at play in these experiments.

For a fixed $L = 7$ cm value, the initial horizontal separation between the cracks is large enough that the repulsive phase has space to unfold and is not artificially truncated, as is shown in Fig. 2.27b for various initial transverse separation distances d. Under these conditions, it is possible to determine the maximum of repulsion θ_{rm} as the tilt angle of the most inclined increment, as well as to identify the beginning of crack interaction. Indeed, for large L values, the cracks will start to propagate in an almost perfectly straight fashion, with very weak local repulsion angle. We define arbitrarily the beginning of the repulsive phase as the point whose abscissa corresponds to the intersection between the crack original axis and the tangent to the maximum of repulsion

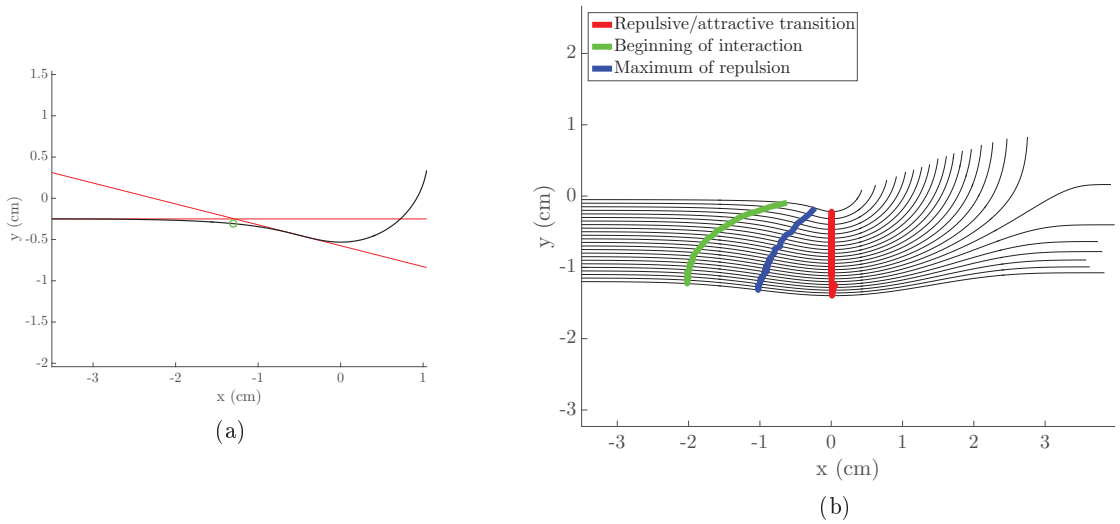

Figure 2.27 – **Remarkable points along propagation paths:**
(a) The beginning of interaction was identified as the point whose abscissa corresponds to intersection between the crack original axis and the tangent to the maximum of repulsion. Here $d = 0.5$ cm.
(b) While the turning point is aligned on the plate medial axis, both the maximum of repulsion and the beginning of interaction positions depends on d. For legibility reasons, only the left crack was represented, for $d = 0.1$ cm to $d = 2.4$ cm.

(See Fig. 2.27a). Contrary to the repulsion to attraction transition, whose position is constant in regards to lateral tip to tip separation, the position of the maximum of repulsion evolves nearly linearly with d. While the beginning of interaction evolves in a similar fashion for small values of d, it quickly saturates and tends toward a horizontal separation of 2.4 cm.

2.4.3 Sensitivity to initial conditions

The results presented in this chapter were all obtained for a geometry mimicking the one used in [2]: since the cracks length is of the same order than the medium size, the effect of initial conditions (initial geometry and loadings) is bound to be significant. In particular, our results may not be representative of the general case and it could explain the discrepancies with previous work [1], who used 10 cm $*$ 20 cm samples instead of square ones.

For example, choosing a rectangular medium, without modifying other geometric parameters such as L or the loading conditions, will impact the value of d for which the hook to s transition occurs. We redid the same computations in rectangular plates (one direction is 5%, 15% or 25% longer than the other). In the square case, the change of behaviour happens for $d = 1.84$ cm. In the case of a plate longer in the Ox direction shown in Fig. 2.28a, the change happens for greater values of $d = 1.98$; 2.25 or 2.55 cm respectively.

Inversely, the switch happens for smaller values of d, $d = 1.80$; 1.74 or 1.71 cm, if the plate is greater in the Oy direction (see Fig. 2.28b). In this case, the position of the repulsion to attraction transition is also shifted after overlap. This confirms that the variations observed with

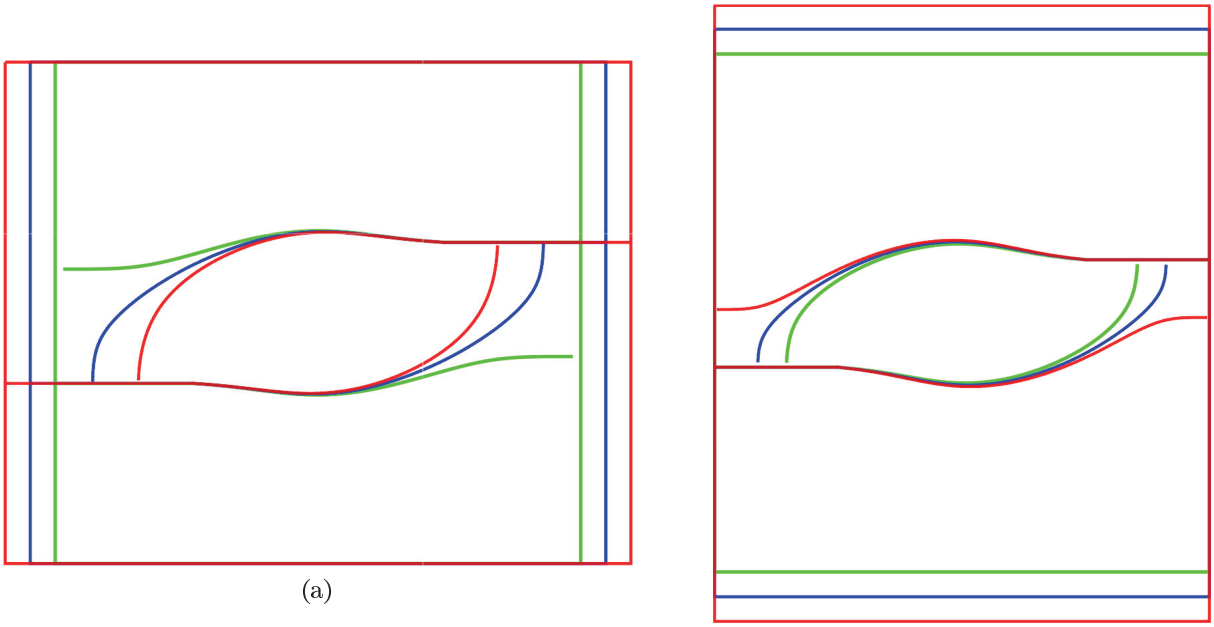

(a) (b)

Figure 2.28 – **Effect of a rectangular plate:** In all cases $L = 4$ cm. The plate length in one direction was increased by either 5% (green), 15% (blue), or 25% (red).
(a) Horizontally stretched plate: $d = 2.25$ cm. (b) Vertically stretched plate: $d = 1.74$ cm.

the horizontally stretched plates are not purely caused by variations in the cracks lengths.

We also computed a few trajectories of EP-cracks standing in a significantly larger medium, using the geometry presented in Fig.2.1. This fracture problem is completely different from the precedent, as there is potentially four propagating fronts instead of two. We focused on the inner tips propagation only and stopped the simulation when the energy release rate at the outer tips exceeded the one at the inner tips. As shown in Fig.2.29, while we retrieve again the classic hook shape (with or without repulsion), the well-known features often described in the literature are altered. Chiefly, the repulsive to attractive transition can occur *before* the inner tips overlap. This may be explainable by the choice of $(\Delta x, \Delta y) = (2.10^{-2}, 2.10^{-2})$ initially. These values are sensibly smaller than what was previously tested in controlled experiment; for large-scale natural observation, it is not inconceivable to retrieve this feature more often simply because because longer cracks make small $(\Delta x, \Delta y)$ separations more accessible.

These results showcase how highly sensible the final paths are to boundary conditions. In particular, making quantitatively accurate predictions of the cracks trajectories, instead of just determining qualitatively approximate shapes, probably requires the use of experimentally measured displacement fields, using for example Digital Image Correlation (DIC), directly as inputs of the simulations. They also illustrate that the discrepancy between Dalbe *et al.* [2] observation and the "universal" shape described in [1] may be, at least partially, explained by different initial configuration and not exclusively by complex material effects.

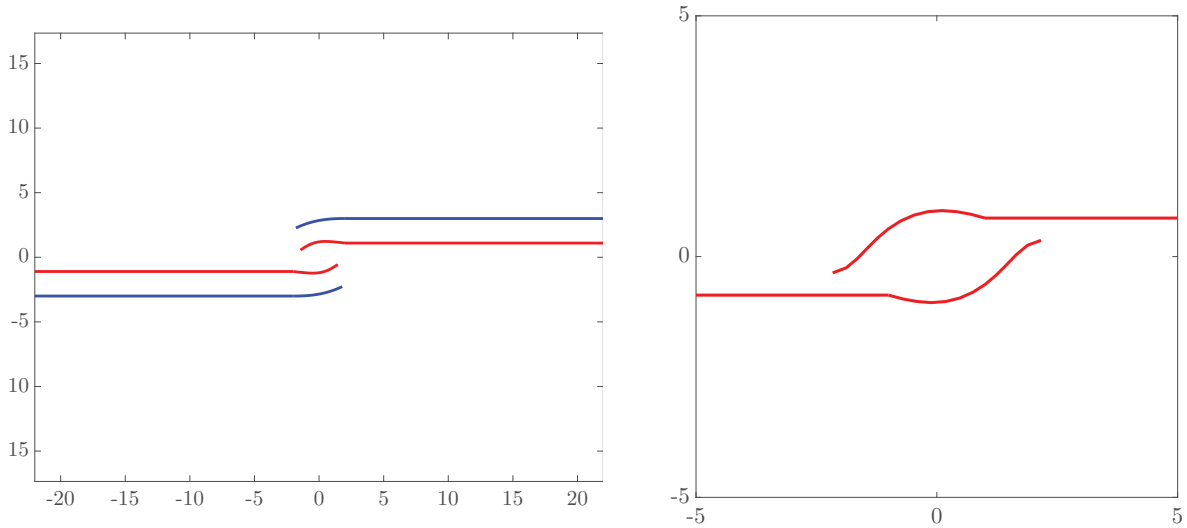

(a) (b)

Figure 2.29 – **EP-cracks propagating in a large medium:** Close-up on the inner tips. (a) Here $L_c = 1000$ and $L_f = 10$, blue: $\Delta x = 0.2$ and $\Delta y = 0.3$. Red: $\Delta x = 0.2$ and $\Delta y = 0.11$ (b) $L_c = 1000$, $Lf = 100$, $\Delta x = 0.01$ and $\Delta y = 0.08$.

2.4.4 SIF along the trajectories

As expected, when examining how the SIF evolves along the propagation, it becomes apparent that the cracks trajectories are controlled first and foremost by K_{II}. In Fig. 2.30 we represented for the three typical kinds of crack trajectory the evolution of K_I, K_{II} and θ_k, the local interaction angle, versus s, the curvilinear abscissa along the path. With the exception of the very first computational step, K_{II} is several order of magnitude smaller than K_I because the previous increment was determined as to minimize K^*_{II}, in accordance with the principle of local symmetry. K_{II} is no rigorously equal to 0 because the two cracks propagate at the same time: K^*_{II} is determined without anticipating the effect of the second crack propagating. Despite this, the maximum of repulsion corresponds to K_{II} changing sign. Similarly the turning point of the trajectory, which is marking the separation between the repulsive and attractive phases, is triggered by a local minimum of K_{II}. Both changes in behaviour are easily explained by the first order of eq. (1.41) to (1.44). Taking θ_k as the local interaction angle, that is to say the angle formed between the last path increment and the horizontal at computational step k, we have α_k the local kink angle (formed between the local crack direction and the next propagation direction) derived from eq. (1.27), then we have naturally:

$$\theta_k = \theta_{k-1} + \alpha_k = \sum_{p=1}^{k} \alpha_p \tag{2.4}$$

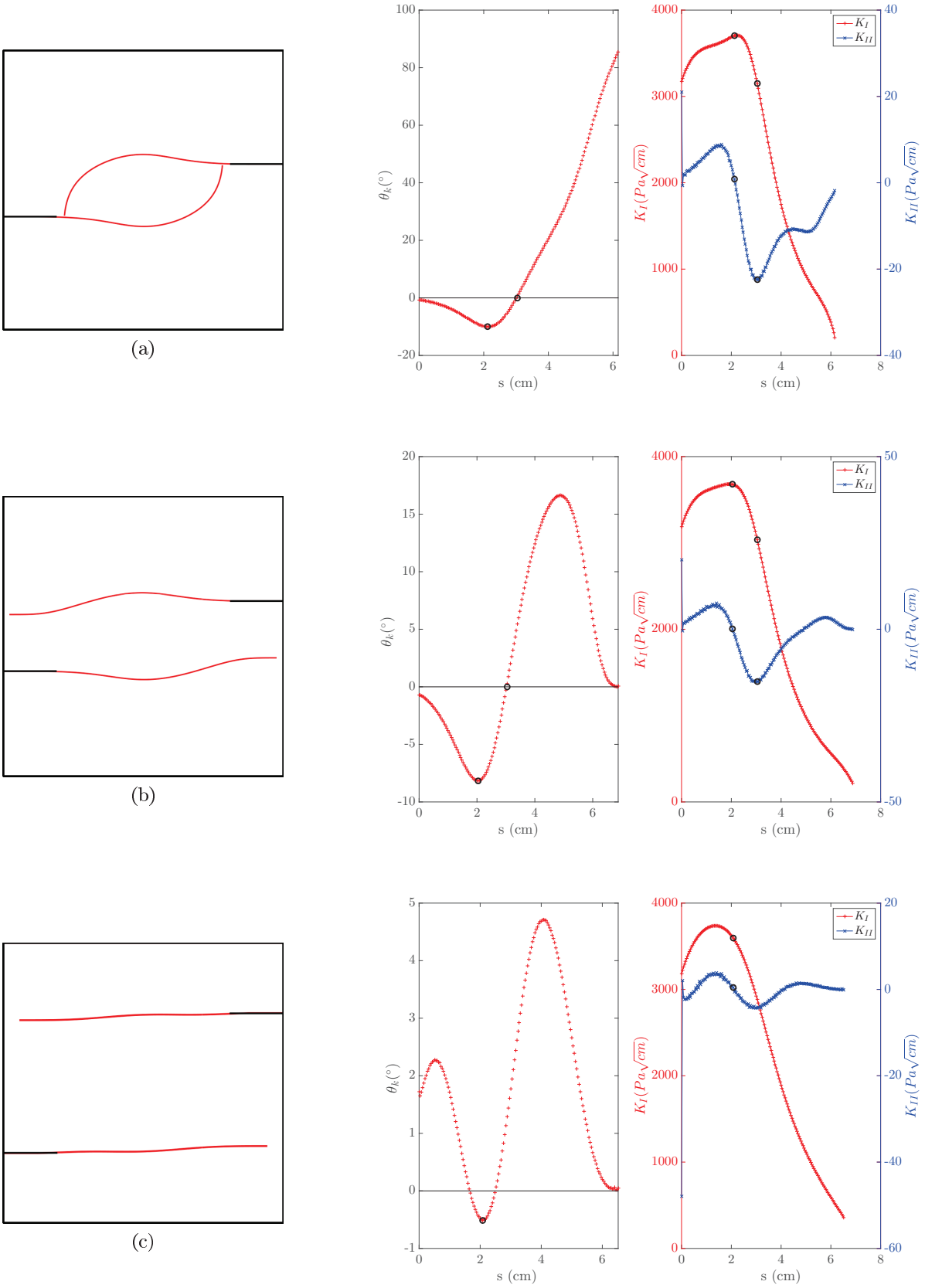

Figure 2.30 – **SIF and θ_k evolution along the propagation:** $L = 6$ cm in all three examples. (a) $d = 1.5$ cm, (b) $d = 2$ cm, (c) $d = 4$ cm. Remarkable points, maximum of repulsion and repulsive/attractive transition, are circled in black.

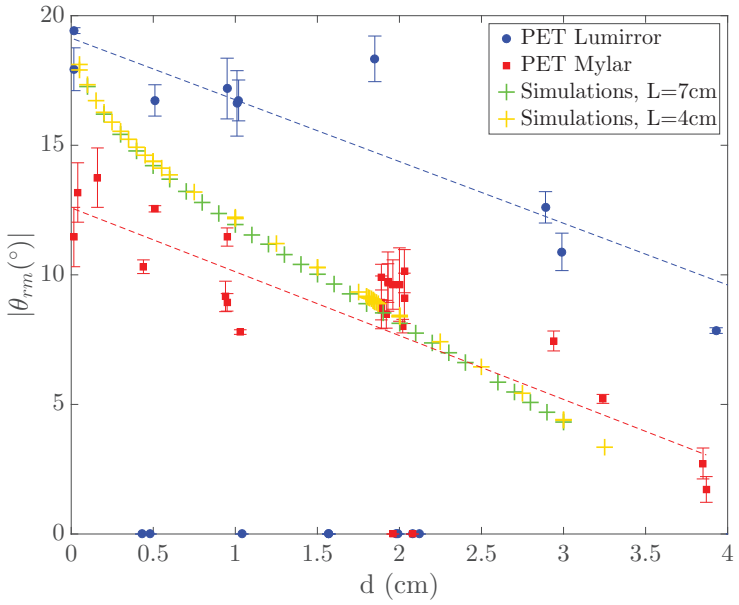

Figure 2.31 – **Maximum repulsion angle vs. d:** The simulation results were overlaid over the experimental data obtained by Dalbe *et al.* [2].

Making a first order approximation, the PLS gives α_k as:

$$\alpha_k \approx -\frac{2}{\pi^2}\left(\frac{K_{II}}{K_I}\right)_k \tag{2.5}$$

Clearly, θ_k grows more and more repulsive as long as the added α_k is negative; θ_n changes of variation direction when α_k changes sign. Because K_I is necessarily always positive, this is only possible when K_{II} takes the opposite sign, signalling a change in the direction of the sliding mode loading direction.

2.4.5 Analysis of the repulsive component

Maximum repulsion

Excluding trajectories starting with a too short L, the maximum repulsion angle θ_{rm} between two EP-cracks in Dalbe's geometry is a function dependant only on d. In Fig.2.31, we present θ_{rm} for (L, d) combinations that result in an initially decreasing θ_k function of the pseudo time (such as cases (a) and (b) in Fig. 2.30): if θ_k is already increasing at the onset of propagation, the final trajectory is too truncated to properly estimate θ_{rm}.

We find that θ_{rm}, as predicted by the principle of local symmetry, is of the same order of magnitude than the one retrieved experimentally. That θ_{rm} follows the same decreasing trends both experimentally and in simulation is also a surprise: given previous works [1, 3], it was not expected that LEFM would be sufficient to give such a good approximation of EP-cracks trajectories. It is, of course, impossible to explain the difference between the PET Lumirror® and Mylar® using a purely elastic theoretical framework. We will examine in section 3.2 if the extra

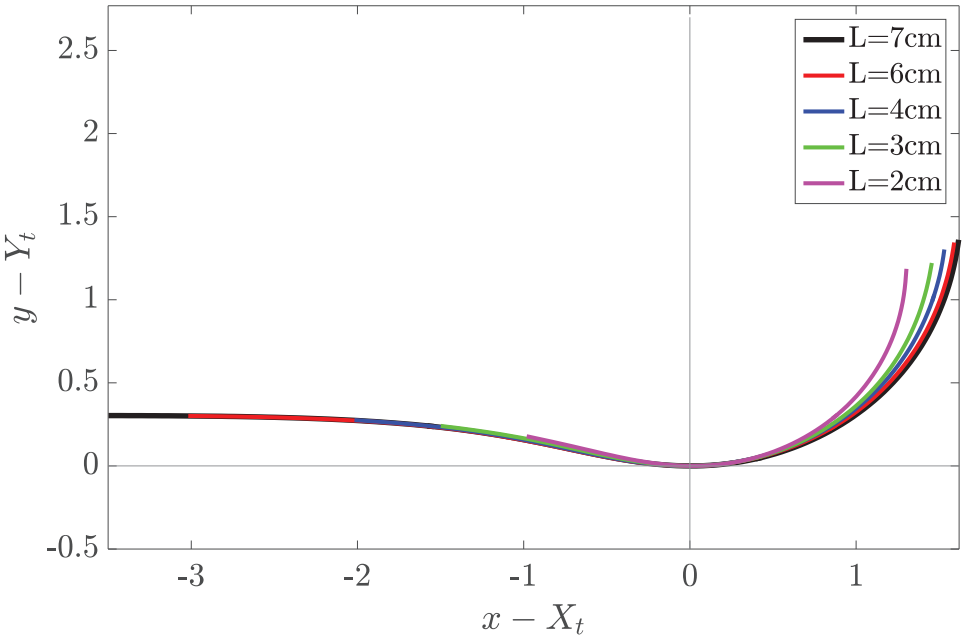

Figure 2.32 – **Shifted EP-cracks trajectories:** In this example, $d = 1$ cm. The trajectories ((x, y) coordinates for the left crack in the original referential) were shifted so that the point of maximum repulsion (X_t, Y_t) fell on $(0, 0)$.

parameter used in diffuse damage models could be a possible extra input helpful to distinguish two macroscopically equivalent materials.

Universal behaviour

In their experiments, Dalbe *et al.* [2] observed that for a fixed d separation and varying the L distance all EP-crack trajectories collapse on a single master curve when shifted so that the repulsion to attraction fall on $(0, 0)$. As shown in Fig. 2.32, we retrieve this behaviour in simulations: for all d values tested, the repulsive component of the paths is completely collapsed for all L. The independence from L is lost in the attractive phase with larger initial separations yielding more elongated paths. This is not a discrepancy between theory and observations: in the experiments, propagation was stopped when out-of-plane deformation became consequent, shortly after overlapping. We do not have experimental data to evaluate the validity of the simulations in the attractive phase.

Shape

As EP-cracks trajectories in this configuration do not depend on L, it stands to reason that paths starting with a short L are truncated in their initial repulsive component. In the following paragraph, we are examining the repulsive component of trajectories starting with $L = 7$ cm, so that they have the necessary space to completely unfold. Observing them in log-log scale reveal they possess power-law like characteristics. As shown in Fig. 2.33a, the paths can indeed be fitted

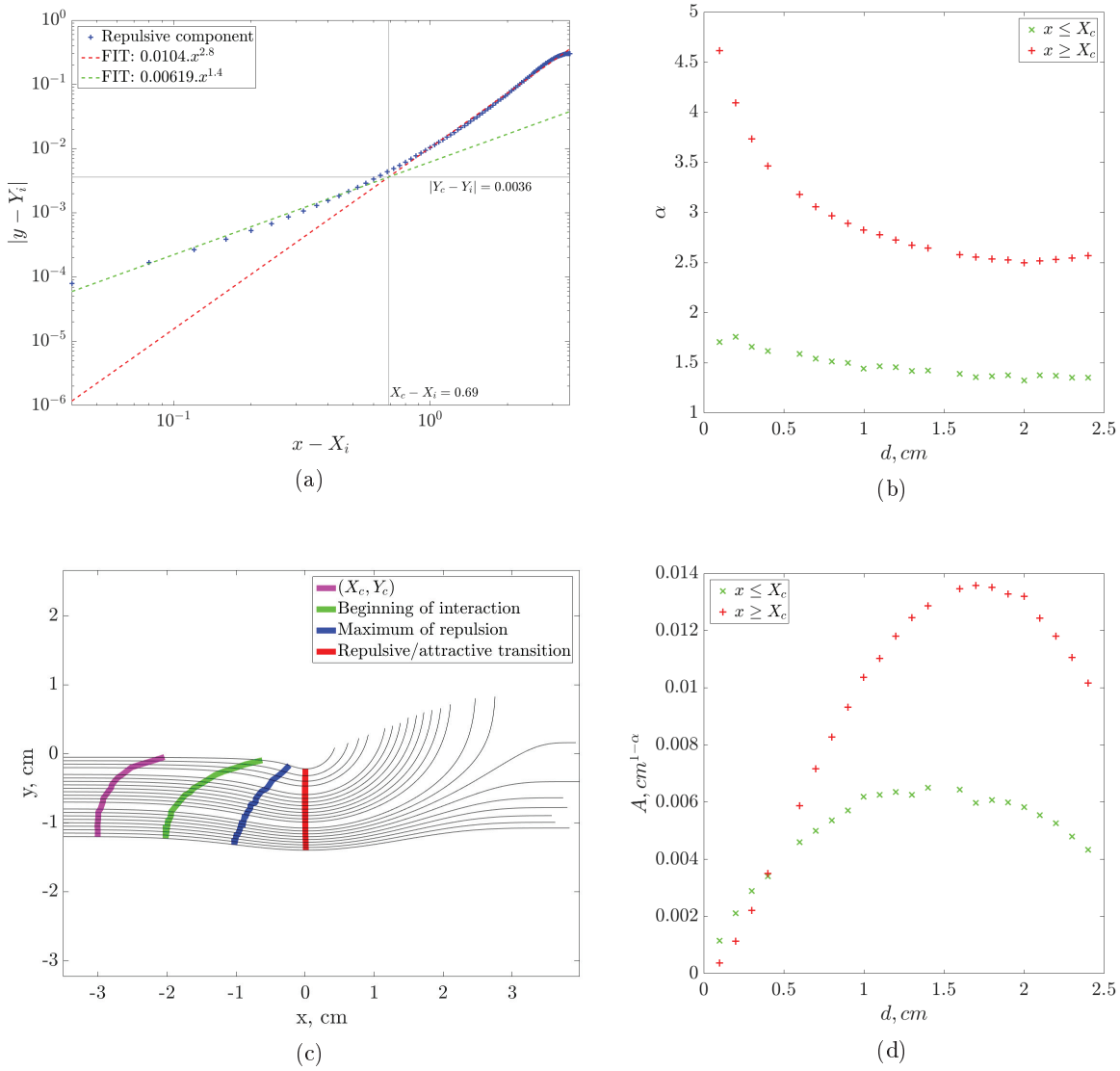

Figure 2.33 – **Piecewise regression of the repulsive component:**
(a) Fit of the regular component into two power laws. The trajectories were shifted so that all coordinates were positive, with the origin at the initial crack tip, allowing to fit linearly in log scale.
(b) Evolution of the exponents $\alpha_{1,2}$ with d.
(c) Position of the newly defined "beginning of interaction", compared to the previous definition, along with the maximum of repulsion and the turning point. Here $L = 7$ cm in all cases and d varies between 0.1 and 2.5 cm.
(d) Evolution of the factors $A_{1,2}$ with d.

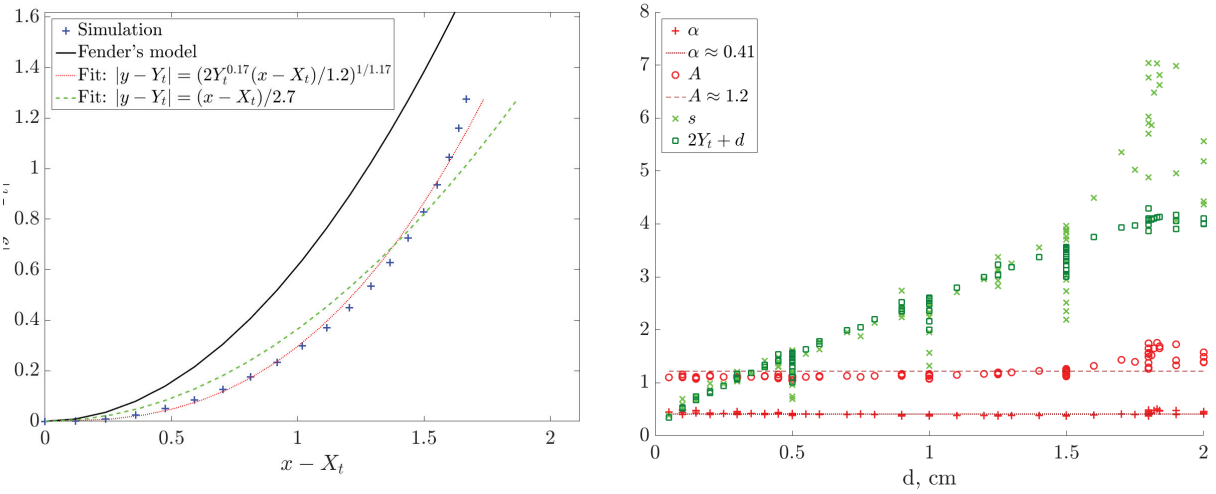

Figure 2.34 – **Attractive component fit:**
(a) Comparison between simulated paths and regressions for $L = 6$ cm and $d = 0.9$ cm. Only the attractive component was retained.
(b) Fitting parameters vs. d.

in two segments of the form:

$$|y - Y_i| = A_{1,2}.(x - X_i)^{\alpha_{1,2}} \tag{2.6}$$

where (x, y) are the coordinates along the left trajectory and $(X_i, Y_i) = (-L/2, -d/2)$ the coordinates of its starting point. The limit between the two fits is effective at (X_c, Y_c). This change in behaviour, combined with the fact that the second exponent α_2 is systematically larger than α_1 and that the first exponent is somewhat constant around $\alpha_1 \approx 1.4$ for all values of d (see Fig. 2.33b), suggests a new way to define the beginning of the interaction between the cracks. As shown in Fig. 2.33c, with this definition interaction occurs much earlier in the propagation than using the intersection method presented in section 2.4.2.

2.4.6 Analysis of the attractive component: comparison to Fender's model

We compared our simulated trajectories to Fender *et al.* model [1]. This model neglects repulsion and considers that crack interaction only begin at overlap, which corresponds in our case to the repulsion to attraction transition (X_t, Y_t). Their crack paths systematically fit as:

$$\frac{l}{s} = A\left(\frac{w}{s}\right)^{\alpha} \tag{2.7}$$

where $A \approx 1$ and $\alpha \approx 0.5$ are scalar parameters that do not depend on the material or the initial offset s between the cracks, and (l, w) are the coordinates along the crack paths.

Using our notations, their model becomes:

$$\frac{x - X_t}{2|Y_t|} = A\left(\frac{|y - Y_t|}{2|Y_t|}\right)^{\alpha} \tag{2.8}$$

In this equation, we replaced the initial offset between the cracks by $2|Y_t|$ as it is the actual lateral separation between the crack tips at the onset of attraction.

As shown in Fig. 2.34a our results do not exhibit the universal square root shape proposed by Fender *et al.* The difference between our results (in blue on Fig. 2.34a) and their prediction (in black) is not merely caused by the presence of a repulsive phase: when fitting eq. (2.8) (in green) to a square-root shape normalised by $s \neq 2|Y_t|$, we find that not only s tend to be greater that expected, of the order of $s \approx 2|Y_t| + d$, but the agreement with simulated data is poor.

Trying to fit to a general power-law shape using eq. (2.8) gives better results that are, this time, independent from d: in our geometry we find $A \approx 1.2$ and $\alpha \approx 0.41$, which is a 20% difference with Fender's results.

The discrepancy between this model and our simulations may be only a product of the different boundary conditions: Fender *et al.* affirmed that EP-cracks universally present a square-root shape but they used the same sample size across all their tests, rendering their conclusion a bit far-reaching.

2.5 Conclusion

Studying EP-crack pairs with a LEFM framework and assuming the principle of local symmetry yielded surprising results in many respects. First, both the investigation of the initial kink angle of EP-cracks loaded under far-field tension and the determination of EP-cracks trajectories in a realistic medium revealed that the LEFM+PLS framework is, against expectations [1, 3], able to predict repulsion of the correct order of magnitude between the cracks. It was also shown that the contradiction between the PLS predictions for perfectly aligned EP-cracks and experiments observed by Dalbe *et al.* [2] is only apparent, and no major argument opposes the use of the PLS to study interacting cracks.

Additionally, we found that the behaviour of the initial kink angle in regard to the initial position of the cracks is more complex than what was previously expected and exhibits strong multi-scale properties, in the sense that the length scales characterizing the transition from attraction to repulsion may be orders of magnitude smaller than the crack length. While the possibility of an initial repulsive behaviour does not fit the universal model proposed by Fender *et al.* [1], the fact that repulsion is induced only by close standing inner tips may explain why the ubiquitous hook-shaped trajectory found in nature is not systematically retrieved when experimenting with shorter cracks.

Finally, further study showed that the LEFM+PLS framework is adequate to provide qualitative predictions of the complete propagation paths of EP-cracks, as all the characteristic features (hook-shape, intersection angle,...) are retrieved. This model is however not sufficient for precise, *quantitative*, determination of certain features; namely the magnitude of the repulsion or the exact position of the repulsion to attraction transition.

Because of Dalbe *et al.* [2] observation that elastically equivalent materials can yield different

result, we believe that this failure is insurmountable by a LEFM based theoretical framework. In the next chapter, we will demonstrate how a diffuse damage model can surpass this difficulty.

Chapter 3

Future prospects: experimental and numerical study of the impact of the fracture process zone

Contents

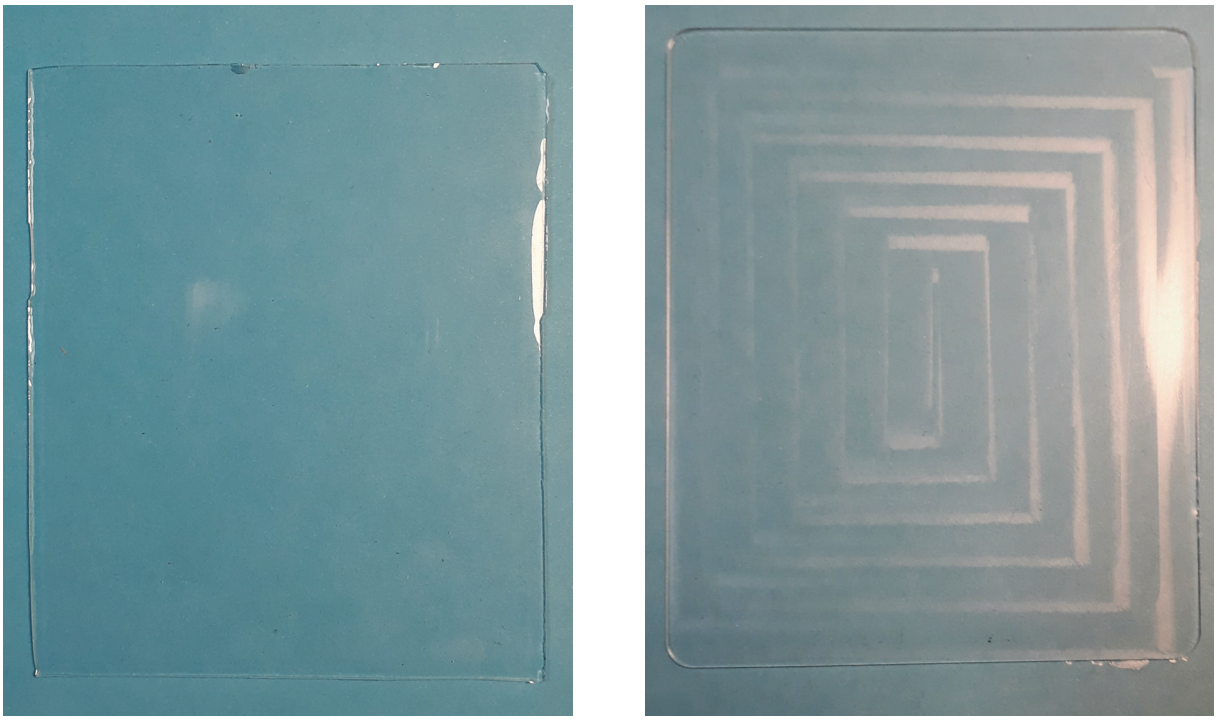

(a) (b)

Figure 3.1 – **Two kinds of samples:** (a) PDMS film made in the glass mould. (b) PDMS film made in the metal mould.

3.1 Testing the impact of the fracture process zone

As we detailed in section 1.3.1, the experiments led by Dalbe *et al.* [2] suggest that the presence of a fracture process zone can be one of the main parameters controlling the magnitude of the repulsion between EP-cracks. Considering the three materials they tested, two different polyethylene terephthalate sheets and a polycarbonate one, it seems that the magnitude of repulsion is *inversely* proportional to the size of the fracture process zone. On the contrary, Koivisto *et al.* [3] advocated that repulsion is induced by the process zone, implying that the magnitude of repulsion should be *directly* proportional to the size the process zone.

To bring some clarity to these conflicting observations, we led during the 3 months internship of Charles Peretti an experimental study of EP-cracks propagating into polydimethylsiloxane (PDMS). PDMS is an elastomer whose Young's modulus is relatively weak at $E \sim 1$ MPa, and whose Poisson's ratio is $\nu = 0.5$. PDMS behaves elastically at low strain but softens at higher strain. Because this material is known for being very brittle [110] we expect the fracture process zone around the crack tips to be negligible.

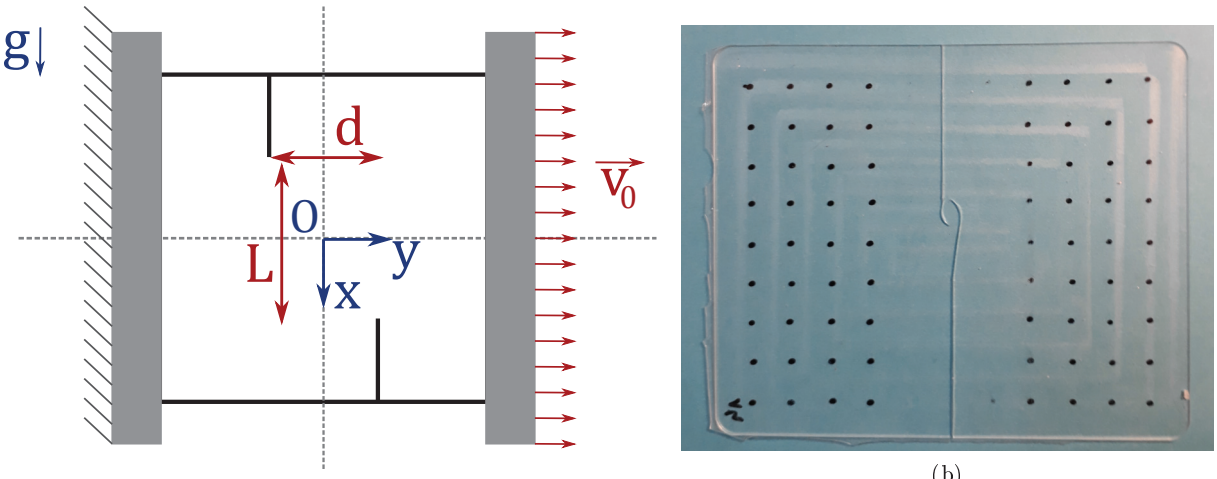

(a) (b)

Figure 3.2 – **Experimental set-up:**
(a) The right side of the sample is pulled at a constant velocity of $v_0 = 50\mu$m/s. The gravitational force $\boldsymbol{g}$, which was neglected in all simulations, may have deformed the film in the (Ox) direction, introducing an asymmetry in the cracks loading.
(b) Example of a broken sample with the grid pattern used to track the displacement.

3.1.1 Experimental set-up

Samples

The samples were crafted on site from a silicone base and a cross-linking agent that amounted to 10% in mass of the preparation. After a centrifugation step, the mix is poured into a mould and degassed under a vacuum bell to get rid of any leftover bubble. The sample is finally reticulated for at least three hours in an oven at 70°. The final product is a 10 cm $*$ 12 cm $*$ 0.1 cm film, whose surface aspect is strongly dependent on the mould used. Indeed, we had two moulds at our disposal: while one, made in glass, resulted in sleek samples (see Fig. 3.1a), the other was in metal and its machining marks imprinted on the PDMS (see Fig. 3.1b). It was also harder to remove the samples from the glass mould than the metal one, resulting in more ragged edges in the samples made in the glass mould. Because of the long degassing and reticulation times it was inconvenient to use only one type of mould; this may have introduced a dispersion in our results.

Finally, the two initial cracks were cut manually using a utility knife.

Tensile test

The samples were loaded under pure tensile stress, in the direction transverse to the cracks. As shown in Fig. 3.2a, each sample was clamped so that its free surface was a 10 cm $*$ 10 cm square using an automatic screwdriver to ensure an even tightening torque across all tests. The clamps were positioned vertically, one fixed and one pulled along the (Oy) direction at a constant velocity of 50μm.s^{-1} over a course of 5 mm.

Point tracking

Because of the high sensitivity of EP-crack trajectories to initial (boundary and loading) conditions we used point tracking to better identify the boundary conditions along the clamps. One question in particular was to determine whether the fixed points were exactly at the edges of the jaws or inside it. Should it be the later, some transverse displacement would be allowed on the sides of the sample free surface. We will show in section 3.2 the importance of this aspect in the final crack shape.

As shown in Fig. 3.2b, a 1 cm $*$ 1 cm grid pattern was therefore added on some samples which were then filmed during the test. We focused the analysis on 6 images of the 110 seconds films: the first and last images of the film corresponding to imposed displacement of 0 mm and 5 mm respectively, and 4 images during the propagation taken every 22 seconds. Given the camera pixel density and the objective-sample distance in our set-up, the final resolution is about 0.13 mm per pixel.

The displacement between two images was then determined simply by a three steps procedure:

- The coordinates of the grid pattern in each image are identified. The detection process consists in binarizing the photo, running the built-in morphologically closing filter of Matlab® 10 times, and calculating the coordinates of the barycentre of each points. Running the closing filter, which consists in a dilation step followed by an erosion step on a $3 * 3$ pixels grid, is necessary to fuse small breaks and fills gaps in the contour of the dark points.

- The correspondence between the grid patterns of two consecutive images is determined point per point, starting from the top left corner, simply by identifying the nearest neighbour of each point.

- The displacement of a tracked point is computed as the difference between its coordinates in two consecutive images.

Digitisation

To determine the coordinates along the crack paths as precisely as possible, all samples were scanned at a 600 pixels per inch (or 0.04 mm per pixel) resolution after the tensile test.

To identify the crack paths, the scanned image is then analysed through the following process (see Fig. 3.3):

- The image is binarized and the cracks are identified as the two largest groups of white pixels. Each retained pixel is identified by its (x_{raw}, y_{raw}) position.

- The rough (x_{avg}, y_{avg}) coordinates along each path is determined by averaging the y_{raw} positions for each x_{raw} occurrence. Because we are interested in measuring angles and

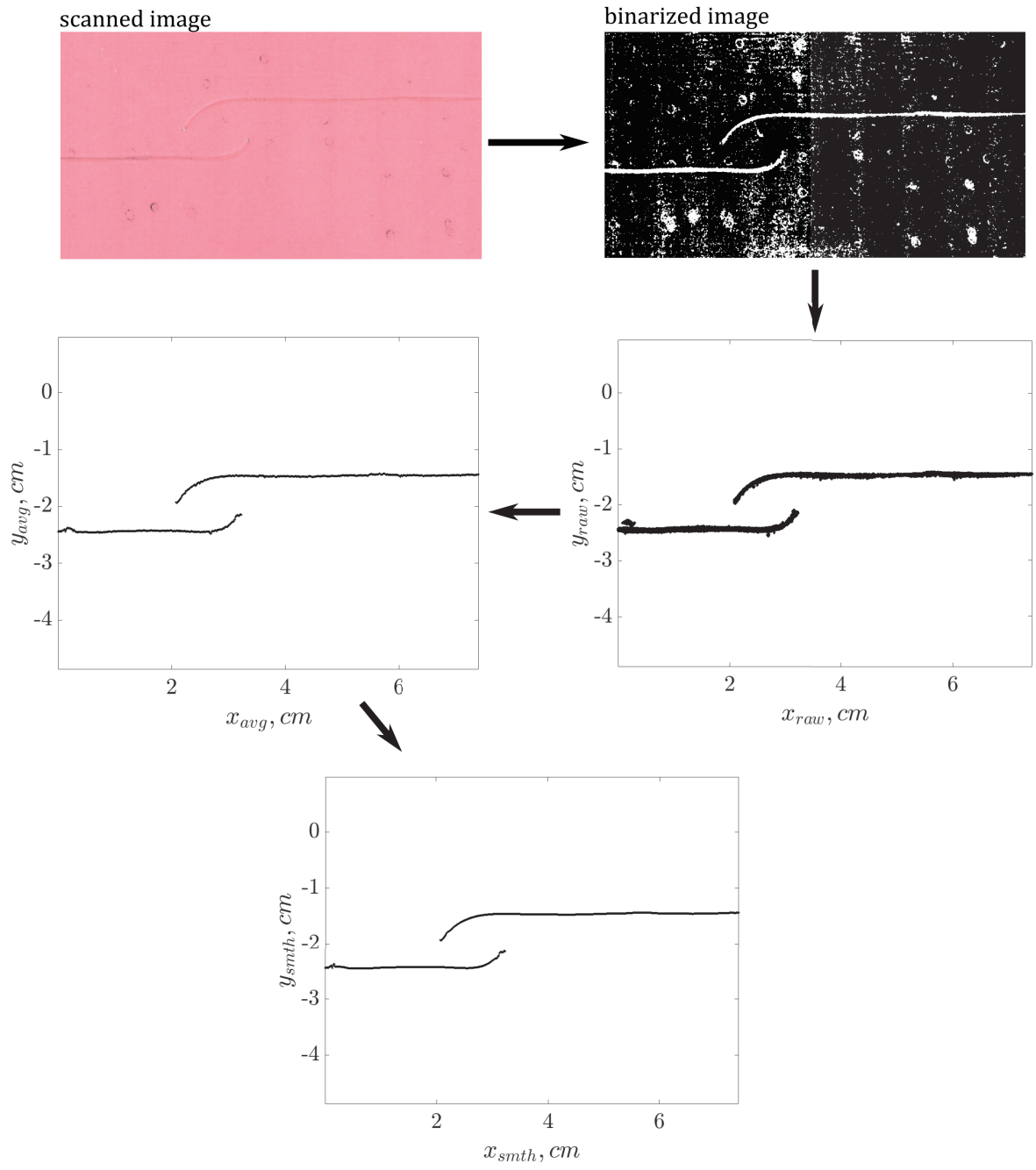

Figure 3.3 – **Digitisation process** applied to scanned images of the samples. It consists of three steps: after a binarization to retrieve the positions of the crack paths, the raw data is averaged so that the crack is represented by a simple line. Finally a running average filter is applied to smooth the trajectory and avoid artificially high valued when determining interaction angles.

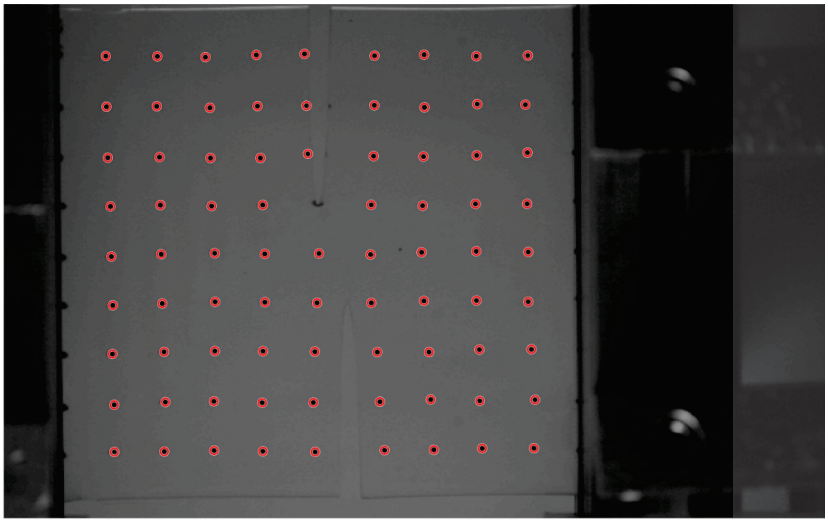

Figure 3.4 – **Point tracking example:** the red overlay indicates the points actually recognized by the point-tracking algorithm. The points too close to a clamp or a crack lip were not detected.

relative distances, we did not shift the coordinate system origin so that $(0, 0)$ fell at the center of the sample.

- To reduce noise, the rough coordinates (x_{avg}, y_{avg}) are then smoothed by a running average filter over 10 pixels in the x direction.

3.1.2 EP-cracks paths in PDMS

Boundary conditions

The clamps of the experiment we tried to reproduce numerically in section 2.3 were reported to allow *some* transverse displacement [2]. We modelled this by letting displacement totally free in the Ox direction. It turns out that his modelling choice has a great effect on the maximum angle of repulsion: it is markedly larger when u_x is free along the sample borders than when the clamp is idealised, imposing both u_x and u_y along the clamped edges. Comparing only the order of magnitude in the experimental and simulated repulsion angles led us to believe that our set-up was also better represented with imperfect clamps, by letting u_x free: a portion of the results presented in section 3.2 were obtained under this assumption.

Using point tracking during a few tensile tests allowed us to check the validity of this hypothesis. Because of poor contrast in the video, we were unable to track the grid pattern right along the clamps: the outermost points we were able to detect were separated by 1 cm from the edges (see Fig. 3.4). The displacement field at the beginning of the tensile test, measured between $t = 0$ s and $t = 22$ s is shown in Fig. 3.5a, while the total displacement measured the end of the experiment field is shown in Fig. 3.5b. To our surprise, the displacement of the outermost points of the grid pattern matches slightly better with what we would expect in the case of an ideal clamp. For example, while the transverse displacement u_y varied between $u_y = \pm 8.10^{-2}$ mm (depending on the position along Ox) in between the first to images in the experimental

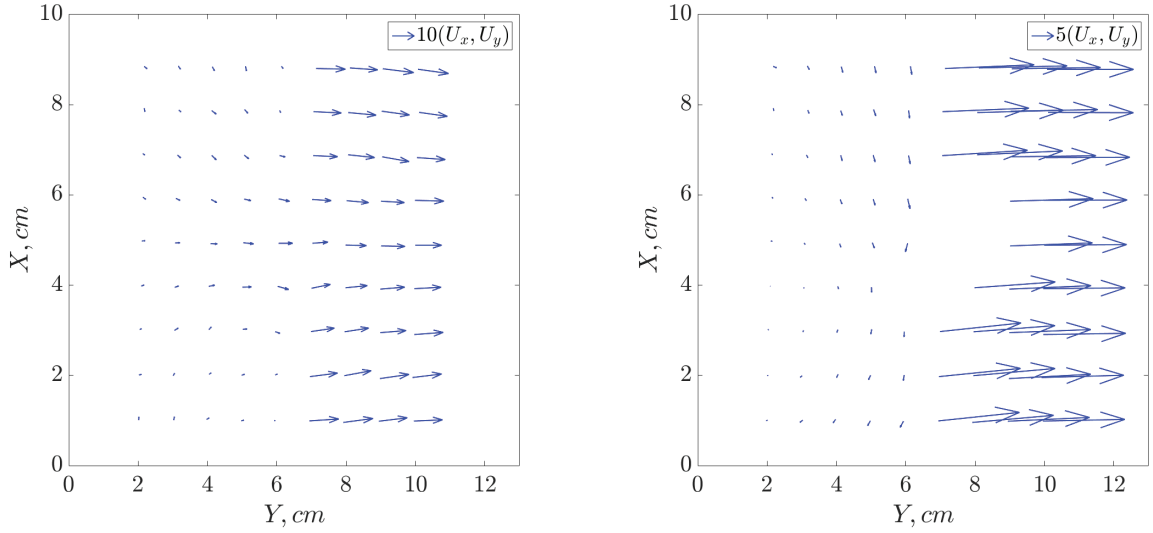

Figure 3.5 – **Tracked displacement fields:** (a) Between $t = 0$ s and $t = 22$ s (b) Between $t = 0$ s and $t = 100$ s, ie. the first and last images of the test.

case, clamped simulations give $u_y = \pm 4.10^{-2}$ mm (50% relative difference) and free transverse displacement simulations give $u_y = \pm 2.10^{-1}$ mm (150% relative difference) for a equivalent u_x imposed displacement.

Given the sensitivity of EP-crack pairs to initial conditions, it would of course be preferable to use measured displacement fields directly as simulation inputs rather than an all-or-nothing approximation. Because of time constraints we were unable to refine the simulation to this level during this Ph.D.

Reproducibility and exploitable results

Obtaining repeatable results proved to be challenging. Small imprecisions when setting up the samples, probably either slight asymmetry when cutting the cracks or a small misalignment in the clamps, leading to inhomogeneous tension, resulted in uneven propagation of the cracks: often the propagated path of one crack is much longer than the other's. Over the 30 samples analysed only 6, or 20%, exhibited both significant repulsion and reasonable symmetry between the cracks. Another 20% of the crack pairs was strongly repulsive but more asymmetrical, and 12 samples, or 40% of the total showed only weak repulsion with significant asymmetry. All remaining samples were considered unusable because one crack did not propagate at all and the other only exhibited attractive behaviour. That most of our crack paths were asymmetric is not surprising: this phenomenon was also observed by Dalbe *et al.* [2].

Absence of or minimal repulsion is not in itself the manifestation of experimental imprecisions, as it could simply be the product of the (L, d) choice. We were surprised however by how prevalent weak repulsion was, even for small d values compared to previous observations in different materials. Weak repulsion also means that the total deflection is relatively smaller when compared to

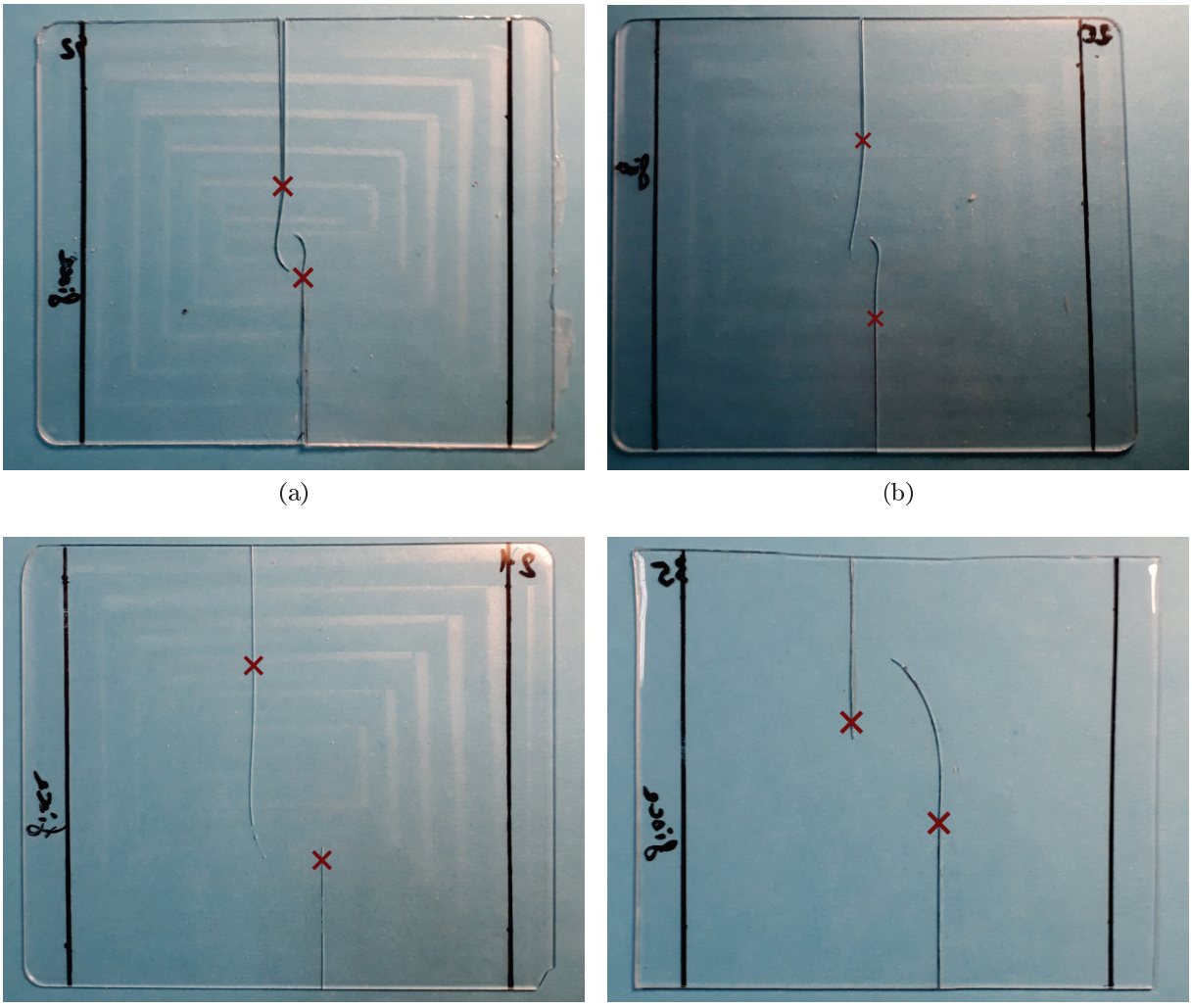

(a) (b)

(c) (d)

Figure 3.6 – **Typical examples of tensile tests results:** The overlaid red crosses indicates the initial position of the crack tips before the tensile test.
(a) Symmetrical propagation and repulsion, $L = 2$ cm and $d = 0.5$ cm.
(b) Asymmetrical propagation and repulsion, $L = 4$ cm and $d = 0.2$ cm.
(c) Asymmetrical propagation and weak repulsion, $L = 4$ cm and $d = 1.5$ cm.
(d) Asymmetrical propagation and no repulsion, $L = 2$ cm and $d = 2$ cm.

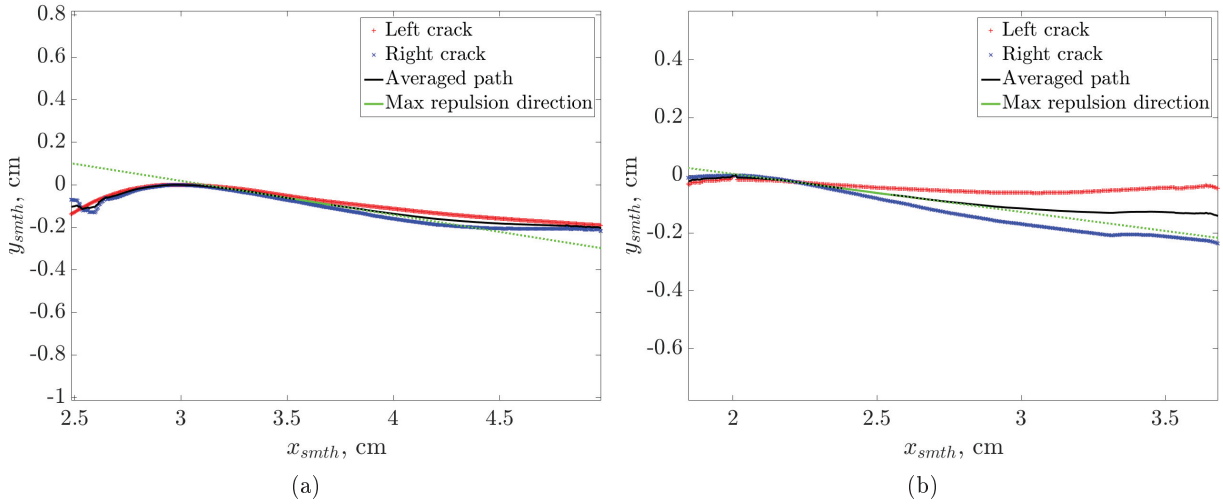

Figure 3.7 – **Measure of the maximum repulsion angle:** Example on two different samples (a) $L = 4$ cm and $d = 0.2$ cm, and (b) $L = 4$ cm and $d = 0.5$ cm. The maximum angle of repulsion θ_{rm} is formed between the horizontal and the dotted green line. The solid green line represents the path portion over which the direction θ_{rm} was linearly fitted.

noise and image resolution, making the determination of the maximum angle of repulsion harder.

Despite our concerns, the use of two different moulds did not increase the dispersion of the results: out of the six samples showing a good symmetry between the cracks a small majority (four of them) were made in a metal mould. It also did not increase the dispersion of the maximum angle of repulsion. Five (L, d) combinations were tested in both kinds of samples ; repulsion was stronger for the glass-moulded samples in three instances.

Magnitude of repulsion

To properly measure the maximum angle of repulsion we had first to account for the strong asymmetry present in most samples. In [2] the authors solved this problem by examining the separation distances $(\delta x, \delta y)$ between the crack tips at each time instead of assessing the trajectories directly. As PDMS is very brittle, crack propagation was in our case more sudden and harder to catch even when using a high-speed camera. We therefore extracted the maximum angle of repulsion between EP-cracks from the digitised paths described in section 3.1.1 rather than films taken during the tensile test.

First an "average" crack path was determined: one crack was mirrored and displaced in the (x, y) space so that the two repulsion to attraction transition points were superposed; the average crack is simply the medium line between these two paths (see Fig. 3.7). A local interaction angle θ_k is then determined for each x_{smth} position along the average path by a running linear fit. The repulsion angle θ_{rm} is then taken as the maximum of $\theta_k(x_{smth})$. The fit is applied to 2 mm long (ie. 70 pixels) portions of the path. The error was determined as the standard deviation of the local inclination angle over a 40-pixels wide portion of the crack paths, centred on θ_{rm} position.

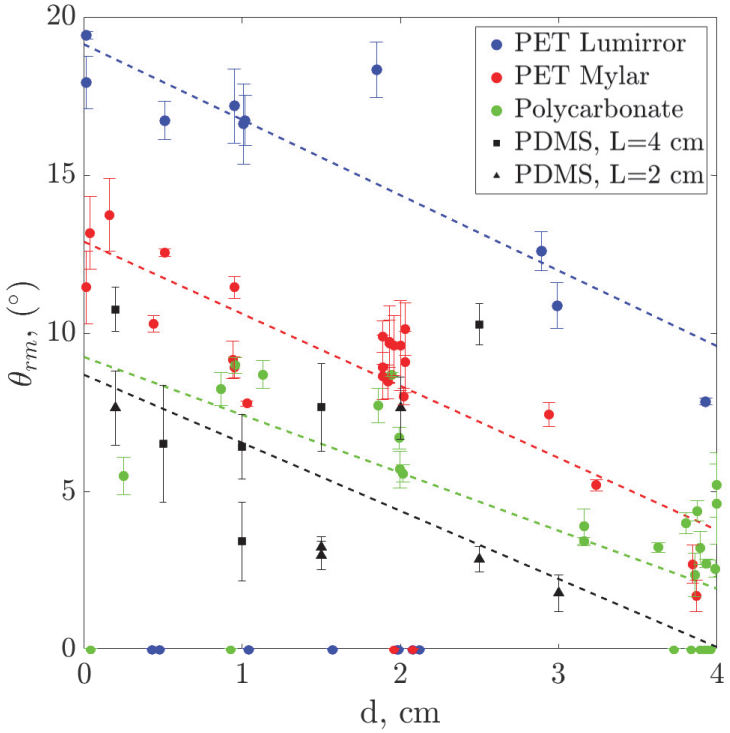

Figure 3.8 – **Repulsion angle θ_{rm} vs d for different types of plastic sheets:** our data (in black) is overlaid on the data from [2] (color). Dotted lines are linear fit of the non-zero data.

It should be noted that with this technique we necessarily loose information; in particular we are not able to determine how long before overlapping the repulsion to attraction transition happened. Also, θ_{rm} is measured on the undeformed sample, contrary what was done in [2]. This, combined with the fact that we averaged the two crack paths, may have led us to underestimate the maximum repulsion angle.

Fig. 3.8 shows our experimental results compared to the ones for PET and PC obtained by Dalbe *et al.* [2]. Some results are in agreement with expectations. Again, we find that the maximum angle of repulsion decreases somewhat linearly when d increases and is at its peak for aligned crack. It also appears that the horizontal separation distance L is of no effect on θ_{rm}. However, we were surprised to find that repulsion was systematically smaller in PDMS that in any other material: given the observations of Dalbe *et al.* [2], we initially expected strong repulsion to be correlated with brittleness.

This inconsistency may explained either by the different techniques employed to determine θ_{rm}, or as a side effect of the non-linear behaviour of PDMS. It is known to typically follow a Mooney-Rivlin model [110], in which the stress tensor derives from the strain energy density expressed as:

$$W_{el} = C_1(J^{-2/3}I_1 - 3) + C_2(J^{-4/3}I_2 - 3) \tag{3.1}$$

where C_1 and C_2 are material constants, J is the determinant of the deformation gradient, and I_1 and I_2 are the first and second invariant of the left Cauchy deformation tensor respectively. At high strain a Mooney-Rivlin material softens.

Even if the total imposed displacement was much smaller than the sample size, chosen so that the global stain was under 5%, the presence of two cracks can induce significant local strain. While it is not a fracture process zone strictly speaking, a softer material zone provoked by strain rather than damage is probably present around the crack tips. These results call again for DIC measurements of the strain field, as it would allow to determine how the size of the softened zone compare to the FPZ present in PET and PC sheets.

3.2 Diffuse damage model simulations

Our aim in this section is to investigate whether a diffuse damage model of EP-crack pairs can overcome the shortcomings of a purely LEFM representation. In particular, we are interested in finding whether it is possible to get quantitatively correct predictions of the order of magnitude of repulsion by adding an extra material parameter: the characteristic length l_c of a phase-field representing damage. To do so, we use the Abaqus phase-field implementation for fracture mechanics, proposed by Molnár *et al.* [50] and presented in section 1.2, to reproduce numerically the experiments presented in section 3.1. Most simulation results presented in this section were realised as part Guilherme Fernandes internship.

3.2.1 Computation

Mesh & material properties

We are again computing paths for EP-cracks in a small plate, under the same set of geometric parameters than in section 2.3: a 10 cm $*$10 cm square plate notched by two cracks initially separated by L and d, in plane stress (see Fig. 2.21).

The mesh was refined to a size of $h = 0.1$ mm where the crack can potentially propagate: a central rectangular zone containing the original crack tip. Outside this zone the mesh size was progressively increased until it reached about 5 mm. Again, we used linear quadratic elements everywhere.

While phase-field methods do not necessitate re-meshing at each time step, the maximum mesh able to properly render phase variations is $h_{max} = l_c/2$ [49, 50]. We chose the same mesh size h across all simulations in sections 3.2.3 and 3.2.4, so that all effects observed could be imputed to changes in l_c, L, or d and not to artefacts caused by mesh variations. As a result, the meshes were optimised for $l_c = 0.2$ mm and comported a large number of elements, around $N_{elem} \approx 180000$ depending on (L, d), and thus the size of the interaction zone, making all simulations both computing time and memory intensive.

Depending on the simulation, we used one of two materials with the following properties:

	Young's modulus E	Poisson's ratio ν	Energy release rate Gc
Material 1	$1,8.10^3$ MPa	0.35	5000 J/m^2
Material 2	1 MPa	0.35	100 J/m^2

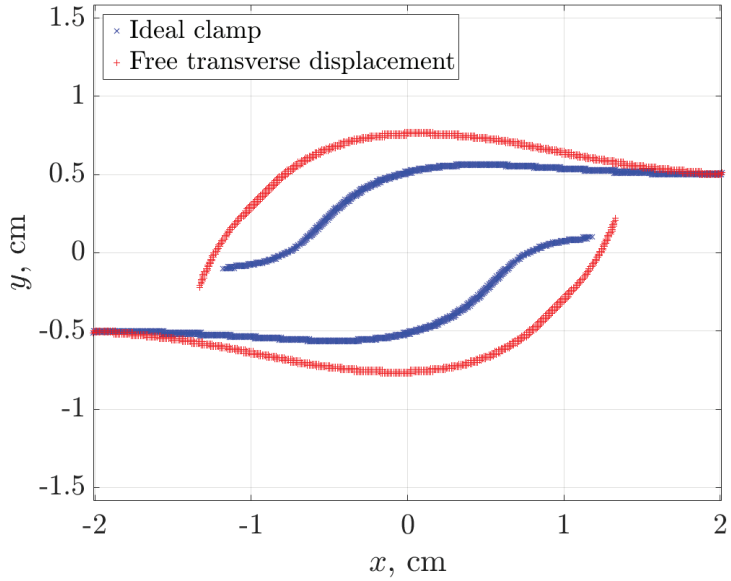

Figure 3.9 – **Impact of boundary conditions on crack path shape:** Example for $L = 4$, $d = 1$ cm, $l_c = 0.2$ mm, material 1 properties

Given the Young's moduli and the energy release rates, material 1 is more akin to PET and material 2 to PDMS. Just as in section 2.3, ν has no effect on the cracks trajectories. On the other hand, E and G_c affect the strain energy: they impact the crack propagation speed but not its shape, as long as the computation is converged in regards to the time discretization (see section 3.2.1).

Boundary conditions

The choice of boundary conditions (clamped points, restricted degrees of freedom and imposed displacement) has a significant impact on the final shape taken by EP-cracks. We initially thought the rubber-clad clamps used in the experiments we are trying to simulate were best modelled by imposed u_y and free u_x along the top and bottom sides of the sample. As we have seen in section 3.1.2, it appeared that, in the case of PDMS at least, an ideal clamp (imposed u_x and u_y on both edges) is a better fit. When we came to this realisation, a significant number of computations had already been completed: as a consequence, results presented in section 3.2.3 regarding the impact of l_c on the cracks shape were obtained making the free transverse displacement assumption. On the other hand, all results in section 3.2.4 regarding the variations of θ_{rm} with d for different l_c were computed under the ideal clamp assumption.

In Fig. 3.9 we present an example of how the final path shape is affected by the choice of boundary conditions. As expected, an ideal clamp returns weaker repulsion, both in terms of the maximum angle of repulsion and the length of the repulsive component. It also affected the hook to s-shape transition, which happened for smaller values of d when an ideal clamp was used.

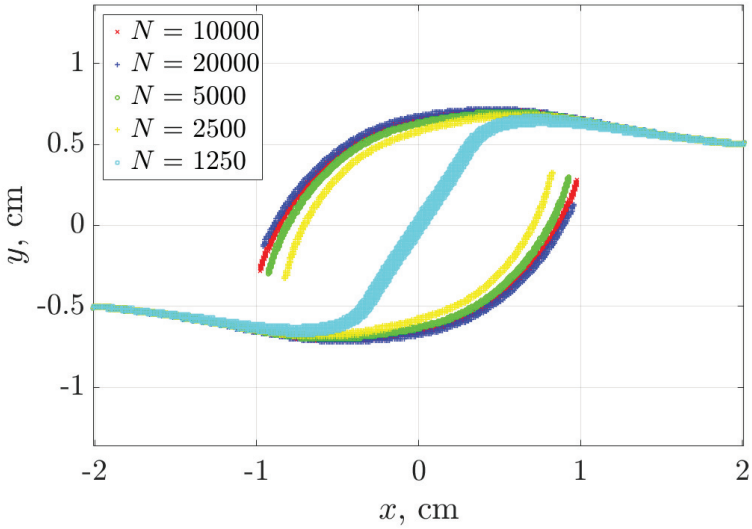

Figure 3.10 – **Loading step speed effect on crack path shape:** Example for $L = 4$ cm, $d = 1$ cm, $l_c = 1$ mm, material 1 properties and free transverse displacement conditions.

Incremental loading

The total displacement U imposed is not applied at once: doing so would induce a too strong change in the strain energy. It is reached instead in N time steps, or *frames* to ensure compliance with the quasi-static propagation assumption (see eq. 1.77). Between two consecutive frames the imposed displacement is therefore increased by $\Delta U = U/N$.

The value taken by N will directly affect the variation of strain energy between two time steps and thus the crack path shape. While large values of N slow the computation, we must choose it large enough to ensure the simulation is converged.

In Fig. 3.10 we show how the crack paths are modified by the choice of N. A much too small $N = 1250$ yields a physically unrealistic behaviour, with the two cracks joining tip to tip. Only doubling N will give better results: past this point, N has little effect on the final path shape and most significant variations are in the attractive phase. The position of the repulsion to attraction transition (happening later with greater N) is affected to a lesser extent. Our main interest, the slope of the repulsive component is barely altered when changing N.

It should be noted that the optimum choice of N is not independent from other parameters. Because the core issue is to ensure a small energy variation between two pseudo-time steps, N must be chosen in regards of l_c and G_c, whose values are also at play in the energy balance. In particular, G_c opposes crack propagation: greater G_c allows us to use less time increments, while l_c has an opposite effect.

To focus our study on the effects of l_c and (L, d) on crack paths, we conserved the same $\Delta u = 4.10^{-5}$ cm across all simulations.

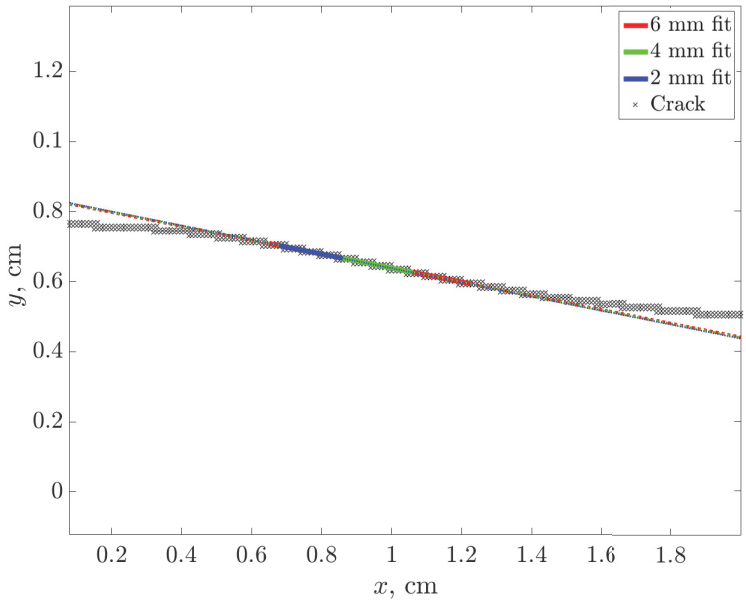

Figure 3.11 – **Maximum repulsion angle:** θ_{rm} was determined as the slope of a linear in the repulsive phase. In this example the first material properties and a free transverse displacement boundary condition were used. $l_c = 0.2$ mm, $L = 4$ cm and $d = 1$ cm.

3.2.2 Post-processing

Determining the crack paths

The result of the simulation consists of, beside the usual stress and displacement fields, the damage field defined at each node of the frame and at each time frame. Damage varies between 0 and 1: we arbitrarily defined a node as broken if its damage ϕ_d is equal to at least 0.98. In a fashion similar to what was done for post-processing the experiments in section 3.1.1, the cracks are defined as surfaces, rather than discrete lines as it was the case in section 2.3.

The maximum angle of repulsion θ_{rm} was determined in a fashion comparable to the post-processing applied to the scanned experimental samples: a linear fit along the crack paths to determine the local propagation direction. As shown in Fig. 3.11, the length of the segment over which this procedure is applied is of little consequence on the value of θ_{rm} in the vast majority of cases. In the following, we chose to retain the 2 mm wide fit value, so that the same process was applied to determine θ_{rm} in both experiments and simulations.

The position of the repulsion of attraction transition was determined simply by taking the barycentre of all nodes realising the maximum (or minimum, in the case of the bottom crack) y coordinate (see Fig. 3.14a).

Exploitable data

The Abaqus phase-field implementation [50] we are using was based on the assumption of a quasi-static propagation of the cracks. Given that our system is also symmetric in terms of

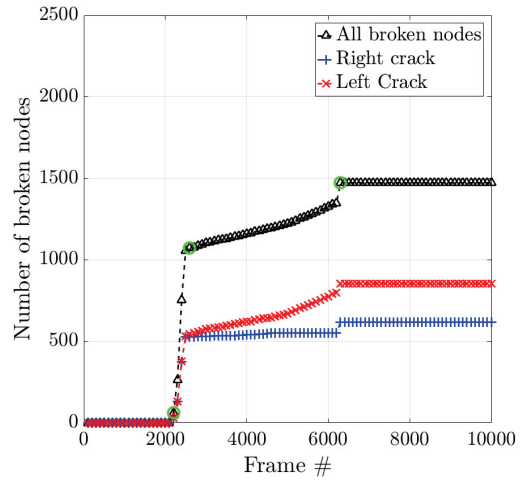

(a)

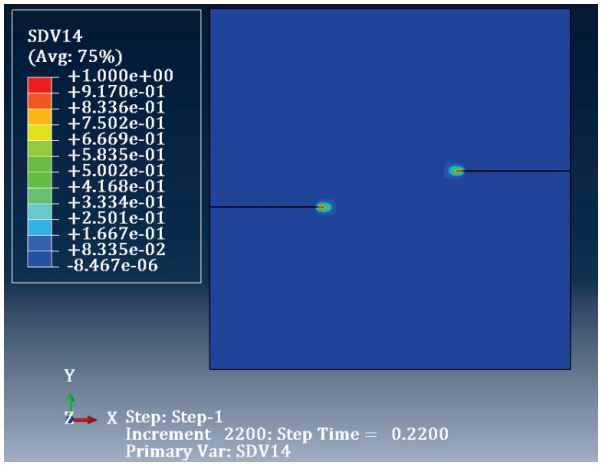

(b)

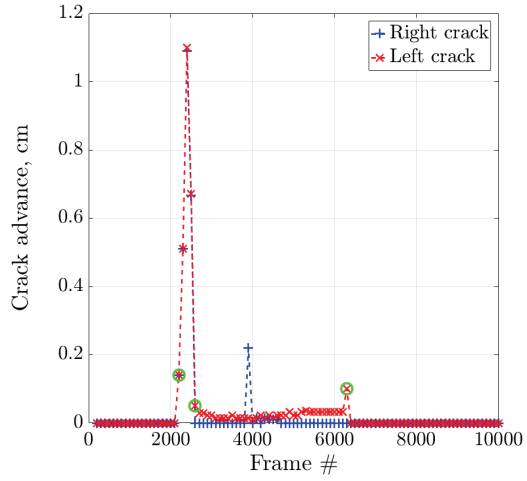

(c)

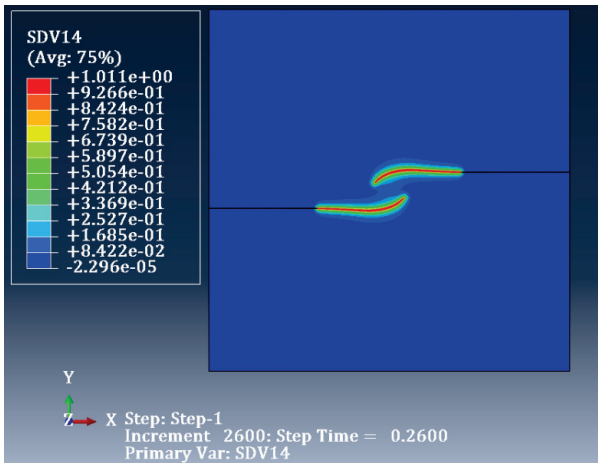

(d)

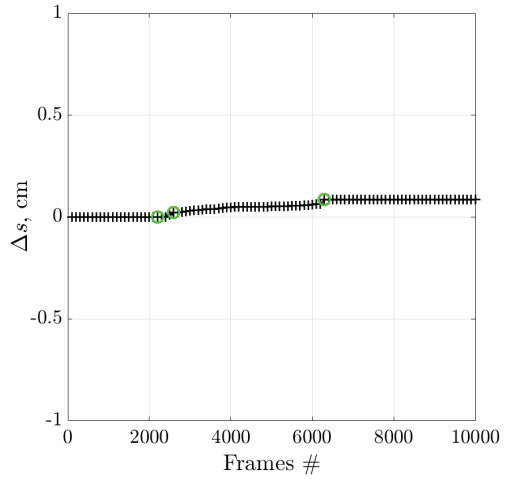

(e)

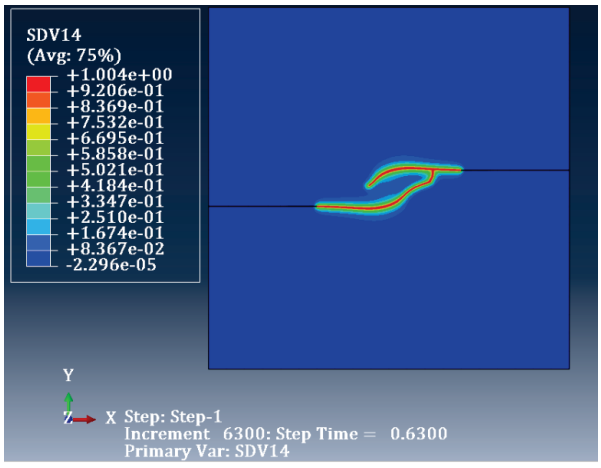

(f)

Figure 3.12 – **Last valid pseudo-time determination:** Example on $L = 4$ cm, $d = 1$ cm, $l_c = 0.5$ mm, material 1 properties and ideal clamp conditions. The total displacement was applied over a total of 10000 frames.
(b), (c) and(d): Simulation frames 2200, 2600 and 6300 respectively. They are signalled by overlaid green circle in (c), (b) and (c). (a) Evolution of the number of broken nodes with time step. (c) Separation distance between crack tip at frames f and $f - 100$. (e) Evolution of the asymmetry measure Δs with time step.

crack positions and loadings, we can expect crack paths to remain symmetric. In practice, the simulated crack paths do not remain symmetric at all time steps. After a certain computation frame, propagation becomes asymmetric either because of small irregularities in the mesh or because one crack tip jumped suddenly across several element. This kind of jump generally happens when a crack tip approaches the other crack. An example is given in Fig. 3.12f: the tortuous later stages of the bottom crack path propagated in less than a hundred time steps. This propagation is clearly not quasi-static and thus outside the scope of validity of our phase-field implementation.

As shown in Fig. 3.12c, the distance covered by a crack tip between two consecutive saved frames (we saved only one out of 100 frames to keep memory use reasonable) is not a good indicator of compliance with the quasi-staticity assumption, as it is maximum at the onset of propagation.

A better indicator is the symmetry between the cracks. It was measured in three different ways:

- For each crack, the number of "broken nodes", ie. the nodes with $\phi_d > 0.98$, was examined as a function of the pseudo-time. Symmetry is broken when the two cracks comprise different number of nodes. Out of all three methods tested it is the least reliable, because estimating whether the difference between the two crack sizes is necessarily arbitrary.
- We also studied how the crack tips advance between computational steps. The last acceptable frame is the last for which both cracks cover the same distance, past this point the cracks tend to alternate in their propagation.
- We introduced an asymmetry measure $\Delta s = \sqrt{\Sigma(x_1 - x_2')^2 + \Sigma(y_1 - y_2')^2}$, which add point per point of the crack (all nodes with $\phi_d \geqslant 0.98$) the distance between a crack (x_1, y_1) and a central symmetry reflection (x_2', y_2') of the other.

These three methods give comparable results and allowed us to determine the usable frame reliably.

In all case we tested, the repulsive component was entirely included in the last admissible frame; this limitation did not impact our study.

3.2.3 From diffuse damage to linear elasticity: impact of l_c

Free transverse displacement

We present in Fig. 3.13 EP-crack paths obtained with different l_c, when transverse displacement is let free along the top and bottom sides of the plate. In this example we are using the first material properties $L = 4$ cm and $d = 1cm$. We find that the repulsive component of the paths shortens with greater l_c values: as shown in Fig. 3.14c, ΔX_t grows linearly with l_c.

In Fig. 3.14c and 3.14d, we excluded the data point corresponding to $l_c = 1.5$ mm from the fits: out of all our computation yielding two independent cracks, this simulation is the one with largest l_c and was probably not converged regarding δU. The exact value of the coefficient in the

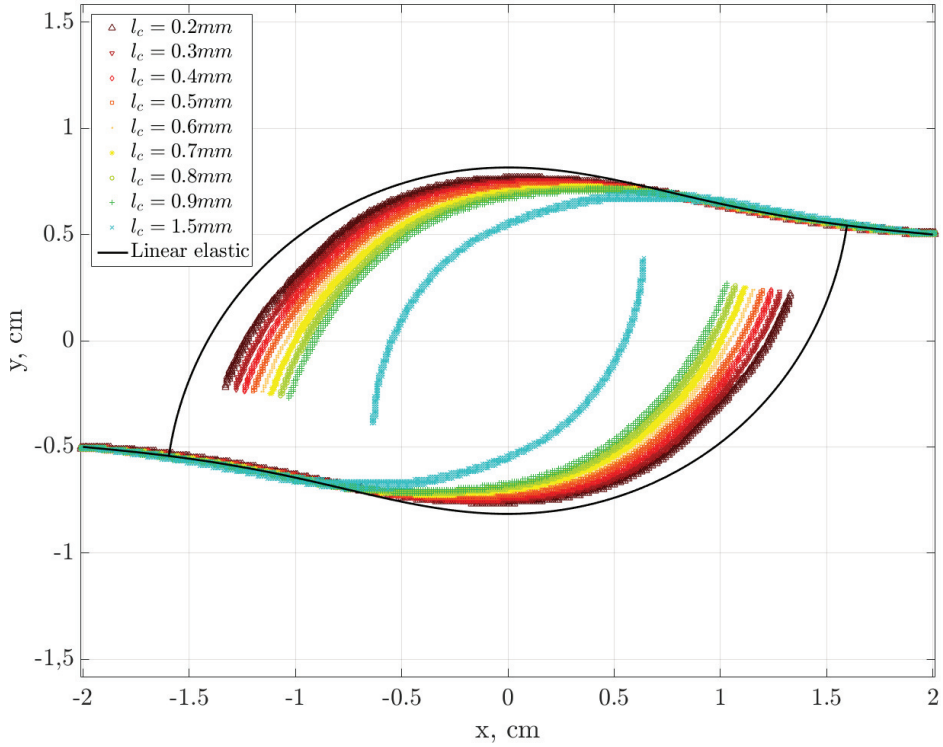

Figure 3.13 – **Impact of l_c on crack shape:** Example obtained for material 1 inputs and free transverse displacement boundary conditions, $L = 4$ cm and $d = 1$ cm. The linear elastic example was computed using $L_i = 0.4$ mm

expression linking ΔX_t to l_c depends on the ϕ_d threshold value used to extract the crack path. We find them to be relatively constant, with $\Delta X_t \approx < 1.06 \pm 0.05 > l_c - < 0.03 \pm 0.05 >$. These results confirm what is suggested by Fig. 3.13: a diffuse damage model converges linearly toward the classic LEFM solution when l_c tends to zero, in agreement with [111].

While the length of the repulsive component of the crack paths is greatly influenced by l_c, we find that the impact on its intensity, that is to say the θ_{rm}, is limited. No matter the size of the path portion over which the maximum angle of repulsion is fitted, we find that l_c does not change the value taken by θ_{rm} by more than 1.3°, an incertitude comparable to the one introduced by the linear regression of the repulsive portion of the trajectory.

Ideal clamp

The same study redone with ideal clamp style boundary conditions yields similar results. As shown in Fig. 3.15, we find again a shorter repulsive component with greater l_c, and crack paths shape getting progressively closer to a LEFM limit when l_c decreases. In this case, the cracks are s-shaped rather than hook-shaped. It appears that greater l_c values also reduce the length of the attractive phase and that the cracks return to horizontal propagation earlier.

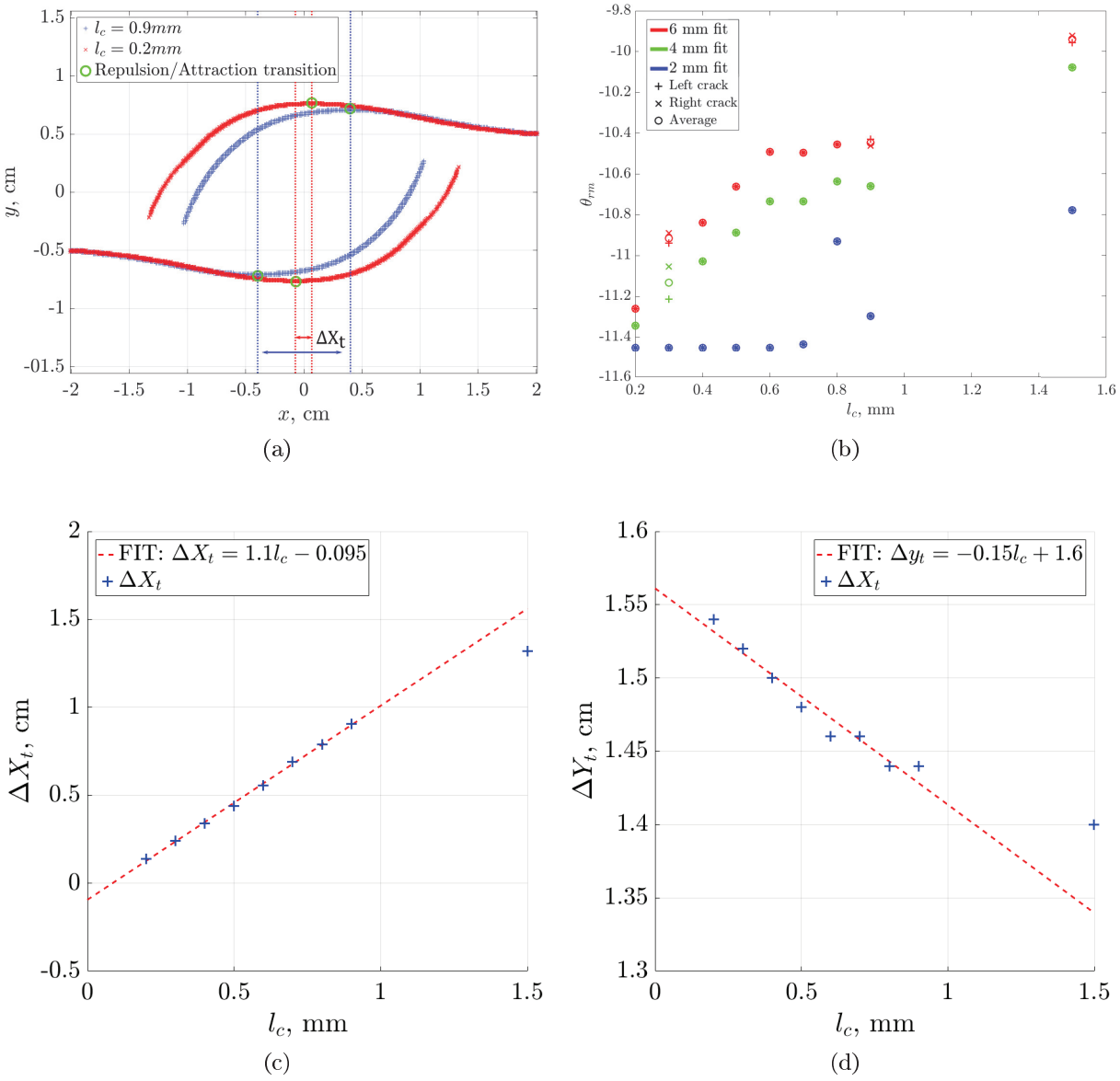

Figure 3.14 – **Convergence toward LEFM:**
(a) Definition of $(\Delta X_t, \Delta Y_t)$, the separation distances between the repulsion to attraction transitions.
(b) Evolution of the maximum angle of repulsion θ_{rm} with l_c.
(c) Evolution of the horizontal separation ΔX_t between the repulsion to attraction transitions with l_c.
(d) Evolution of the horizontal separation ΔY_t between the repulsion to attraction transitions with l_c.

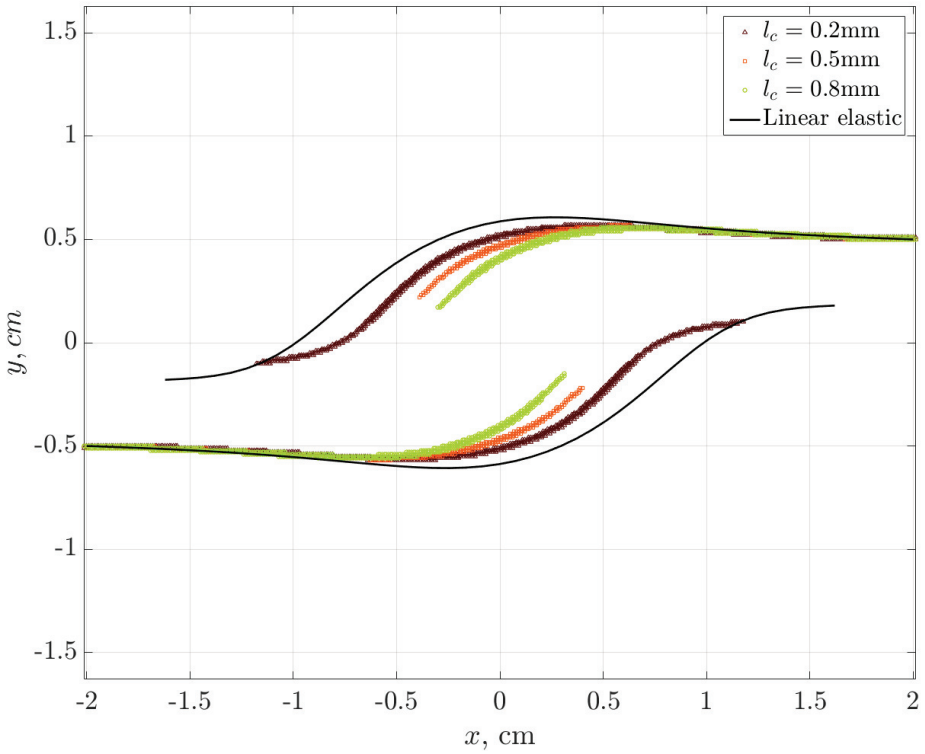

Figure 3.15 – **Impact of l_c on crack shape:** Example obtained for material 1 inputs, ideal clamp boundary conditions, $L = 4$ cm and $d = 1$ cm. The displacement u_x was blocked at all nodes of the top edge of the sample. The linear elastic case was computed using $L_i = 0.8$ mm

3.2.4 Comparison to experimental data: material nature of l_c

In this section we used the second material properties and ideal clamp boundary conditions for all simulations.

We show in Fig. 3.16a an example of how simulated trajectories fare when compared to experimental data. This case, in which $L = 4$ cm, $d = 0.5$ cm, is representative of all configuration we tested: the repulsion is severely underestimated by the simulations even for the smallest l_c value. This may be imputed, at least partially, to the choice of boundary conditions: while we have seen that the ideal clamp approximation is in our case a better modelling choice than letting u_x free on the sample edges, it is not completely accurate. Making more accurate prediction of the crack path shape requires the exact knowledge (via direct measure) of how loading is applied.

This underestimation is also visible in Fig. 3.16b, where we represented θ_{rm} as a function of the lateral separation d. The data points corresponding to $d = 0.2$ cm were not included into the linear regressions because the corresponding simulations were not converged in Δu: the cracks merged tip to tip. More than the order of magnitude of repulsion between EP-cracks, it seems that l_c impacted the slope of $\theta_{rm}(d)$. This observation remains tentative, and should be confirmed with more data points in the (l_c, d) space. It should be noted that $\theta_{rm}(d)$ cannot be linear over the whole $d = [0; 4$ cm$]$ range: while linear regression gives repulsion even at $d = 4$ cm, we found that in this situation the EP-cracks exhibited a purely attractive behaviour for both l_c tested.

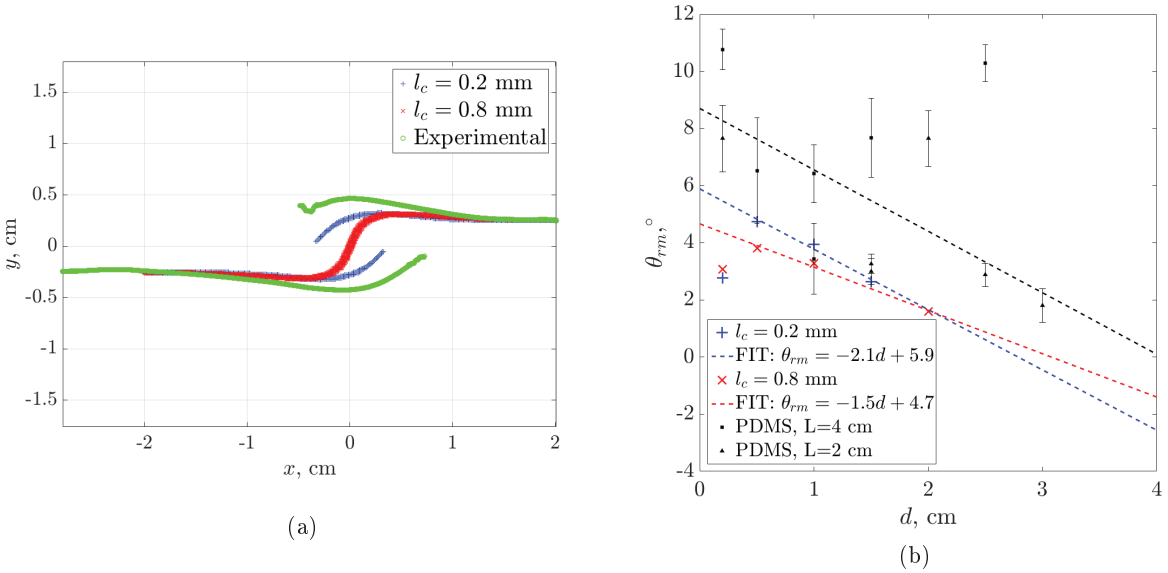

(a) (b)

Figure 3.16 – **Comparison between experimental and simulated trajectories:** The simulation data points were obtained using material 2 properties, and ideal clamp boundary conditions (a) Example for $L = 4$ cm and $d = 0.5$ cm. (b) Evolution of θ_{rm} with d.

3.3 Conclusion

Contrary to our expectations, the experiments in PDMS did not allow us to conclude whether the presence of a fracture process zone around the crack tips has a shielding or amplifying effect on the magnitude of repulsion between EP-cracks. It became clear however that, even if we showed in section 2.3 that EP-cracks repulsion can be observed in a purely linear elastic context, inelastic effects could strongly influence its magnitude. These experiments also showed that the inelastic effects at play are not necessarily damage processes localised around the crack tips: other material behaviours, such as inelastic elasticity, can unfold at a larger scale than a fracture process zone.

We were surprised to see that the characteristic length scale l_c used in diffuse damage models does not significantly impact the order of magnitude of the repulsion between EP-cracks. However these results must be treated with caution, as we were unable to simulate a large number of trajectories for different l_c and d values. Another limit of our model is how we represented the clamps: that ideal clamp simulations yielded s-shaped cracks when we only observed hook-shaped cracks in reality is another proof that our modelling choice is not ideal. Clearly, it is inconceivable to make accurate comparison between experiment and simulation without using the exact displacement field measured during experiments as an input of the computation. The diffuse damage approach is still promising: we showed that l_c impacts how θ_{rm} varies with d, which may explain the difference observed between PET and polycarbonate sheets by Dalbe *et al.* [2]. This model also predicts the repulsion to attraction to occur before the crack overlap, as in the experiments.

These results call for a more precise comparison between experiments and simulation: without

using DIC measured displacement field as inputs of the computation, it is not possible to conclude how much of the discrepancy we observed were due to poor modelling choices or to shortcomings of a diffuse damage approach.

Conclusion

This Ph.D.was first motivated by the experiments realised by Dalbe *et al.* [2]: that the observed repulsion is maximum when theory predicted straight paths, combined with surprising material effects on the paths led them to question the limitations of the principle of local symmetry. Using the same set of experimental data, Koivisto *et al.* [3] went further and challenged the very validity of linear elastic fracture mechanics theory, at least when applied to the study of interacting cracks. Our main concern was therefore to understand why the generally well-accepted LEFM+PLS framework apparently failed when applied to the specific case of EP-cracks.

Our findings reconcile theory and observation: not only we have shown that it is possible, contrary to expectation, to predict repulsive EP-cracks trajectories using only a LEFM+PLS framework but we also provided explanations of the discrepancy described by Dalbe *et al.* [2] or why the model proposed by Fender *et al.* [1] does not fit the typical hook trajectory. Indeed, our results concerning the initial kink angle of EP-crack pairs showcase how small variations in the relative position of the inner crack tips can change the initial behaviour from attractive to repulsive: the contradictions between theory and experiments can be imputed to measurement inaccuracies only.

This initial study done in the context of linear elastic fracture mechanics is not without limitations: while we have shown the *en-passant* fracture problem to be extremely sensible to initial and boundary conditions, we examined the initial kink angle of EP-crack pairs in only two specific configurations. Although it is enough to prove that the LEFM+PLS framework is not inherently unable to predict crack repulsion, our study of EP-crack loaded into pure opening far-field tension is far from being representative of EP-cracks encountered in nature or industrial applications.

Along the answer to the main question regarding the use of LEFM and the validity of the principle of local symmetry to study interacting cracks, our work on the initial kink angle of EP-cracks highlights the multi-scale nature of the *en-passant* problem; the length scales characterizing the transition from attraction to repulsion may be orders of magnitude smaller than the crack length.

The study of full trajectories in an exclusively elastic theoretical framework confirmed that modelling *some* crack repulsion is achievable without representing a fracture process zone in any way. However, these results highlighted again the strong sensitivity of the EP-cracks problems to minute changes in the relative position of the crack tips. As we were unable to retrieve magnitude of repulsion concording with Dalbe *et al.* experiments [2] and there was still unexplained material effects to consider, the next logical step was to change the theoretical framework and study how

a fracture process zone will impact the trajectories. In that order, we applied the diffuse damage theory to the case of EP-cracks using a phase-field solving technique. The phase-field represents both the crack and the damaged zone around it. Its width depends on the parameter l_c whose nature, either purely numerical or with physical meaning, was questioned by Molár *et al.* [50]. We found that the choice of l_c influences greatly the shape of the crack paths, in particular the magnitude and duration of the repulsive phase. It seems that the trajectories continuously tend to the LEFM+PLS paths when l_c decreases. This suggests that the characteristic length of the damage field is physical in nature and can be tied to local damaging process, and thus to the micro-structure of the material.

Determining the value of l_c for a given material remains a challenge. It is possible to imagine the *en-passant* fracture problem as a characterisation test; after measuring the magnitude and duration of the repulsive phase between two cracks, one can identify l_c by fitting simulated paths to observed ones. However, given the sensitivity of EP-cracks to boundary conditions, this is only possible if the exact displacement field of the medium is known precisely during propagation using for example digital image correlation. This kind of test is also inapplicable to too brittle materials, as the propagation must be quasi-static to remain within the assumptions of the theoretical framework.

Some issues remains to be addressed in our work. In particular, a recommended future work is to deepen our diffuse damage study by using DIC to properly account for boundary conditions in the simulations. It would be especially interesting to repeat the experiments on various materials, and check if it is possible to tune l_c to reproduce the cracks trajectories as precisely as possible. With enough tested materials, one can even hope to relate l_c to material behaviours such as inelasticity of damage mechanisms.

Bibliography

[1] M. Fender, F. Lechenault, and K. Daniels. Universal shapes formed by two interacting cracks. *Physical Review Letters*, 105(12):1–4, 2010.

[2] M.-J. Dalbe, J. Koivisto, L. Vanel, A. Miksic, O. Ramos, M. Alava, and S. Santucci. Repulsion and Attraction between a Pair of Cracks in a Plastic Sheet. *Physical Review Letters*, 114(20):205501, 2015.

[3] J. Koivisto, M.-J. Dalbe, M. J. Alava, and S. Santucci. Path (un)predictability of two interacting cracks in polycarbonate sheets using Digital Image Correlation. *Scientific Reports*, 6:32278, 2016.

[4] A. Griffith. The Phenomena of Rupture and Flow in Solids. *Philosophical Transactions of the Royal Society A: Mathematical, Physical and Engineering Sciences*, 221(582-593):163–198, 1920.

[5] C. Inglis. Stresses in a plate due to the presence of cracks and sharp cornes. *Trans. Inst. Nav. Archit.*, 55:219–241, 1913.

[6] H. Westergaard. Bearing pressures and cracks. *Journal of Applied Mechanics*, 61:A49–A53, 1939.

[7] M. Williams. On the Stress Distribution at the Base of a Stationary Crack. *ASME Journal of Applied Mechanics*, 24(1):109–114, 1957.

[8] G. Irwin. Analysis of Stresses and Strains Near the End of a Crack Traversing a Plate. *Journal of Applied Mechanics*, 24:361–364, 1957.

[9] C. Roux-Langlois, A. Gravouil, M.-C. Baietto, J. Réthoré, F. Mathieu, F. Hild, and S. Roux. DIC identification and X-FEM simulation of fatigue crack growth based on the Williams' series. *International Journal of Solids and Structures*, 53:38–47, 2015.

[10] Wikimedia Foundation, Inc. Fracture Mechanics. `https://en.wikipedia.org/wiki/Fracture_mechanics`, (last accessed July 18, 2018).

[11] J.-B. Leblond. *Mécanique de la rupture fragile et ductile*. Hermes Science publication, Editions Lavoisier, 2003.

[12] D. Maugis. *Contact, Adhesion and Rupture of Elastic Solids*. Springer-Verlarg Berlin Heidelberg New York, 2000.

[13] H. Bui. *Mécanique de la rupture fragile*. Masson, Paris, 1978.

[14] F. Erdogan and G. Sih. On the crack extension in plane loading and transverse shear. *Journal of Basic Engineering*, 85:519–527, 1963.

[15] I. Finnie and H. Weiss. Some observations on Sih's strain energy density approach for fracture prediction. *International Journal of Fracture*, 10(1):136–138, 1974.

[16] R. Mahajan and K. Ravi-Chandar. An experimental investigation of mixed-mode fracture. *International Journal of Fracture*, 41:235–252, 1989.

[17] G. Sih. *Handbook of stress-intensity factors*. Lehigh University, Institute of Fracture and Solid Mechanics, 1973.

[18] G. Sih. Strain-energy-density factor applied to mixed mode crack problems. *International Journal of Fracture*, 10(3):305–321, 1974.

[19] E. Gdoutos. *Problems of Mixed Mode Crack Propagation*. Martinus Nijhoff Publishers, 1984.

[20] E. Gdoutos. *Fracture Mechanics Criteria and Applications*. Kluwer Academic Publishers - Springer Netherlands, Dordrecht, 1990.

[21] L. Malíková, V. Veselý, and S. Seitl. Crack propagation direction in a mixed mode geometry estimated via multi-parameter fracture criteria. *International Journal of Fatigue*, 89:99–107, 2016.

[22] S. Maiti and R. Smith. Comparison of the criteria for mixed mode brittle fracture based on the preinstability stress-strain field - Part II: Pure shear and uniaxial compressive loading. *International Journal of Fracture*, 24(1):5–22, 1984.

[23] R. Goldstein and R. Salganik. Brittle fracture of solids with arbitrary cracks. *International Journal of Fracture*, 10(4):507–523, 1974.

[24] B. Cotterell and J.R. Rice. Slightly curved or kinked cracks. *International Journal of Fracture*, 16(2):155–169, 1980.

[25] J.-B. Leblond. Crack Paths in Plane Situations - I General Form of the Expansion of the Stress Itensity Factors. *International Journal of Solids and Structures*, 25:1311–1325, 1989.

[26] M. Amestoy and J.-B. Leblond. Crack paths in plane situations—II. Detailed form of the expansion of the stress intensity factors. *International Journal of Solids and Structures*, 29:465–501, 1992.

[27] A. Ingraffea and F. Heuze. Finite element models for rock fracture mechanics. *International Journal for Numerical and Analytical Methods in Geomechanics*, 4(1):25–43, jan 1980.

[28] P. Wawrzynek and A. Ingraffea. Interactive finite element analysis of fracture processes: An integrated approach. *Theoretical and Applied Fracture Mechanics*, 8(2):137–150, 1987.

[29] W. Gerstle, L. Martha, and A. Ingraffea. Engineering Computers Finite and Boundary Element Modeling of Crack Propagation in Two and Three Dimensions. *Engineering with Computers*, 2:167–183, 1987.

[30] T. Bittencourt, P. Wawrzynek, A. Ingraffea, and J. Sousa. Quasi-automatic simulation of crack propagation for 2D lefm problems. *Engineering Fracture Mechanics*, 55(2):321–334, 1996.

[31] P. Bouchard, F. Bay, and Y. Chastel. Numerical modelling of crack propagation: Automatic remeshing and comparison of different criteria. *Computer Methods in Applied Mechanics and Engineering*, 192(35-36):3887–3908, 2003.

[32] D. Lebaillif and N. Recho. Brittle and ductile crack propagation using automatic finite element crack box technique. *Engineering Fracture Mechanics*, 74(11):1810–1824, 2007.

[33] H. Tada, P. Paris, and G. Irwin. *The Stress Analysis of Cracks Handbook, Third Edition.* ASME, 2000.

[34] J. Rice. A Path Independent Integral and the Approximate Analysis of Strain Concentration by Notches and Cracks. *Journal of Applied Mechanics*, 35(2):379, 1968.

[35] T. Hellen. On the method of virtual crack extensions. *International Journal for Numerical Methods in Engineering*, 9(1):187–207, 1975.

[36] D. Parks. A stiffness derivative finite element technique for determination of crack tip stress intensity factors. *International Journal of Fracture*, 10(4):487–502, 1974.

[37] D. Parks. The virtual crack extension method for nonlinear material behavior. *Computer Methods in Applied Mechanics and Engineering*, 12:353–364, 1977.

[38] P. Destuynder and M. Djaoua. Sur une interpretation mathematique de l'integrale de Rice en théorie de la rupture fragile. *Mathematical Methods in the Applied Sciences*, 3:70–87, 1981.

[39] X. Suo and A. Combescure. Double virtual crack extension method for crack growth stability assessment. *International Journal of Fracture*, 57(2):127–150, 1992.

[40] G. Debruyne. Proposition d'un paramètre énergétique de rupture pour les matériaux dissipatifs. *Comptes Rendus de l'Académie des Sciences, Série IIb*, 7742(328):785–791, 2000.

[41] EDF. Code Aster Documentation. `https://www.code-aster.org/`, (last accessed May 22, 2018).

[42] Commissariat à l'énergie atomique et aux énergies alternatives (CEA). Cast3m documentation 2017. `http://www-cast3m.cea.fr/`, (last accessed October 17, 2018).

[43] M. Amestoy, H.D. Bui, and K. Dang-Van. Déviation infinitésimale d'une fissure dans une direction arbitraire. *Comptes Rendus des Séances de l'Académie des Sciences, Serie B*, 285(5):99 – 102, 1979.

[44] M. Vu, S. Geniaut, P. Massin, and J.-J. Marigo. Numerical investigation on corner singularities in cracked plates using the G-theta method with an adapted h field. *Theoretical and Applied Fracture Mechanics*, 77:59–68, 2015.

[45] X. Suo and A. Combescure. On the application of G(Theta) method and its comparison with De Lorenzi's approach. *Nuclear Engineering and Design*, 135(2):207–224, 1992.

[46] M. Stern, E. Becker, and R. Dunham. A contour integral computation of mixed-mode stress intensity factors. *International Journal of Fracture*, 12(3):359–368, 1976.

[47] J. Yau, S. Wang, and H. Corten. A Mixed-Mode Crack Analysis of Isotropic Solids Using Conservation Laws of Elasticity. *Journal of Applied Mechanics*, 47(2):335, 1980.

[48] M. Gosz and B. Moran. An interaction energy integral method for computation of mixed-mode stress intensity factors along non-planar crack fronts in three dimensions. *Engineering Fracture Mechanics*, 69(3):299–319, 2002.

[49] C. Miehe, M. Hofacker, and F. Welschinger. A phase field model for rate-independent crack propagation: Robust algorithmic implementation based on operator splits. *Computer Methods in Applied Mechanics and Engineering*, 199(45-48):2765–2778, 2010.

[50] G. Molnár and A. Gravouil. 2D and 3D Abaqus implementation of a robust staggered phase-field solution for modeling brittle fracture. *Finite Elements in Analysis and Design*, 130:27–38, 2017.

[51] J. Lemaitre and J.-L. Chaboche. *Mécanique des Matériaux Solides*. Dunod, Paris, 2ème edition, 1996.

[52] G. Borino and R. de Borst. Some observations on the regularizing field for gradient damage models. *Acta Mechanica*, 140(3):149–162, 2000.

[53] J. Mazars. Application de la mécanique de l'endommagement au comportement non linéaire et à la rupture du béton de structure. *Thèse de doctorat d'état de l'Université Paris VI*, 1984.

[54] R. de Borst, J. Pamin, and M. Geers. On coupled gradient-dependent plasticity and damage theories with a view to localization analysis. *European Journal of Mechanics, A/Solids*, 18(6):939–962, 1999.

[55] A. Karma and W.-J. Rappel. Quantitative phase field modelling of dendritic growth in two and three dimensions. *Physical Review E*, 57(4):4323, 1998.

[56] M. Kachanov. *Advanced Applied Mechanics : Elastic Solids with Many Cracks and Related Problems*, volume 30. AcademicPress Limited, 1994.

[57] Y. Wang, J. Atkison, R. Akid, and R. Parkins. Crack Interactions, Coalescence and Mixed Mode Fracture Mechanics. *Fatigue & Fracture of Engineering Materials & Structures*, 19(4):427–439, 1996.

[58] M. Ortiz. Microcrack coalescence and macroscopic crack growth initiation in brittle solids. *International Journal of Solids and Structures*, 24(3):231–250, 1988.

[59] R. Pearson and A. Yee. Toughening mechanisms in thermoplastic-modified epoxies: 1. Modification using poly(phenylene oxide). *Polymer*, 34(17):3658–3670, 1993.

[60] J. Hutchinson. Crack tip shielding by micro-cracking in brittle solids. *Acta Metallurgica*, 35(7):1605–1619, 1987.

[61] S. Nemat-Nasser. Stability of a system of interacting cracks. *International Journal of Engineering Science*, 16(4):277–285, 1978.

[62] R. Nalla, J. Kinney, and R. Ritchie. Mechanistic fracture criteria for the failure of human cortical bone. *Nature Materials*, 2(3):164–168, 2003.

[63] J. Martin, B. Yahata, J. Hundley, J. Mayer, T. Schaedler, and T. Pollock. 3D printing of high-strength aluminium alloys. *Nature*, 549(7672):365–369, 2017.

[64] P.-P. Cortet, G. Huillard, L. Vanel, and S. Ciliberto. Attractive and repulsive cracks in a heterogeneous material. *Journal of Statistical Mechanics: Theory and Experiment*, 10022(10):P10022, 2008.

[65] S. Singh, A. Harding, G. Kent, M. Sinha, V. Combier, S. Bazin, C. Tong, J. Pye, P. Barton, R. Hobbs, R. White, and J. Orcutt. Seismic reflection images of the Moho underlying melt sills at the East Pacific Rise. *Nature*, 442(7100):287–290, 2006.

[66] R. Kranz. Crack-crack and crack-pore interactions in stressed granite. *International Journal of Rock Mechanics and Mining Sciences and Geomechanics Abstracts*, 16(1):37–47, 1979.

[67] British Antarctic Survey (BAS). New footage shows crack in Larsen C Ice Shelf. `https://www.bas.ac.uk/media-post/new-footage-shows-rift-in-larsen-c-ice-shelf/`, (last accessed December 16, 2017).

[68] G. Wesley-Patterson and J. Head. Segmented lineaments on Europa: Implications for the formation of ridge complexes and bright bands. *Icarus*, 205(2):528–539, 2010.

[69] V. Acocella, A. Gudmundsson, and R. Funiciello. Interaction and linkage of extension fractures and normal faults: Examples from the rift zone of Iceland. *Journal of Structural Geology*, 22(9):1233–1246, 2000.

[70] S. Bechtle, S. Habelitz, A. Klocke, T. Fett, and G. Schneider. The fracture behaviour of dental enamel. *Biomaterials*, 31(2):375–384, 2010.

[71] G. Parsamian and T. Norman. Diffuse damage accumulation in the fracture process zone of human cortical bone specimens and its influence on fracture toughness. *Journal of Materials Science: Materials in Medicine*, 2:779–783, 2001.

[72] K. Koester, J. Ager, and R. Ritchie. The true toughness of human cortical bone measured with realistically short cracks. *Nature Materials*, 7(8):672–677, 2008.

[73] R. Nalla, J. Stölken, J. Kinney, and R. Ritchie. Fracture in human cortical bone: Local fracture criteria and toughening mechanisms. *Journal of Biomechanics*, 38(7):1517–1525, 2005.

[74] M. Launey, P. Chen, J. McKittrick, and R. Ritchie. Mechanistic aspects of the fracture toughness of elk antler bone. *Acta Biomaterialia*, 6(4):1505–1514, 2010.

[75] S. Lacour, J. Jones, S. Wagner, T. Li, and Z. Suo. Stretchable Interconnects for Elastic Electronic Surfaces. *Proceedings of the IEEE*, 93(8):1459–1466, 2005.

[76] S. Olliges, P. Gruber, S. Orso, V. Auzelyte, Y. Ekinci, H. Solak, and R. Spolenak. In situ observation of cracks in gold nano-interconnects on flexible substrates. *Scripta Materialia*, 58(3):175–178, 2008.

[77] B. Putz, R. Schoeppner, O. Glushko, D. Bahr, and M. Cordill. Improved electro-mechanical performance of gold films on polyimide without adhesion layers. *Scripta Materialia*, 102:23–26, 2015.

[78] D. Kang, P. Pikhitsa, Y. Choi, C. Lee, S. Shin, L. Piao, B. Park, K. Suh, T. Kim, and M. Choi. Ultrasensitive mechanical crack-based sensor inspired by the spider sensory system. *Nature*, 516(7530):222–226, 2014.

[79] A. Eremenko, S. Novikov, and A. Pogorelov. Investigation of the propagation and interaction of fast cracks in plexiglas. *Journal of Applied Mechanics and Technical Physics*, 20(4):477–480, 1979.

[80] D. Hull. The effect of mixed mode I/III on crack evolution in brittle solids. *International Journal of Fracture*, 70(1):59–79, 1994.

[81] P. Theocaris. Interaction of cracks with other cracks or boundaries. *International Journal of Fracture Mechanics*, 8(1):37–47, 1972.

[82] M. Swain and J. Hagan. Some observations of overlapping interacting cracks. *Engineering Fracture Mechanics*, 10(2):299–304, 1978.

[83] K. MacDonald and P. Fox. Overlapping spreading centers: new accretion geometry on the East Pacific Rise. *Nature*, 302(9):1689–1699, 1983.

[84] D. Pollard and A. Aydin. Propagation and linkage of oceanic ridge segments. *Journal of Geophysical Research*, 89:10017–10028, 1984.

[85] J.-C. Sempere and K. Macdonald. Overlapping spreading centers: implications from crack growths simulation by the displacement discontinuity method. *Tectonics*, 5(1):151–163, 1986.

[86] T. Tentler and V. Acocella. How does the initial configuration of oceanic ridge segments affect their interaction? Insights from analogue models. *Journal of Geophysical Research: Solid Earth*, 115(1):1–16, 2010.

[87] M. Kachanov. On the problems of crack interactions and crack coalescence. *International Journal of Fracture*, 120(3):537–543, 2003.

[88] M. Kachanov. A simple technique of stress analysis in elastic solids with many cracks. *International Journal of Solids and Structures*, 23(1):23–43, 1985.

[89] H. Horii and S. Nemat-Nasser. Elastic fields of interacting inhomogeneities. *International Journal of Solids and Structures*, 21(7):731–745, 1985.

[90] Y. Benveniste, G. Dvorak, J. Zarzour, and E. Wung. On interacting cracks and complex crack configurations in linear elastic media. *International Journal of Solids and Structures*, 25(11):1279–1293, 1989.

[91] D. Hills, P. Kelly, D. Dai, and A. Korsunsky. *Solution of Crack Problems The Distributed Dislocation Technique*. Kluwer Academic Publishers - Springer Netherlands, 1996.

[92] B. Bilby and J. Eshelby. Dislocation and the theory of fracture. In *Fracture*, volume I, pages 99–182. Ed. H.Lieb, 1968.

[93] D. Hull and D. Bacon. *Introduction to Dislocations*. Butterworth-Heinemann, fourth edition, 2011.

[94] S. TerMaath, S. Phoenix, and C.-Y. Hui. A technique for studying interacting cracks of complex geometry in 2D. *Engineering Fracture Mechanics*, 73(8):1086–1114, 2006.

[95] J. Burton and S. Phoenix. Superposition method for calculating singular stress fields at kinks, branches and tips in multiple crack arrays. *International Journal of Fracture*, 102(2):99–139, 2000.

[96] R. Ribeaucourt. Gestion du contact avec frottement le long des faces de fissures dans le cadre de la méthode X-FEM. Application à la fatigue tribologique. *Thèse de doctorat d'état de l'Université de Lyon*, 2006.

[97] S. Melin. Why do cracks avoid each other? *International Journal of Fracture*, 23(1):37–45, 1983.

[98] N. Mills and N. Walker. Development and growth of offset fingerlike cracks. *Engineering Fracture Mechanics*, 13(3):479–489, 1980.

[99] E. Gdoutos. Interaction between two equal skew-parallel cracks. *The Journal of Strain Analysis for Engineering Design*, 15(3):127–136, 1980.

[100] T. Yokobori, M. Ichikawa, and M. Uozumi. Interaction between two non-coplanar parallel staggered elastic cracks with narrow spacing, calculating stress intensity required for crack propagation. *Tohoku University, Research Institute for Strength and Fracture of Materials, Reports*, 7:25–47, 1971.

[101] H. Chan. Equivalent crack formation by propagating cracks under tension. *Engineering Fracture Mechanics*, 39(2):433–441, 1991.

[102] P. Baud and T. Reuschlé. A theoretical approach to the propagation of interacting cracks. *Geophysical Journal International*, 130:460–468, 1997.

[103] D. Rooke and D. Cartwright. *Compendium of Stress Intensity Factors*. Procurement Executive, Ministry of Defence. H. M. S. O., 1976.

[104] P. Forsyth. A unified description of micro and macroscopic fatigue crack behaviour. *International Journal of Fatigue*, 5(1):3–14, 1983.

[105] R. Ghelichi and K. Kamrin. Modeling growth paths of interacting crack pairs in elastic media. *Soft Matter*, 11:7995–8012, 2015.

[106] Y. Chen, Z. Wang, and X. Lin. Evaluation of the T-stress for interacting cracks. *Computational Materials Science*, 45(2):349–357, 2009.

[107] Commissariat à l'énergie atomique et aux énergies alternatives (CEA). Cast3m : Notice G_THETA. `http://www-cast3m.cea.fr/index.php?page=notices&notice=G_THETA`, (last accessed July 28, 2018).

[108] Y. Sumi. Computational crack path prediction. *Theoretical and Applied Fracture Mechanics*, 4(2):149–156, oct 1985.

[109] A. Mesgarnejad, B. Bourdin, and M. Khonsari. Validation simulations for the variational approach to fracture. *Computer Methods in Applied Mechanics and Engineering*, 290:420–437, 2015.

[110] G. Genesky and C. Cohen. Toughness and fracture energy of PDMS bimodal and trimodal networks with widely separated precursor molar masses. *Polymer*, 51(18):4152–4159, 2010.

[111] B. Bourdin, G. Francfort, and J.-J. Marigo. The variational approach to fracture To cite this version : The variational approach to fracture. *Journal of Elasticity*, pages 5–148.